

Search for displaced leptons in proton-proton collisions at
 $\sqrt{s} = 13 \text{ TeV}$

Dissertation

Presented in Partial Fulfillment of the Requirements for the Degree
Doctor of Philosophy in the Graduate School of The Ohio State
University

By

Bryan Cardwell, B.S., M.S.

Graduate Program in Physics

The Ohio State University

2021

Dissertation Committee:

Christopher Hill, Advisor

Stanley Durkin

Linda Carpenter

Andrew Heckler

© Copyright by

Bryan Cardwell

2021

Abstract

A search is presented for new long-lived particles that propagate a measurable distance through the CMS detector before decaying to leptons. The search is performed in $113\text{--}118\,\text{fb}^{-1}$ of proton-proton collision data produced by the CERN LHC at a center-of-mass energy of 13 TeV and collected by the CMS detector in 2016, 2017, and 2018. Events are selected with two leptons (an electron and a muon, two electrons, or two muons) that both have transverse impact parameter values between 0.01 cm and 10 cm. Using transverse impact parameter as the discriminating variable allows for sensitivity to displaced decays without requiring that the leptons form a common vertex. The search is designed to be sensitive to a wide range of new physics models that produce displaced di-lepton final states. The observation is consistent with the background-only hypothesis, and limits are set on the product of the cross-section of top squark pair production and the branching fraction to a lepton and a b or d quark through an R-parity-violating vertex. For a proper decay length hypothesis of 2 cm, top squarks with masses up 1500 GeV are excluded at the 95 % confidence level.

For Cristiana and Montague.

Vita

2015	B.S. Physics, North Central College
2015-2017	Graduate Teaching Associate, The Ohio State University
2017	M.S. Physics, The Ohio State University
2017-present	Graduate Research Associate, The Ohio State University

Publications

Research Publications

Included in the author list of 78 publications from CMS.

Fields of Study

Major Field: Physics

Table of Contents

	Page
Abstract	ii
Dedication	iii
Vita	iv
List of Tables	viii
List of Figures	xii
1. Introduction	1
1.1 The Standard Model	2
1.1.1 Quantum chromodynamics	4
1.1.2 The electroweak theory	4
1.1.3 The Higgs mechanism	5
1.1.4 Current status	7
1.2 Beyond the Standard Model	10
1.2.1 Supersymmetry	10
1.2.2 Long-lived particles	12
1.2.3 Displaced supersymmetry	15
2. The Large Hadron Collider and Compact Muon Solenoid experiment . .	19
2.1 The Large Hadron Collider	19
2.1.1 Injection chain	20
2.1.2 Main ring	21
2.2 The Compact Muon Solenoid experiment	27
2.2.1 Solenoid magnet	29
2.2.2 Tracker	29

2.2.3	Electromagnetic calorimeter	35
2.2.4	Hadronic calorimeter	37
2.2.5	Muon system	39
2.2.6	Trigger	41
2.2.7	Physics object reconstruction	43
3.	Search for displaced leptons	48
3.1	Overview	49
3.1.1	Long-lived particles at the LHC	49
3.1.2	Displaced leptons signature	51
3.1.3	Analysis strategy	54
3.2	Data and simulated samples	57
3.2.1	Experimental data	57
3.2.2	Simulated background events	57
3.2.3	Simulated signal events	58
3.3	Event selection	61
3.3.1	Triggers	61
3.3.2	Preselection	63
3.3.3	Prompt control region	73
3.3.4	Inclusive signal region	76
3.4	Corrections to simulation	79
3.4.1	Pileup	79
3.4.2	Lepton ID	79
3.4.3	Lepton d_0 resolution	79
3.4.4	Trigger efficiency	84
3.5	Background estimation	88
3.5.1	Background sources	88
3.5.2	Data-driven ABCD method	90
3.5.3	Closure tests in control regions	93
3.5.4	ABCD correction and systematic uncertainty	95
3.5.5	Testing full background estimation procedure	102
3.5.6	Additional background checks	104
3.6	Systematic uncertainties	110
3.6.1	Integrated luminosity	110
3.6.2	Pileup	110
3.6.3	Displaced tracking efficiency	112
3.6.4	Trigger efficiency	112
3.6.5	Lepton ID and isolation	112
3.6.6	Muon pixel hit efficiency	113
3.6.7	Lepton d_0 resolution	114
3.7	Results	115

3.7.1	Observed events	115
3.7.2	Limits	120
3.7.3	Additional likelihood tests	124
4.	Conclusion	128
Appendices		131
A.	Impact of APV25 saturation on displaced tracking	131
B.	Poorly measured lepton $ d_0 $ at large $ \eta $	135
C.	Displaced tracking efficiency	137
Bibliography		145

List of Tables

Table	Page
2.1 Luminosity parameters used in Eq. (2.1).	22
3.1 The top squark production cross sections used when generating the simulated $\tilde{t}\tilde{t} \rightarrow \bar{l}b\bar{l}b$ and $\tilde{t}\tilde{t} \rightarrow \bar{l}d\bar{l}d$ events. Cross sections are calculated at NLO + NLL by the LHC SUSY Cross Section Working Group. . .	60
3.2 The $e\mu$ preselection criteria. The electron and muon p_T thresholds increase in 2017 in accordance with the increased HLT electron and muon p_T thresholds.	64
3.3 The ee preselection criteria. The electron p_T threshold increase in 2017 and 2018 in accordance with the increased HLT electron p_T threshold. .	65
3.4 The $\mu\mu$ preselection criteria. The muon p_T threshold increase in 2017 and 2018 in accordance with the increased HLT muon p_T threshold. .	66
3.5 The electron tight ID requirements, which are identical to the tight cut-based ID from the CMS EGamma Physics Object Group with the d_0 and d_z requirements removed. Electron ID quantity definitions are available in Ref. [1].	67
3.6 The muon tight ID requirements, which are identical to the tight cut-based ID from the CMS Muon Physics Object Group with the requirements on d_0 and d_z removed.	68
3.7 The cumulative efficiency for simulated $\tilde{t}\tilde{t} \rightarrow \bar{l}b\bar{l}b$ signal events to pass the 2018 inclusive signal region selection, for several choices of \tilde{t} mass and $c\tau$. The corrections described in Section 3.4 are applied.	78

3.8	The average σ_{align} for electrons and muons, for the 2017 and 2018 analyses.	82
3.9	The unprescaled p_T^{miss} triggers used to create an orthogonal data sample for the trigger efficiency calculation.	85
3.10	The trigger efficiency scale factors in each channel and year.	86
3.11	The p_T boundaries between the low- and high- p_T bins of SR I in each channel.	93
3.12	Closure test results in background simulation (with and without $Z \rightarrow \tau\tau \rightarrow ll$ events) and in data, in the 100–500 μm region. The average extrapolated ratios and their statistical uncertainties are given. The A, B, C, and D regions are defined as follows: A is 20–30 μm in prompt lepton $ d_0 $ and 20–100 μm in displaced lepton $ d_0 $, B is 20–30 μm in prompt lepton $ d_0 $ and 100–500 μm in displaced lepton $ d_0 $, C is always 20–100 μm in displaced lepton $ d_0 $, D (the test region) is always 100–500 μm in displaced lepton $ d_0 $, and we perform repeated tests while simultaneously varying the C and D prompt lepton $ d_0 $ s within the 30–100 μm range.	95
3.13	Closure test results in data and background simulation (with and without $Z \rightarrow \tau\tau \rightarrow ll$ events), in the 500 μm –10 cm region. The ratios of the actual yield to the estimated yield and their statistical uncertainties are given. The A, B, C, and D regions are defined as follows: A is 20–30 μm in prompt lepton $ d_0 $ and 20–100 μm in displaced lepton $ d_0 $, B is 20–30 μm in prompt lepton $ d_0 $ and 500 μm –10 cm in displaced lepton $ d_0 $, C is 30–100 μm in prompt lepton $ d_0 $ and 20–100 μm in displaced lepton $ d_0 $, and D (the test region) is 30–100 μm in prompt lepton $ d_0 $ and 500 μm –10 cm in displaced lepton $ d_0 $	96
3.14	The correction factors and the uncorrected and corrected background estimates in SR I. The correction factor uncertainties include both the uncertainty in the average and the additional uncertainty obtained from varying the fit extrapolation point. The total uncertainty (statistical plus systematic) is given for the corrected background estimates.	101
3.15	The systematic uncertainty and the background estimates in SRs II, III, and IV. The total uncertainty (statistical plus systematic) is given for each estimate.	102

3.16 Closure test results in background simulation in the SRs, with the correction applied. The estimated number of events, the actual number of events, and their total uncertainties (statistical plus systematic) are given. In cases where the actual number of events is zero, the uncertainty is given by the product of the average background simulation event weight and the upper bound of the 68% Poisson interval given by a single observation of zero events.	103
3.17 Some properties of the seven events found in data with the material interactions selection inverted.	104
3.18 Background estimates in data while applying the 2018 $\mu\mu$ preselection and the additional requirement of at least one b -tagged jet. The estimates with at least one b -tagged jet are about an order of magnitude below the nominal prediction.	106
3.19 A closure test of the ABCD method in 2018 QCD simulation in the $\mu\mu$ channel with the muon isolation criterion inverted. The estimates from the ABCD method, the actual yields in simulation, and the ratios of the actual to the estimated yields are shown.	107
3.20 Systematic uncertainties in the signal efficiency for all three years and the three channels. The mean is provided in cases where the uncertainty varies by signal sample. Uncertainties in the same row are treated as correlated among the years of data taking, except for the displaced tracking and muon pixel hit efficiencies, where the 2016 uncertainty is treated as uncorrelated with the 2017 and 2018 uncertainties.	111
3.21 The number of estimated background and observed events in each channel and SR. For each estimate, the total uncertainty is given. The p_T boundaries that separate the low- and high- p_T bins of SR I are listed in Table 3.11.	116
3.22 The pre- and post-fit predictions for each signal region bin.	125
C.1 Cosmic ray muon arrival time requirements used when measuring displaced tracking efficiency in data and simulation.	140

C.2 Mean measured efficiency to reconstruct both lepton tracks in simulated $\tilde{t}\bar{t} \rightarrow \bar{l}b\bar{l}b$ events in data and simulation and the resulting systematic uncertainty. The top squark mass and proper decay length are assumed to be 1800 GeV and 100 cm.	144
--	-----

List of Figures

Figure	Page
1.1 The SM particle content.	3
1.2 Summary of Standard Model production cross section measurements from the CMS experiment [2].	8
1.3 The Higgs boson mass corrected by a fermion loop (left) and a fermion mass corrected by photon loop (right).	10
1.4 Corrections to the Higgs boson mass from the top quark (left) and top squark (right) cancel in exact SUSY. The top quark and top squark contributions are enhanced by the large coupling between the large Higgs-top quark coupling.	11
1.5 Mass limits at 95 % CL for a simplified model of gluino pair production with gluino decays to pairs of top quarks and the LSP (left) and top squark pair production with squark decays to a top quark and the LSP (right) from several CMS analyses [3].	12
1.6 Masses and proper decay lengths of many Standard Model particles. Particles with proper decay lengths above approximately 10^{-4} m will be noticeably long-lived in collider detectors such as CMS [4].	13
1.7 Long-lived decays of the neutron (left) and muon (right).	14
1.8 Pair-produced top squarks that each decay to a bottom quark and a lepton through an R-parity-violating LQD vertex.	17
2.1 Layout of the LHC experiments [5].	20

2.2	A diagram of the CERN accelerator complex. The analysis presented in Chapter 3 utilizes protons accelerated by LINAC 2, BOOSTER (also known as PSB), PS, SPS, and finally the LHC before their ultimate collision inside CMS [6].	21
2.3	The peak instantaneous (top) and integrated (bottom) luminosity delivered by the LHC during proton operation between 2011 and 2018 [7].	24
2.4	Diagram of an LHC dipole magnet in cross-section [8].	25
2.5	The CMS detector [9].	28
2.6	The stored-energy-over-mass ratio, E/M, for several detector magnets (left), and a cross-sectional view of the four-layer winding of reinforced conductor in the CMS superconducting solenoid (right) [10].	30
2.7	Measured single hit efficiency per layer as a function of the instantaneous luminosity (left) and pileup interactions (right) in data taken with the original CMS pixel detector in 2016 [11].	33
2.8	Comparison of the original and Phase-1 CMS pixel detector layouts in y - z plane [12].	34
2.9	Layout of the CMS silicon tracker. TIB, TOB, TID, and TEC refer to subdetectors of the strip detector while PIXEL refers to the original pixel detector. The Phase-1 pixel detector is contained within the same volume [10].	35
2.10	The observed local p-value for the five decay modes and the overall combination as a function of the SM Higgs boson mass showing the importance of the ECAL mass resolution in the discovery of the Higgs boson by the CMS experiment. The dashed line shows the expected local p-values for a SM Higgs boson with a mass m_H [13].	36
2.11	Layout of the hadron calorimeter barrel (HB), outer (HO), endcap (HE), and forward (HF) subdetectors [10].	38
2.12	Muon momentum resolution as a function of momentum when using the CMS muon system, the CMS inner tracker, and the combination of the two subdetectors in two different η ranges [14].	40

2.13 Sketch of a CMS muon system drift cell showing drift lines and isochrones.	41
The plates at the top and bottom of the cell are at ground potential while the voltages applied to the electrodes are +3600 V for wires, +1800 V for strips, and -1200 V for cathodes [10].	
2.14 A sketch of a transverse slice of the CMS detector showing representative particle interactions used to identify and reconstruct particles with the CMS Particle Flow algorithm [15].	47
3.1 Illustration of several possible experimental signatures of long-lived particles [16].	50
3.2 Illustration of the displaced leptons signature showing the definition of d_0 in a transverse view of the CMS detector. X denotes a new long-lived particle, ℓ denotes an electron or muon, and Y denotes any other decay products of the new long-lived particle. When interpreting the results of the Displaced Leptons analysis with the Displaced SUSY model, X refers to a top squark and Y refers to a b or d quark.	52
3.3 Distribution of data (colors) and simulated Displaced SUSY events (black boxes) in the plane defined by electron $ d_0 $ and muon $ d_0 $. The size of the black boxes are proportional to the bin content, and the bins along the x and y axes include underflow. All events are required to pass the $e\mu$ preselection defined in Section 3.3.	55
3.4 Comparison of the the muon isolation pileup correction term in the standard muon isolation and the modified muon isolation in simulated $t\bar{t}$ events that pass the 2018 $e\mu$ preselection. Muon $ d_0 $ is constrained to be less than 100 μm in the plot on the left and between 500 and 1000 μm in the plot on the right.	69
3.5 The distribution of $t\bar{t}$ simulated events in the plane defined by electron $ d_0 $ and muon $ d_0 $. The standard isolation is applied in the plot on the left, and the modified isolation is applied in the plot on the right, and the events in both plots are required to pass the remaining 2018 $e\mu$ preselection criteria and the additional constraint that the parent of at least one lepton is a heavy-flavor meson.	70
3.6 The muon modified isolation distribution for simulated $t\bar{t}$ background and $\tilde{t}\tilde{t} \rightarrow \bar{l}b l\bar{b}$ signal events that pass the 2018 $e\mu$ preselection with no isolation criterion applied.	70

3.7	The electron $\eta - \phi$ distribution in a prompt-muon, displaced-electron control region in 2017 (left) and 2018 (right) data before vetoing the regions affected by pixel power-supply issues.	71
3.8	The di-muon $\cos(\alpha)$ distribution of 2018 NoBPTX data and simulated $\tilde{t}\tilde{t} \rightarrow \bar{l}b\bar{l}b$ events (left) and the di-muon Δt distribution in simulated cosmic ray muon events in 2016 conditions (center) and $\tilde{t}\tilde{t} \rightarrow \bar{l}b\bar{l}b$ (right) events in 2018 conditions. In each case, all $\mu\mu$ preselection criteria except those relating to cosmic rejection are applied.	72
3.9	The electron (left) and muon (right) $ d_0 $ distributions for 2018 simulation events that pass the $e\mu$ preselection criteria. The upper two plots show $\tilde{t}\tilde{t} \rightarrow \bar{l}b\bar{l}b$ simulation for a single \tilde{t} mass and four different proper decay lengths; each histogram is normalized to unity. The lower two plots show the background simulation normalized to the integrated luminosity. In all of the histograms, the last bin includes the overflow. All of the corrections from Section 3.4 are applied.	74
3.10	The cumulative number of events that pass each criterion in the $e\mu$ (upper), ee (middle), and $\mu\mu$ (lower) preselection, using 2018 signal simulation. Several \tilde{t} proper decay lengths are shown. The jet criteria do not exclude any events and are simply an artifact of the analysis framework.	75
3.11	The electron (top) and muon (bottom) p_T (left), η (center), and $ d_0 $ (right) distributions in the $e\mu$ prompt control region for 2016 data and simulated background events. The rightmost bin in each plot contains the overflow entries.	76
3.12	The electron p_T (left), η (center), and $ d_0 $ (right) distributions in the ee prompt control region for 2016 data and simulated background events. The rightmost bin in each plot contains the overflow entries.	77
3.13	The muon p_T (left), η (center), and $ d_0 $ (right) distributions in the $\mu\mu$ prompt control region for 2016 data and simulated background events. The rightmost bin in each plot contains the overflow entries.	77

3.14 The uncorrected lepton $ d_0 $ distributions in the $e\mu$ prompt control region, for electrons (left) and muons (right), for 2017 data and simulation (upper), and 2018 data and simulation (lower). The rightmost bin in each plot contains the overflow entries.	80
3.15 The average lepton $ d_0 $ as a function of ϕ in the $e\mu$ prompt control region, for electrons (left) and muons (right), for 2017 data and simulation.	81
3.16 The lepton d_0 distributions with Gaussian fits in the 2017 $e\mu$ prompt control region for (working from left to right) electrons in data, electrons in background simulation, muons in data, and muons in background simulation.	82
3.17 The lepton d_0 distributions with Gaussian fits in the 2018 $e\mu$ prompt control region for (working from left to right) electrons in data, electrons in background simulation, muons in data, and muons in background simulation.	82
3.18 The corrected lepton $ d_0 $ distributions in the $e\mu$ prompt control region, for electrons (left) and muons (right), for 2017 data and simulation (upper), and 2018 data and simulation (lower). The rightmost bin in each plot contains the overflow entries.	83
3.19 Trigger efficiency as a function of leading electron (left) or leading muon (right) p_T in the $e\mu$ channel in 2016 (top), 2017 (middle), and 2018 (bottom) in data and simulated background $t\bar{t}$ events.	87
3.20 The fraction of electrons (left) and muons (right) from different parents as a function of lepton $ d_0 $, for simulated $t\bar{t}$ events that pass the 2018 $e\mu$ channel preselection. In $t\bar{t}$ events, the vast majority of leptons whose parent is a W boson are produced in a prompt decay.	89
3.21 The fraction of muons from different parents as a function of muon $ d_0 $, for simulated DY events that pass the 2018 $\mu\mu$ channel preselection and the additional constraint that the leading and subleading muon both come from the same type of parent particle.	90

3.22 A diagram of the ABCD method overlaid on simulated background events passing the 2018 $e\mu$ preselection. A, B, and C are control regions, and D corresponds to the inclusive SR, which includes SRs I, II, III, and IV. Underflow events are included in the bins along the left and bottom edges. When performing the background estimate, regions B and C are further subdivided to coincide with the SR for which the estimate is being performed.	91
3.23 Background estimation closure tests in data, in 100–500 μm subregions of regions B (left) and C (right) in the $e\mu$ channel. Each plot shows the ratio of the actual to the estimated number of events as a function of the prompt lepton $ d_0 $ in 2016 (top) and 2017–18 (bottom). A linear fit is shown in black along with the 68 % and 95 % confidence intervals of the extrapolated fit value.	98
3.24 Background estimation closure tests in data, in 100–500 μm subregions of regions B (left) and C (right) in the ee channel. Each plot shows the ratio of the actual to the estimated number of events as a function of the prompt lepton $ d_0 $ in 2016 (top) and 2017–18 (bottom). A linear fit is shown in black along with the 68 % and 95 % confidence intervals of the extrapolated fit value.	99
3.25 Background estimation closure tests in data, in 100–500 μm subregions of regions B (left) and C (right) in the $\mu\mu$ channel. Each plot shows the ratio of the actual to the estimated number of events as a function of the prompt lepton $ d_0 $ in 2016 (top) and 2017–18 (bottom). A linear fit is shown in black along with the 68 % and 95 % confidence intervals of the extrapolated fit value.	100
3.26 The dimuon invariant mass distribution in the $\mu\mu$ channel with the muon isolation criterion inverted, for 2018 data and QCD multijet simulation.	107
3.27 The dimuon invariant mass distribution in 2018 data in the $\mu\mu$ channel, in the prompt control region (black), SR I (blue), SR IV (red), with the muon isolation and di-muon ΔR criteria inverted. The equivalent distribution from the prompt control region is also shown in green. . .	108
3.28 The pixel hit efficiency as a function of muon $ d_0 $, for cosmic simulation and NoBPTX data in 2016 (left), 2017 (middle), and 2018 (right) conditions.	114

3.29 The number of estimated background and observed events in each channel and SR, with a representative signal overlaid, for 2016 (top) and 2017–2018 (bottom). For each background estimate and signal yield, the total uncertainty is given.	117
3.30 The number of estimated background and observed events in each channel and SR, with a representative signal overlaid, for 2016–2018. For each background estimate and signal yield, the total uncertainty is given.	118
3.31 Two-dimensional distributions of $ d_0^a $ and $ d_0^b $, for the events in data that pass the $e\mu$ (left), ee (middle), and $\mu\mu$ (right) preselection. The bins along the x and y axes contain underflow. The inclusive signal region covers the region between 100 μm and 10 cm in each $ d_0 $ variable shown.	118
3.32 Two-dimensional distributions of $ d_0^a $ and $ d_0^b $, for data events in the inclusive SR in the $e\mu$ (left), ee (middle), and $\mu\mu$ (right) channels.	119
3.33 Muon ϕ and di-muon invariant mass distributions for data and composite background simulation in the $\mu\mu$ channel in the inclusive SR. The background simulation is normalized to the ABCD method background prediction.	120
3.34 The 95% CL upper limits on the long-lived particle mass ($m_{\tilde{t}}$) as a function of its lifetime ($c\tau$), for the $e\mu$, ee , and $\mu\mu$ channels. The $\tilde{t}\bar{t} \rightarrow \bar{l}b \bar{l}b$ (top) and $\tilde{t}\bar{t} \rightarrow \bar{l}d \bar{l}d$ (bottom) processes are shown.	122
3.35 The 95% CL upper limits on the long-lived particle mass ($m_{\tilde{t}}$) as a function of its lifetime ($c\tau$). The colors indicate the observed 95% CL upper limit on the cross section. The $\tilde{t}\bar{t} \rightarrow \bar{l}b \bar{l}b$ (left) and $\tilde{t}\bar{t} \rightarrow \bar{l}d \bar{l}d$ (right) processes are shown.	123
3.36 The distribution of pulls for each signal region bin, where pulls are calculated as the difference between the post-fit background yield and the pre-fit background yield divided by the pre-fit background uncertainty (left). The distribution of pulls for each background nuisance parameter, where pulls are calculated as the difference between the post-fit value and the pre-fit value divided by the pre-fit uncertainty (right).	126

3.37 The observed asymptotic significances for the $\tilde{t}\tilde{t} \rightarrow \bar{l}b\bar{l}b$ process as a function of \tilde{t} mass and lifetime using the combined results.	127
3.38 The observed asymptotic significances for the $\tilde{t}\tilde{t} \rightarrow \bar{l}b\bar{l}b$ process as a function of \tilde{t} mass and lifetime in the ee (left), $e\mu$ (center), $\mu\mu$ channels (right).	127
A.1 Transverse decay length distribution of reconstructed $K_S^0 \rightarrow \pi^+\pi^-$ candidates for various runs in 2016 (top left), 2017 (top right) and 2018 (bottom). The peak instantaneous luminosity of each run is indicated in the legend, and each distribution is normalized to the integrated luminosity of the run. In the 2016 plot, runs taken before (after) the APV25 saturation effect was mitigated are shown by solid (dashed) lines. In the 2017 plot, the run with lowest (highest) instantaneous luminosity examined in each data taking era is plotted with a dashed (solid) line. Towards the end of 2017 (orange and black lines) the LHC ran with approximately 20% fewer proton bunches, meaning that the instantaneous luminosity per bunch crossing was higher than one might naively expect from the instantaneous luminosities shown in the legend.	134
B.1 The standard deviation of the leading muon d_0 as a function of the leading muon η for simulated background events (left). To ensure that the variation in width is purely due to d_0 resolution effects, we use a sample of simulated Drell-Yan events from which the $Z \rightarrow \tau\tau \rightarrow ll$ events have been removed. Muon η distribution for simulated $\tilde{t}\tilde{t} \rightarrow \bar{l}b\bar{l}b$ events (right). The $\mu\mu$ preselection with a loosened $ \eta $ requirement is applied in both plots.	136
B.2 Electron η distribution for simulated background events in which the electron parent particles are required to be SM mesons (left). Electron η distribution for simulated $\tilde{t}\tilde{t} \rightarrow \bar{l}b\bar{l}b$ events (right). The $e\mu$ preselection with a loosened η requirement is applied in both plots.	136
C.1 Distribution of the arrival time of cosmic rays at their point of closest approach to the beamline as measured by the muon system in 2016 (left), 2017 (center), and 2018 (right) in data and simulation. Only cosmic ray muons with $ d_0 < 8$ cm and $ z_0 < 20$ cm are considered.	141

C.2 Measured downward tracking efficiency versus cosmic ray muon arrival time in 2016 (left), 2017 (center), and 2018 (right) in data and simulation. Only cosmic ray muons with $ d_0 < 8$ cm and $ z_0 < 20$ cm are considered.	141
C.3 Measured downward tracking efficiency in 2016 (top), 2017 (middle), and 2018 (bottom) versus $ d_0 $ (left) and $ d_z $ (right) in data and simulation. $ d_z $ ($ d_0 $) impact parameter is constrained to less than 20 cm (1.2 cm) when plotting against $ d_0 $ ($ d_z $).	143

Chapter 1: Introduction

2 Particle physicists seek to understand the fundamental constituents of nature and
3 their interactions. At the present moment, the Standard Model of particle physics
4 (along with the general theory of relativity) represents the most complete understand-
5 ing humanity has yet achieved. At the same time, the Standard Model cannot explain
6 gravity or several observed but not yet understood aspects of nature and therefore
7 must give way to a more complete theory at a higher energy scale. One approach
8 to understanding what might be hiding beneath the Standard Model is to use high-
9 energy particle collisions to probe nature at ever smaller length scales. This thesis
10 presents a search for beyond the Standard Model physics in 13 TeV proton-proton col-
11 lision data collected by the Compact Muon Solenoid experiment at the Large Hadron
12 Collider, which is the highest-energy particle collider ever constructed.

13 The search presented in this thesis targets new long-lived particles that produce
14 displaced leptons, a unique signature that could evade many existing searches for new
15 physics. In this chapter, I present theoretical context in the form of a brief overview
16 of the Standard Model and targeted discussion of beyond the Standard Model physics
17 and long-lived particles. I then present the experimental context with an overview of
18 the Large Hadron Collider and the Compact Muon Solenoid detector in Chapter 2,
19 present the search itself in Chapter 3, and conclude in Chapter 4.

20 **1.1 The Standard Model**

21 The Standard Model of particle physics (SM) describes all known particles and
22 their non-gravitational interactions. Developed and experimentally verified over the
23 past six decades, the SM posits the existence of twelve spin- $\frac{1}{2}$ particles, the fermions,
24 that make up all observed matter; twelve spin-1 particles, the gauge bosons, that
25 communicate the electromagnetic, weak, and strong forces; and one fundamental
26 scalar, the Higgs boson, which breaks electroweak symmetry, giving mass to the
27 gauge bosons and fermions.

28 The fermions and gauge bosons can be classified according to the forces with
29 which they interact. The fermions are divided into six quarks, which carry color and
30 interact via the strong force, and six leptons, which do not. Furthermore, all six
31 quarks and three of the leptons carry electric charge and interact electromagnetically.
32 The charged leptons include the electron, muon, and tau, and the neutral leptons
33 are called neutrinos. All fermions interact via the weak force. The gauge bosons in-
34 clude the photon, which communicates the electromagnetic force; the W^+ , W^- , and
35 Z bosons, which communicate the weak force; and eight gluons that communicate the
36 strong force. Of these, only the W^+ and W^- bosons are electrically charged and only
37 the gluons carry color charge. Finally, the fermions are grouped into three genera-
38 tions, each with two quarks, one charged leptons, and one neutral lepton. Figure 1.1
39 diagrams the grouping of the SM particles and lists some of their properties.

40 In the SM, the interactions between particles are governed by two theories: quan-
41 tum chromodynamics, which describes the strong force, and the electroweak theory,
42 which describes the electromagnetic and weak forces. The following sections provide
43 a brief overview of these theories.

Standard Model of Elementary Particles

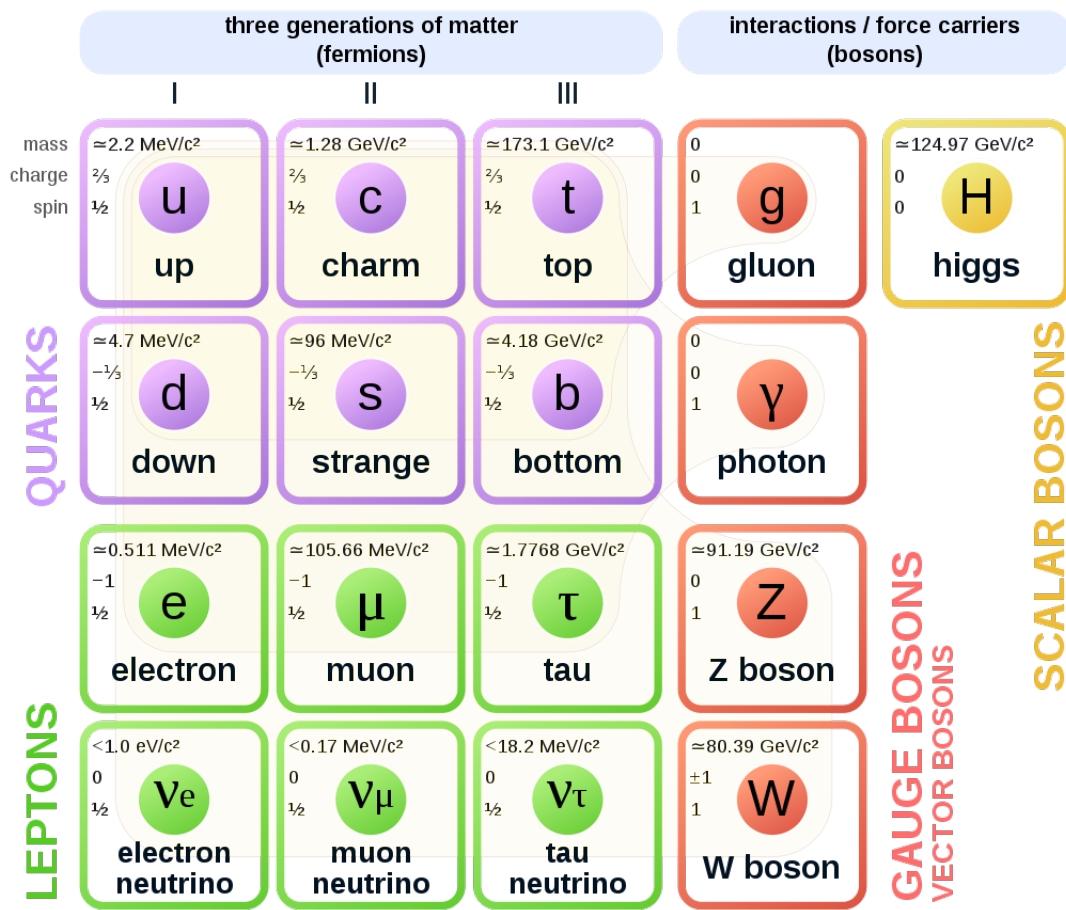


Figure 1.1: The SM particle content.

⁴⁴ **1.1.1 Quantum chromodynamics**

⁴⁵ Quantum chromodynamics (QCD) describes the strong interactions between
⁴⁶ quarks and gluons and is based on the $SU(3)_c$ symmetry group, where the subscript c
⁴⁷ refers to color charge. In QCD, all quarks and gluons carry color charge, which allows
⁴⁸ interactions between two quarks of the same generation and a gluon, three gluons,
⁴⁹ or four gluons. QCD is responsible for the formation of all hadrons (such as protons
⁵⁰ and neutrons), and leads to two unique phenomena: confinement and asymptotic
⁵¹ freedom [17, 18].

⁵² Confinement refers to the experimental fact that an isolated particle with color
⁵³ charge has never been directly observed. Composite particles composed of quarks
⁵⁴ and gluons are always neutral under color, and attempts to separate the constituent
⁵⁵ particles will only produce new hadrons. This phenomenon is the result of the unique
⁵⁶ running of the strong coupling constant, which increases with decreasing energy (and
⁵⁷ therefore increasing distance).

⁵⁸ Asymptotic freedom is the other side of the coin: if the strong coupling constant
⁵⁹ decreases as the interaction energy increases, then the strong interaction becomes
⁶⁰ more and more feeble at high energies. In high energy interactions (such as those
⁶¹ at the Large Hadron Collider), the strong coupling constant is in fact small enough
⁶² to render the quarks nearly free. In this regime, perturbative calculations become
⁶³ possible.

⁶⁴ **1.1.2 The electroweak theory**

⁶⁵ The electroweak theory unifies the electromagnetic and weak interactions and is
⁶⁶ based on the $SU(2)_L \otimes U(1)_Y$ symmetry group. It posits two new charges: weak

67 isospin, which has three components T_1 , T_2 , and T_3 , and hypercharge, Y . T_3 is $\pm\frac{1}{2}$ for
 68 all left-handed fermions and 0 otherwise, while Y varies according to $Q = T_3 + \frac{1}{2}Y$,
 69 where Q is the familiar electric charge. Each generation of left-handed quarks or
 70 leptons forms an SU(2) doublet. The first generation doublets, for example, are:

$$\begin{pmatrix} \nu_e \\ e^- \end{pmatrix}_L, \begin{pmatrix} u \\ d \end{pmatrix}_L \quad (1.1)$$

71 where, as in $SU(2)_L$, the L denotes left-handed chiral states. The three generators
 72 of $SU(2)_L$ result in three massless spin-1 bosons: W^1 , W^2 , and W^3 , while $U(1)_Y$
 73 gives rise to one massless spin-1 boson, B^0 . After electroweak symmetry is broken
 74 by the mechanism explained in the following subsection, the physical W^\pm bosons are
 75 identified as superpositions of W^1 and W^2 while the Z boson and the photon are
 76 identified as superpositions of W^3 and B^0 [19].

77 Terms in the electroweak Lagrangian involve either two left-handed fermions and a
 78 W^\pm or Z boson, two electrically charged particles and a photon, or charge-conserving
 79 combinations of W^\pm bosons, Z bosons, and photons that include three or four par-
 80 ticles. Conspicuously missing, however, are mass terms for the electroweak gauge
 81 bosons or fermions.

82 1.1.3 The Higgs mechanism

83 As shown in Fig. 1.1, the fermions and W^\pm and Z bosons all have nonzero mass.
 84 Accounting for this fact within the context of the electroweak theory is difficult be-
 85 cause explicit mass terms violate the gauge and chiral symmetry of $SU(2)_L \otimes U(1)_Y$.
 86 For example, a term such as

$$\frac{1}{2}m_A^2 A^\mu A_\mu, \quad (1.2)$$

⁸⁷ which assigns mass m_A to gauge boson A , becomes

$$\frac{1}{2}m^2(A^\mu - \partial^\mu\alpha)(A_\mu - \partial_\mu\alpha) \neq \frac{1}{2}m^2A^\mu A_\mu \quad (1.3)$$

⁸⁸ under a $U(1)_Y$ gauge transformation, and a term such as

$$m_f \bar{f} f = m_f (\bar{f}_R f_L + \bar{f}_L f_R), \quad (1.4)$$

⁸⁹ which assigns mass m_f to fermion f , breaks chiral symmetry by coupling the right-
⁹⁰ and left-handed components of the fermion.

⁹¹ If the gauge and chiral symmetries of $SU(3)_c \otimes SU(2)_L \otimes U(1)_Y$ truly are symmetries
⁹² of nature and the fermions and W^\pm and Z bosons truly have nonzero mass, then
⁹³ another mechanism must be at work. Spontaneous symmetry breaking, which occurs
⁹⁴ when the vacuum state does not exhibit all of the symmetries of the underlying
⁹⁵ theory. In such a situation, each spontaneously broken continuous symmetry gives
⁹⁶ rise to a massless scalar particle [20]. In the case of spontaneously broken continuous
⁹⁷ *gauge* symmetries, however, there exists a mechanism by which the massless bosons
⁹⁸ are removed and some of the gauge bosons associated with the generators of the
⁹⁹ symmetries acquire mass [21, 22, 23]. In the SM, this mechanism, known as the
¹⁰⁰ Higgs mechanism, breaks electroweak symmetry, gives mass to the fermions and W^\pm
¹⁰¹ and Z bosons, and results in one massive scalar particle, the Higgs boson.

¹⁰² The Higgs mechanism adds the scalar doublet

$$\Phi = \begin{pmatrix} \phi^+ \\ \phi^0 \end{pmatrix}, \quad (1.5)$$

¹⁰³ whose potential is given by

$$V(\Phi^\dagger\Phi) = \mu^2\Phi^\dagger\Phi + \lambda(\Phi^\dagger\Phi)^2, \quad (1.6)$$

104 to the SM. If $\mu^2 < 0$ and $\lambda > 0$, then $\Phi^\dagger \Phi = -\frac{\mu^2}{2\lambda}$ defines a circle of minima in the
105 $\phi^+ - \phi^0$ plane. Even though the potential remains invariant under $SU(2)_L \otimes U(1)_Y$,
106 nature must spontaneously choose a vacuum state somewhere along this circle. Be-
107 cause the vacuum state does not respect $SU(2)_L \otimes U(1)_Y$, the symmetry is said to be
108 spontaneously broken.

109 This procedure has three significant consequences. First, three of the four degrees
110 of freedom originally associated with Φ are now associated with the longitudinal
111 components of the W^\pm and Z bosons, which causes them to acquire mass while the
112 photon remains massless. Second, Φ 's remaining degree of freedom adds a single
113 massive scalar, the Higgs boson, to the theory. Third, the interaction between the
114 fermions and the nonzero vacuum state of the scalar field produces fermion mass
115 terms that obey chiral symmetry.

116 1.1.4 Current status

117 The SM is remarkably successful. It describes all known particles and their non-
118 gravitational interactions, and it has passed countless experimental tests over the last
119 several decades. Figure 1.2 gives an idea of the scale of this success by comparing
120 theoretical predictions of SM production cross sections with measurements performed
121 by the CMS experiment: theory and experiment agree across 41 different SM processes
122 at 7, 8, and 13 TeV. In 2012, the CMS and ATLAS experiments independently
123 discovered an approximately 125 GeV scalar particle with properties consistent with
124 the SM Higgs boson [13, 24]. Further measurements in 7, 8, and 13 TeV proton-proton
125 collisions at the Large Hadron Collider continue to agree with SM predictions of the
126 Higgs boson properties [25, 26]. We finally have meaningful evidence as to the origin

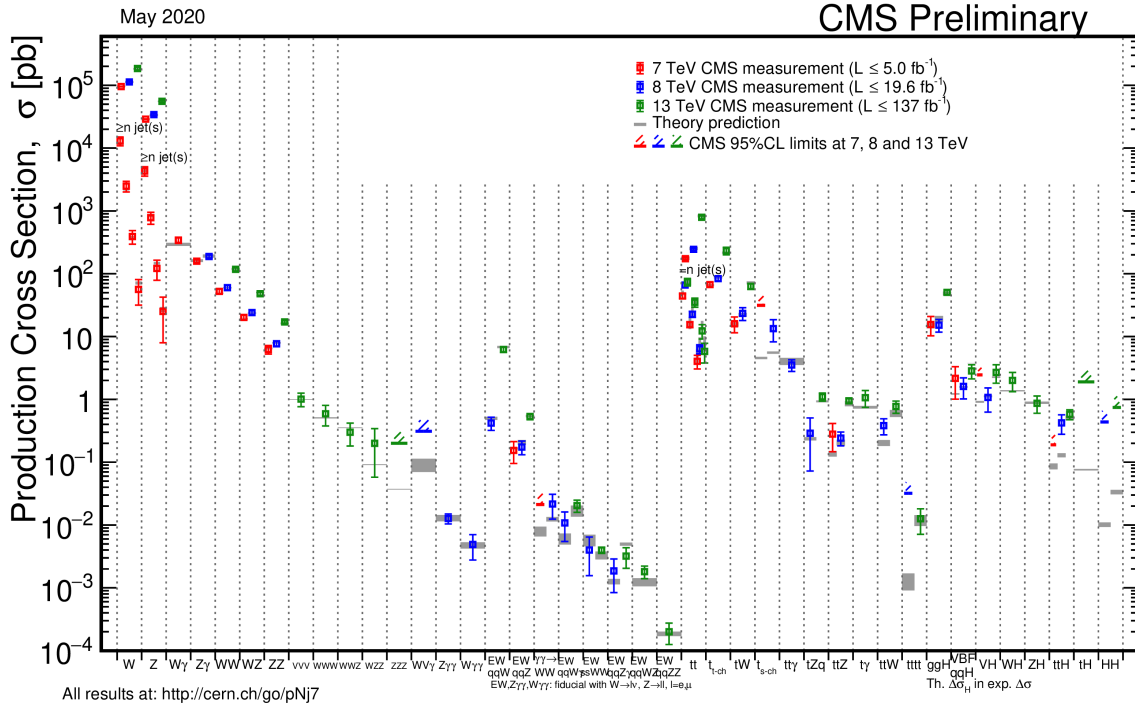


Figure 1.2: Summary of Standard Model production cross section measurements from the CMS experiment [2].

¹²⁷ of electroweak symmetry breaking, and all current evidence indicates that the SM
¹²⁸ Higgs mechanism is indeed responsible.

Despite this remarkable success, the SM is not without problems. For one, it cannot be the whole story: it says nothing on the subjects of gravity, dark matter, or dark energy, which implies that it only describes about 5% of the energy content of the universe [27] and that a more complete theory must take over at or below the energy scale where gravity becomes important ($M_P \approx 10^{19}$ GeV) [28]. Furthermore, many aspects of the SM seem arbitrary and unmotivated. It offers no explanation, for example, for why three generations of fermions are necessary or why its many parameters take the values they do. It could be that these unmotivated values are

137 simply experimental facts of nature without explanation, but the history of science
138 implies that a deeper understanding is likely hiding beneath the surface. Finally, the
139 observed value of the Higgs boson mass is not only unexplained, it is unnatural. This
140 final issue, which is explained in the following paragraphs, is a powerful motivation
141 to search for new physics at currently accessible energy scales.

142 **Naturalness**

143 The naturalness criterion states that an effective theory such as the SM must
144 not be overly sensitive to the details of the underlying higher energy theory. Put
145 another way, it requires that any dimensionless parameter much smaller than one
146 must be protected by a custodial symmetry [29]. Such a criterion may or may not be
147 respected by nature, but history and simple probability are on its side.

148 The dimensionless parameter in question is the mass of the Higgs boson, which is
149 quadratically sensitive to Λ , the energy scale at which a new theory takes over. All SM
150 parameters are affected by interactions with virtual particles through loop diagrams
151 such as those shown in Fig. 1.3, but the Higgs boson mass is particularly sensitive. As
152 a fundamental scalar, the Higgs boson lacks the chiral and gauge symmetries enjoyed
153 by the fermions and gauge bosons. These symmetries, known as custodial symmetries,
154 protect the fermion and gauge boson masses by guaranteeing that all corrections are
155 proportional to the bare masses themselves. If the SM is indeed valid up to M_P ,
156 then the bare mass of the Higgs boson must be coincidentally equal and opposite to
157 the sum of the terms that correct it to approximately one part in 10^{32} [28]. Such
158 miraculous fine tuning is technically possible, but it could also be strong evidence
159 that a deeper physical mechanism is at work.

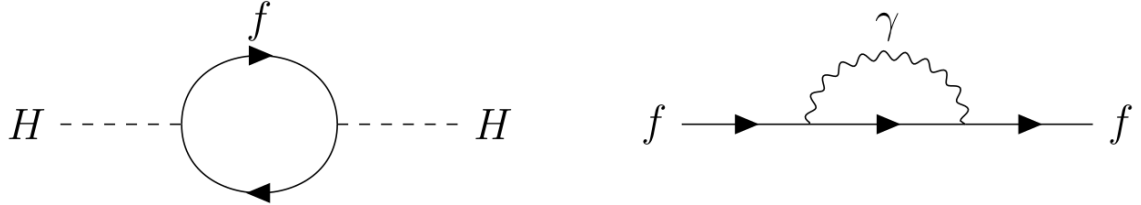


Figure 1.3: The Higgs boson mass corrected by a fermion loop (left) and a fermion mass corrected by photon loop (right).

160 1.2 Beyond the Standard Model

161 Many beyond the SM (BSM) theories have been proposed to address the issues
162 discussed in Section 1.1.4. Theories such as large extra dimensions address the unnat-
163 ural Higgs boson mass by allowing gravity to spread across more than three spatial
164 dimensions, which lowers M_P and therefore the size of the Higgs boson mass correc-
165 tions [30]. Other theories posit new symmetries that protect the Higgs boson mass
166 from large corrections. The following section explains supersymmetry, which protects
167 the Higgs boson mass with a new symmetry between bosons and fermions.

168 1.2.1 Supersymmetry

169 Supersymmetry (SUSY) introduces a new symmetry in which every SM particle
170 fits into a larger multiplet with an inherent symmetry between bosons and fermions.
171 In its simplest form, SUSY predicts one new boson for every SM fermion, one new
172 fermion for every SM boson, and one new Higgs doublet. The increase in particle
173 multiplicity necessitates a new naming convention: the spin-0 superpartners of the SM
174 fermions are called sfermions (e.g. sleptons or squarks) while the spin- $\frac{1}{2}$ superpartners

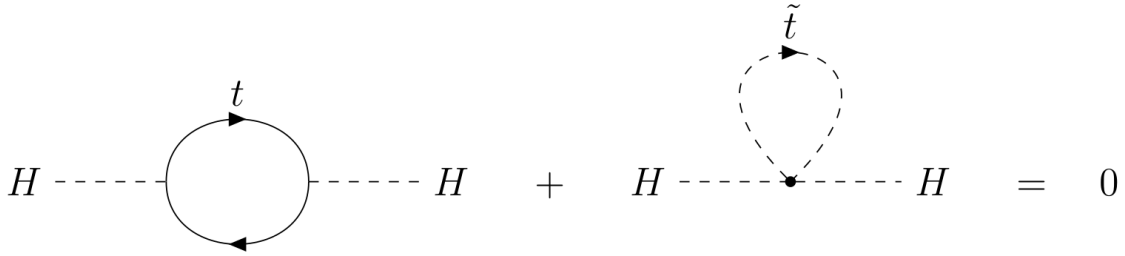


Figure 1.4: Corrections to the Higgs boson mass from the top quark (left) and top squark (right) cancel in exact SUSY. The top quark and top squark contributions are enhanced by the large coupling between the large Higgs-top quark coupling.

175 to the SM bosons add “ino” to the end of their SM counterpart (e.g. Higgsino or
176 wino).

177 When calculating contributions to the Higgs boson mass from loop diagrams, one
178 finds that fermion loops differ in sign from boson loops, which means that in SUSY
179 every bosonic correction to the Higgs boson mass is cancelled by a fermionic correction
180 and vice versa. If SUSY were an exact symmetry of nature, the cancellation would
181 be perfect, and the observed Higgs boson mass would match the bare Higgs boson
182 mass exactly [31]. Figure 1.4 shows a sample leading-order cancellation.

183 Exact SUSY also requires that SUSY particles have the same mass as their SM
184 counterparts, so the uniformly null results in collider searches imply that if SUSY
185 exists, it must be a broken symmetry. In broken SUSY, the diagrams in Fig. 1.4 no
186 longer exactly cancel. Instead, the resulting correction is proportional to the mass of
187 the top squark [32], which means that broken SUSY can still resolve the naturalness
188 problem if the masses of the SUSY particles that correct the Higgs boson mass are
189 themselves approximately at the weak scale (say $\mathcal{O}(250 \text{ GeV})$). Many natural SUSY
190 scenarios are therefore excluded as collider experiments set increasingly large lower

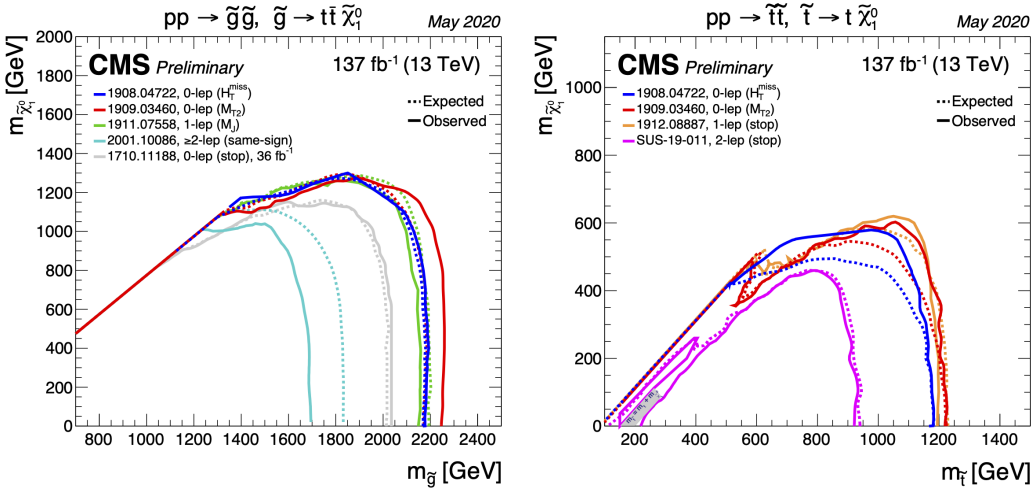


Figure 1.5: Mass limits at 95 % CL for a simplified model of gluino pair production with gluino decays to pairs of top quarks and the LSP (left) and top squark pair production with squark decays to a top quark and the LSP (right) from several CMS analyses [3].

¹⁹¹ bounds on SUSY particle masses. Figure 1.5, for example, shows that the exclusion
¹⁹² bounds on top squark and gluino masses extend above 1 TeV in several recent CMS
¹⁹³ analyses.

¹⁹⁴ As the available natural SUSY parameter space is further constricted, it is im-
¹⁹⁵ portant to investigate signatures of new physics that conventional analyses may be
¹⁹⁶ missing. One possibility, new long-lived particles, is presented in the following section.

¹⁹⁷ 1.2.2 Long-lived particles

¹⁹⁸ In the context of collider physics, long-lived particles (LLPs) are particles whose
¹⁹⁹ lifetimes are such that they decay a measurable distance from the collision point. This
²⁰⁰ category includes everything from particles that decay less than 1 mm away from the

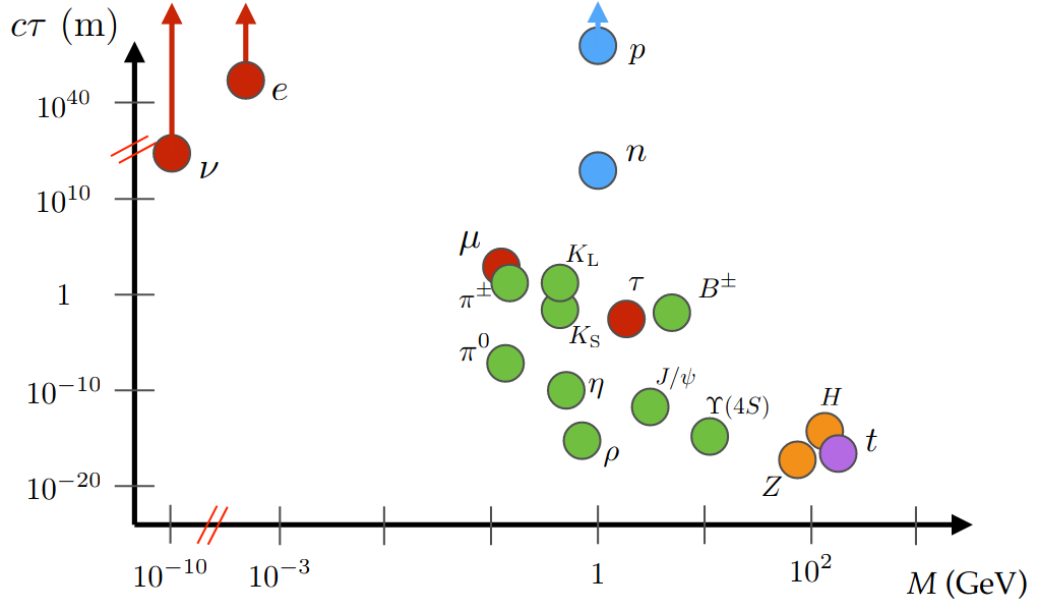


Figure 1.6: Masses and proper decay lengths of many Standard Model particles. Particles with proper decay lengths above approximately 10^{-4} m will be noticeably long-lived in collider detectors such as CMS [4].

201 collision to particles that propagate through the entire detector. As shown in Fig 1.6,
 202 long-lived particles are common in the SM.

203 Long-lived SM particles arise from several mechanisms. First, symmetries such as
 204 charge and baryon number conservation ensure that particles such as electrons and
 205 protons are absolutely stable. Second, small coupling constants and highly virtual
 206 intermediate states decrease the decay rate of particles such as muons, whose $2.2\ \mu\text{s}$
 207 lifetime is the product of a weak decay through a virtual W boson (the W boson mass
 208 is about 760 times that of the muon). Finally, limited decay phase space increases
 209 the lifetime of particles such as the neutron, whose decay into a proton, an electron,
 210 and an electron neutrino is slowed by the near mass degeneracy of the neutron and

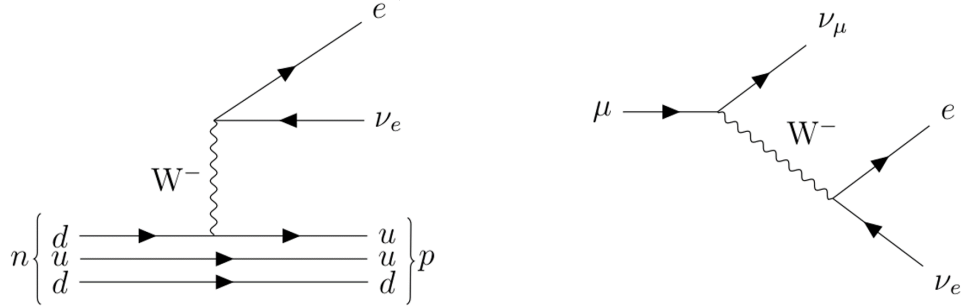


Figure 1.7: Long-lived decays of the neutron (left) and muon (right).

the proton. The mass difference between the neutron and its decay products is less than 1 MeV. The muon and neutron decays are diagrammed in Fig. 1.7.

In BSM physics, the same fundamental mechanisms could very well produce new long-lived particles. Many SUSY scenarios, for example, introduce a symmetry known as R parity that prevents proton decay. In models with exact R-parity conservation, SM particles are assigned R-parity 1 and SUSY particles are assigned R-parity -1 . Conserving the product of R-parity at each vertex has two phenomenological consequences: SUSY particles must be produced in pairs, and the lightest SUSY particle (LSP) must be absolutely stable. A neutral, weakly interacting LSP would therefore pass through most detectors (including the CMS detector described in Section 2.2) without interacting. The resulting momentum imbalance is a standard signature in many SUSY searches [33].

On the other hand, SUSY models with weakly coupled R-parity violating (RPV) terms produce long-lived but not perfectly stable LSPs. The following section will give a detailed overview of one such model. A similar situation arises in gauge-mediated SUSY breaking models where the gravitino is the LSP. The strength of the

227 coupling between the next-to-LSP (NLSP) and the gravitino is inversely proportional
228 to the energy scale at which SUSY is broken. A high SUSY breaking scale therefore
229 suppresses the NLSP decay rate, making it long lived [34].

230 LLPs also arise from particular SUSY mass spectra. Models in the Split SUSY
231 paradigm, for example, propose that the spin-0 SUSY particles are significantly more
232 massive than the spin- $\frac{1}{2}$ SUSY particles. In these models, the gluino becomes long
233 lived when its decay to two quarks and a neutral spin- $\frac{1}{2}$ SUSY particle is suppressed
234 by a highly virtual intermediate squark [35]. Other SUSY models produce long-lived
235 particles by limiting decay phase space. Some anomaly-mediated SUSY breaking
236 models, for example, predict that the NLSP and LSP are nearly degenerate in mass.
237 Just like the neutron decaying into a proton, the lack of available phase space sup-
238 presses the decay and produces a long-lived NLSP [36].

239 In summary, LLPs are a general feature of the SM, and it is reasonable to assume
240 that the same mechanisms that produce SM LLPs will also manifest in BSM physics.
241 The following subsection gives an overview of the phenomenology of the SUSY model
242 most relevant to the analysis presented in Chapter 3, while the experimental details
243 of this model and LLP searches at the LHC will be saved until after presenting the
244 LHC and CMS experiment in Chapter 2.

245 1.2.3 Displaced supersymmetry

246 As mentioned in Section 1.2.1, weak-scale SUSY has the potential to explain the
247 seemingly unnatural observed value of the Higgs boson mass. With this appealing
248 outcome in mind, experimental physicists have been searching for signs of SUSY
249 in high-energy particle collisions for the last few decades. In particular, searches

250 at the Large Hadron Collider, where the 7, 8, and 13 TeV proton-proton collisions
 251 could potentially be producing SUSY particles with masses above 1 TeV, are actively
 252 excluding large swaths of the natural SUSY parameter space. By examining the
 253 common assumptions behind a majority of these searches, the proponents of the
 254 Displaced SUSY model find an approach that avoids proton decay constraints while
 255 naturally producing long-lived SUSY particles that would be undetected by most
 256 collider searches [37].

257 Displaced SUSY is an RPV SUSY model that respects proton lifetime constraints
 258 by allowing terms that violate lepton number but not baryon number. The Minimal
 259 Supersymmetric Standard Model, which is a simple supersymmetric extension of the
 260 SM, allows the following baryon and lepton violating operators:

$$\frac{1}{2}\lambda''_{ijk}U_iD_jD_k, \frac{1}{2}\lambda_{ijk}L_iL_jE_k, \lambda'_{ijk}L_iQ_jD_k, \epsilon_iL_iH_u \quad (1.7)$$

261 where the first term violates baryon number and the remaining terms violate lepton
 262 number. The i, j, and k indices run over the three generations of fermions and U , D , L ,
 263 E , Q , and H refer to the SUSY multiplets whose SM components are right-handed
 264 up-type quarks, right-handed down-type quarks, left-handed leptons, right-handed
 265 leptons, left-handed quarks, and Higgs bosons, respectively [31]. Most SUSY models
 266 introduce R-parity to forbid all of these terms and therefore disallow proton decay,
 267 but this approach may be overkill: separately conserving either lepton number or
 268 baryon number is sufficient to prevent proton decay.

269 Such a situation can arise naturally if a gauge-unifying, R-parity-conserving $SU(5)$
 270 theory exists at high energies but is broken at lower energies [38]. In this scenario, the
 271 baryon-number-violating terms are suppressed and mixing between L and H becomes
 272 possible. The final term in expression (1.7) then dominates, and we are left with the

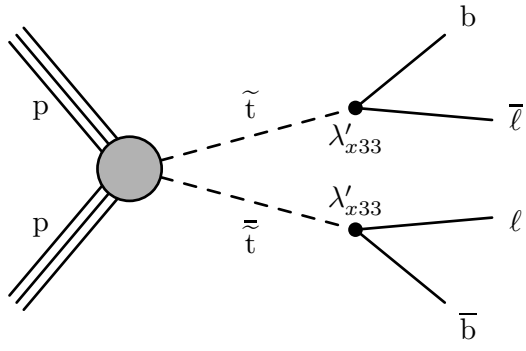


Figure 1.8: Pair-produced top squarks that each decay to a bottom quark and a lepton through an R-parity-violating LQD vertex.

²⁷³ following lepton-number-violating terms after rotating to the mass basis:

$$\epsilon_i y_{jk}^d L_i Q_j D_k, \quad \epsilon_i y_{jk}^e L_i L_j E_k \quad (1.8)$$

²⁷⁴ where the ϵ factors are lepton-Higgs mixing angles and the y factors are the Yukawa
²⁷⁵ coupling constants associated with the interactions between the fermions and the SM
²⁷⁶ Higgs field. Because these y factors are proportional to fermion mass, the lepton-
²⁷⁷ violating processes will favor third-generation fermions.

²⁷⁸ The dimensionless lepton-Higgs mixing angles are protected by the custodial R-
²⁷⁹ parity conservation of the higher-energy theory and will therefore naturally be small.
²⁸⁰ Just as in the SM, these small coupling constants can lead to macroscopic SUSY
²⁸¹ particle lifetimes that would evade most collider searches. In particular, long-lived
²⁸² LSP squarks can decay to a quark and charged lepton though a displaced vertex, as
²⁸³ in Fig. 1.8.

²⁸⁴ The unique experimental signature of processes such as the one shown in Fig. 1.8 is
²⁸⁵ a major motivating factor behind the analysis presented in Chapter 3. The particular
²⁸⁶ experimental consequences of such processes will be further explored in that context.

287 Chapter 2: The Large Hadron Collider and Compact Muon 288 Solenoid experiment

²⁸⁹ 2.1 The Large Hadron Collider

The Large Hadron Collider (LHC) is the highest-energy particle collider ever constructed. Located at the European Organization for Nuclear Research (CERN) and housed in a 27 km ring approximately 100 m below the French/Swiss countryside, the LHC is designed to accelerate two counter-rotating beams of protons to 7 TeV (and sometimes beams of heavy ions to 2.8 TeV) and collide them at four points around the ring. Each collision point is instrumented with a dedicated detector: the ATLAS (A Toroidal LHC ApparatuS) and CMS (Compact Muon Solenoid) experiments are general purpose detectors designed to reconstruct the remnants of proton-proton collisions at the highest collision rates offered by the LHC, LHCb (LHC beauty) studies b-quark decays from proton-proton collisions produced at lower collision rates, and ALICE (A Large Ion Collider Experiment) studies heavy-ion collisions [5]. Figure 2.1 shows the location of each experiment around the LHC ring. The analysis presented in Chapter 3 utilizes proton-proton collision data collected by the CMS experiment, and the following discussion is focused accordingly.

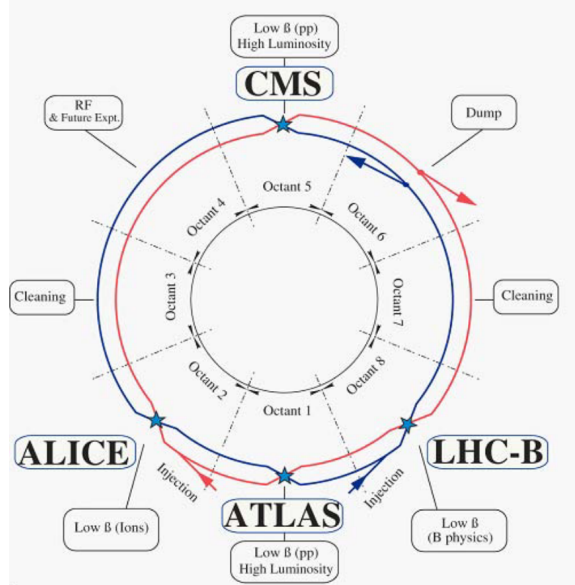


Figure 2.1: Layout of the LHC experiments [5].

2.1.1 Injection chain

The protons ultimately collided by the LHC must first travel through much of the CERN accelerator complex, which is diagrammed in Fig. 2.2. The 6.5 TeV proton beams relevant to this thesis start their journey as the nuclei of hydrogen atoms in a bottle of hydrogen gas. After having their electrons stripped away with an electric field, the protons are accelerated to an energy of 50 MeV with the Linac 2 linear accelerator [39]. The Proton Synchrotron Booster (PSB) next accelerates the protons to an energy of 1.4 GeV before injecting them into the Proton Synchrotron (PS) [40]. The PS was the first synchrotron constructed at CERN and was the highest-energy particle accelerator in the world at the time of its first operation [41]. Today, it accelerates protons to an energy of 25 GeV before passing them along to the Super Proton Synchrotron (SPS), which is the 7 km proton-antiproton collider at which the

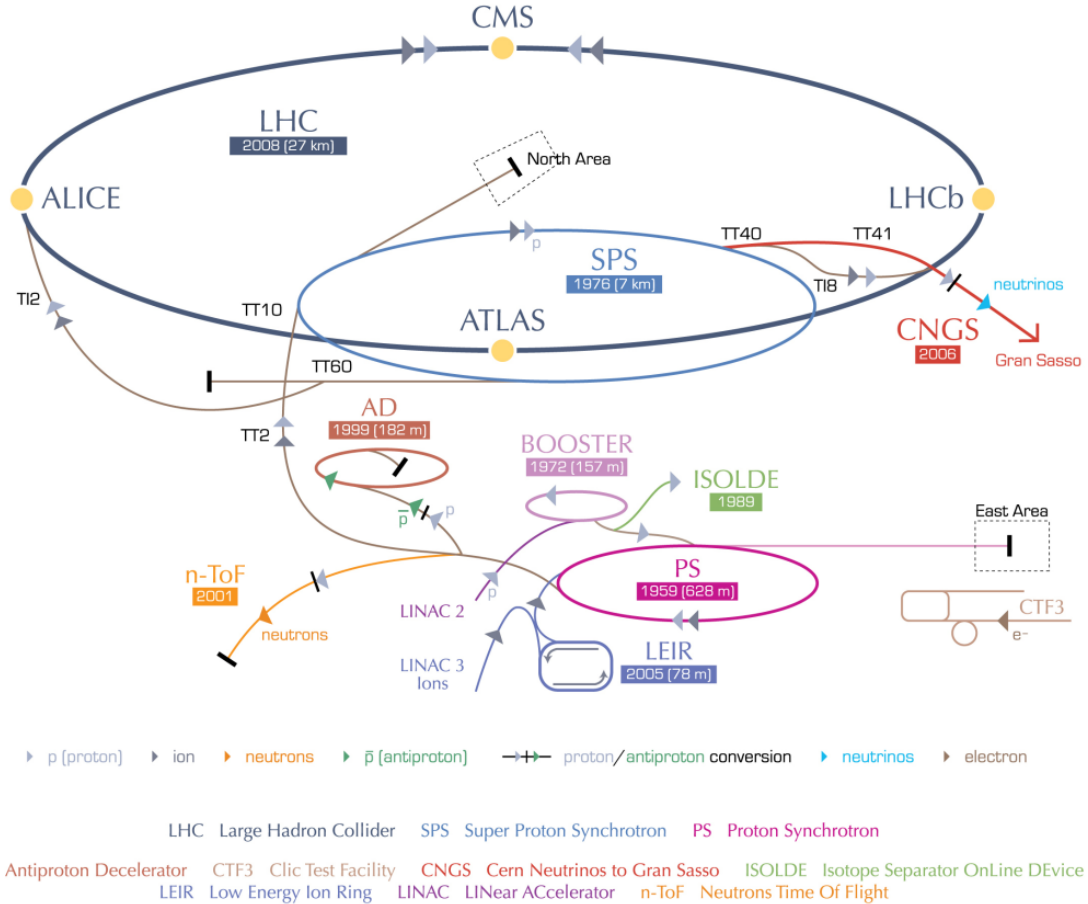


Figure 2.2: A diagram of the CERN accelerator complex. The analysis presented in Chapter 3 utilizes protons accelerated by LINAC 2, BOOSTER (also known as PSB), PS, SPS, and finally the LHC before their ultimate collision inside CMS [6].

³¹⁶ W^\pm and Z bosons were discovered in 1983 [42]. As the final step in the LHC injection
³¹⁷ chain, SPS accelerates protons to an energy of 450 GeV before injecting them into
³¹⁸ the LHC [5].

³¹⁹ 2.1.2 Main ring

³²⁰ Maximizing the physics potential of the LHC requires simultaneously maximizing
³²¹ the collision energy and the number of interesting collisions per unit time. The main

Table 2.1: Luminosity parameters used in Eq. (2.1).

Parameter	Description
N_b	Number of particles per bunch
n_b	Number of bunches per beam
f_{rev}	Revolution frequency
γ_r	Relativistic gamma factor
ϵ_n	Normalized transverse beam emittance
β^*	Beta function at collision point
F	Geometric luminosity reduction factor

322 LHC ring is therefore designed to accelerate the 450 GeV protons it receives from
 323 SPS to 7 GeV and collimate them into intense beams to be collided at high rates.
 324 The number of interesting collisions per unit time is ultimately the product of the
 325 total cross section of the processes one deems interesting, σ , and the instantaneous
 326 luminosity, L , which is given by:

$$L = \frac{N_b^2 n_b f_{rev} \gamma_r}{4\pi \epsilon_n \beta^*} F \quad (2.1)$$

327 where the parameters are defined as in Table 2.1 [5].

328 The LHC is designed to deliver a maximum instantaneous luminosity of
 329 $10^{34} \text{ cm}^{-2} \text{ s}^{-1}$ to ATLAS and CMS, but operational improvements, most notably a
 330 reduction in ϵ_n and β^* , have allowed the LHC to exceed this goal by up to a factor of
 331 approximately two in the 2016, 2017, and 2018 data-taking periods [7]. As shown in
 332 Fig. 2.3, the total integrated luminosity delivered during this period is approximately
 333 a factor of five times greater than that of the 2011–2012 period.

334 Increasing the number of interesting collisions per unit time comes with the unfor-
 335 tunate side effect of increasing the total number of collisions in each bunch crossing.
 336 Due to storage and processing limitations, the CMS and ATLAS detectors only record

337 data from the small subset of bunch crossing whose properties imply that they may
338 contain interesting processes (see Section 2.2.6). In a given bunch crossing, usually
339 only one collision is considered interesting. The remaining collisions, referred to as
340 “pileup”, add a layer of difficulty to collecting and analyzing the data while increasing
341 the total radiation dose that the detectors must withstand.

342 The ability to produce high-energy proton collisions at such high rates depends
343 on several impressive technological feats, notably the superconducting magnets that
344 steer and shape the beams and the superconducting radio-frequency (RF) cavities
345 that accelerate the protons and determine their bunch structure.

346 Superconducting magnets

347 The LHC magnet system relies on superconducting NbTi magnets that are cooled
348 to below 2 K with superfluid helium and are capable of producing fields in excess of
349 8 T. The design of the main dipole magnets that are responsible for keeping the beams
350 in a circular trajectory is heavily influenced by the size of the LHC tunnel, which orig-
351 inally housed the Large Electron-Positron Collider (LEP). Unlike LEP, which collided
352 particles and antiparticles, the LHC requires two separate beam pipes, each with its
353 own dipole magnetic field. This requirement, along with the limited tunnel cross
354 section, motivates the “two-in-one” magnet design in which both superconducting
355 magnets share a common cold mass and cryostat, as shown in Fig. 2.4 [5].

356 In addition to the main dipole magnets, the LHC also employs quadrupole magnets
357 for beam focusing and sextupole, octupole, and decapole magnets to correct the field
358 at the edges of the dipoles [5].

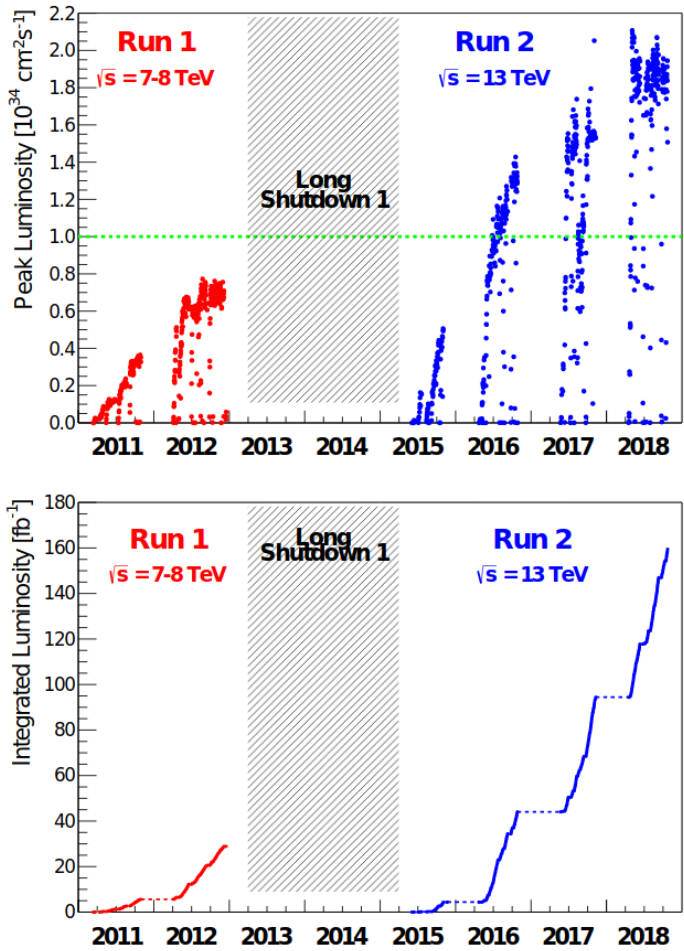


Figure 2.3: The peak instantaneous (top) and integrated (bottom) luminosity delivered by the LHC during proton operation between 2011 and 2018 [7].

LHC DIPOLE : STANDARD CROSS-SECTION

CERN AC/DI/MM - HE107 - 30.04.1999

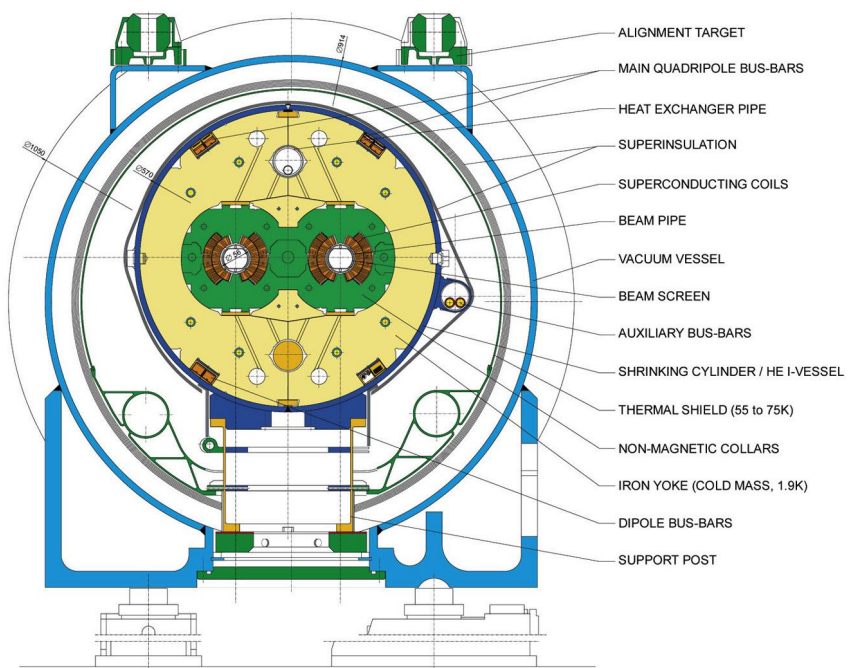


Figure 2.4: Diagram of an LHC dipole magnet in cross-section [8].

359 **Radio-frequency cavities**

360 An RF superconducting cavity system is responsible for capturing the 450 GeV
361 protons injected into the LHC from SPS, accelerating them to the full collision energy,
362 defining their bunch structure, and storing them. The main RF system operates
363 at 400 MHz and is located in Octant 4 (see Fig.2.1). Each RF cavity contains an
364 oscillating electromagnetic field whose phase is synchronized with the arrival of the
365 proton bunches such that the protons passing through the cavity always feel a force
366 in the direction of their motion. The applied force naturally varies for protons that
367 are slightly out of phase in such a way as to keep the protons tightly bunched in the
368 longitudinal direction [5].

369 2.2 The Compact Muon Solenoid experiment

370 The Compact Muon Solenoid experiment (CMS) is designed for the general study
371 of the highest-energy, highest-luminosity proton-proton (and heavy ion) collisions the
372 LHC can provide. The detector design is driven by the particular goals of explor-
373 ing physics at the TeV scale and discovering the origin of electroweak symmetry
374 breaking [43]. More than 4000 collaborators from institutions across more than forty
375 countries work together to collect and analyze the data using a global computing
376 grid [44].

377 To reconstruct the variety of particles that emerge from high-energy proton-proton
378 collisions, CMS uses several complimentary subdetectors nested radially about the
379 collision point. A 4 T superconducting solenoid magnet provides a powerful magnetic
380 field to bend the trajectories of charged particles, thus enabling the determination
381 of their momenta. Working from the center out, the CMS detector consists of an
382 all-silicon tracker, a lead-tungstate scintillating crystal electromagnetic calorimeter,
383 a sampling hadronic calorimeter composed of brass absorber and plastic scintillator
384 tiles, the superconducting solenoid magnet, and a muon system with three varieties
385 of gaseous detectors. Figure 2.5 shows the detector layout, and the remainder of this
386 chapter is devoted to a brief overview of each subsystem as well as the triggering and
387 reconstruction strategies employed by CMS.

388 CMS uses a right-handed coordinate system centered on the nominal collision
389 point with positive x direction pointing towards the center of the LHC ring and the
390 positive y direction pointing vertically upward. The azimuthal angle in the x - y plane,
391 denoted ϕ , is measured from the positive x axis, and the polar angle θ is measured
392 from the positive z axis. The angle from the z axis is more commonly described

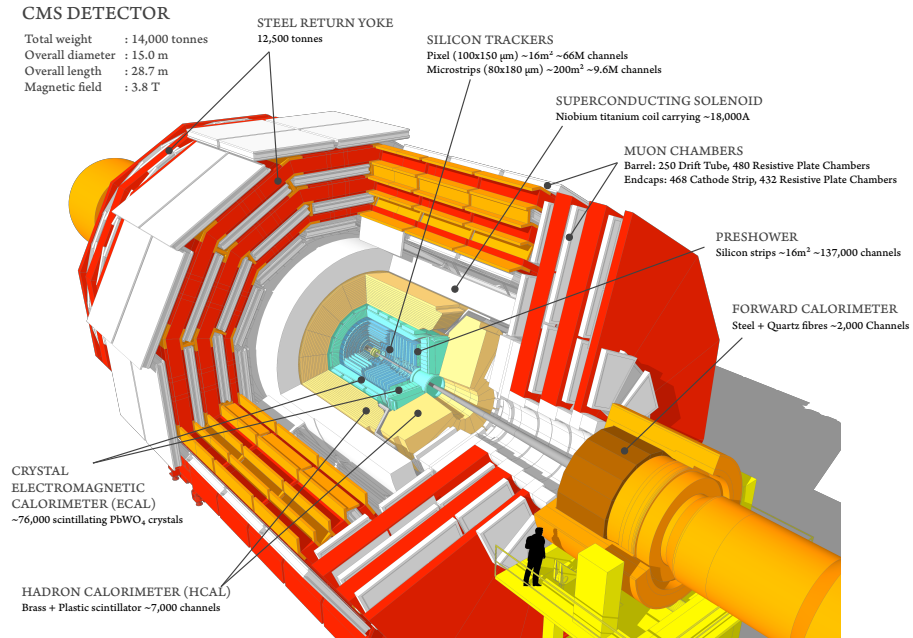


Figure 2.5: The CMS detector [9].

393 in terms of the pseudorapidity $\eta = -\ln \tan(\theta/2)$. Distances in the η - ϕ plane are
 394 commonly referred to as $\Delta R = \sqrt{(\Delta\eta)^2 + (\Delta\phi)^2}$. The component of the momentum
 395 that is transverse to the beam direction (i.e., in the x - y plane) is denoted p_T , and
 396 the magnitude of the negative vector sum of the p_T of all the reconstructed particles
 397 in an event is denoted p_T^{miss} . The magnitude of p_T is also sometimes referred to as
 398 transverse energy or E_T [14, 10].

399 The CMS detector has undergone several upgrades since its initial construction.
 400 The description presented here will focus on the detector conditions relevant to the
 401 analysis presented in Section 3.

402 **2.2.1 Solenoid magnet**

403 The superconducting solenoid is designed to produce a 4 T magnetic field through-
404 out the 6.3 m diameter, 12.5 m long cylindrical volume that contains the tracker and
405 calorimeters. The magnetic field is produced by running 19 kA through 2168 turns
406 of NbTi superconducting cable that are cooled with liquid helium. The flux returns
407 through an iron yoke that also houses the muon system [10].

408 The strong magnetic field is critical to CMS’s ability to unambiguously distinguish
409 muons and anti-muons with transverse momenta up to 1 TeV [14], and much of the
410 overall detector design is guided by the choice of a large superconducting solenoid.
411 The uniform magnetic field alters the trajectories of charged particles immediately
412 upon their production, which results in significant bending power within a relatively
413 small radius and therefore enables a compact detector.

414 The CMS solenoid stores a uniquely large amount of energy in its magnetic field
415 when compared to other collider detector magnets, especially when viewed relative to
416 its mass. To avoid deformations from the strong magnetic field, the superconducting
417 coils are reinforced with an aluminium alloy so that the coil layers themselves han-
418 dle 70% of the magnetic hoop stress. Figure 2.6 compares several collider detector
419 magnets in the energy/mass vs energy plane and shows a cross-sectional view of the
420 reinforced conductor coils in cross section. This approach allows for a relatively thin
421 solenoid that is less likely to scatter muons before they reach the muon system [10].

422 **2.2.2 Tracker**

423 In the region closest to the proton collisions, CMS employs a silicon tracker to re-
424 construct particle trajectories along with primary and secondary vertices. Efficiently

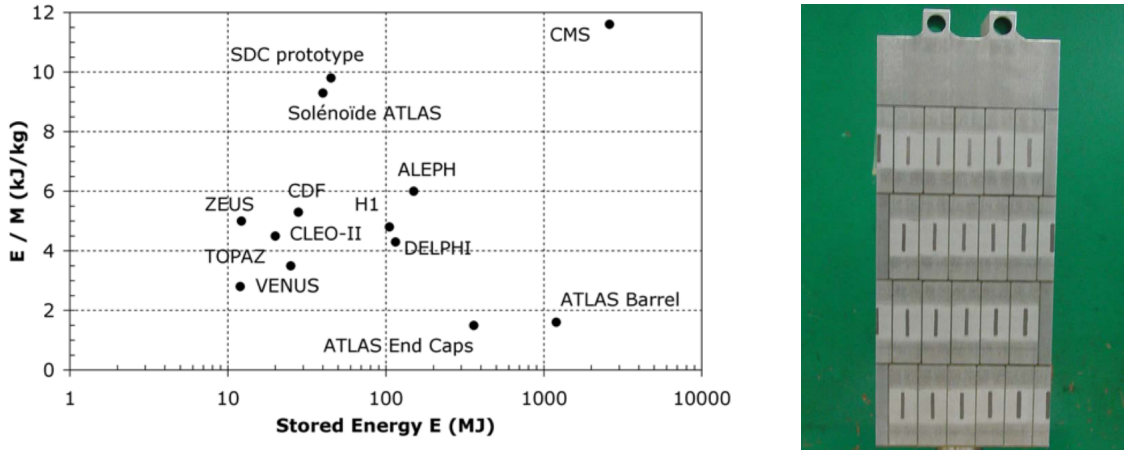


Figure 2.6: The stored-energy-over-mass ratio, E/M , for several detector magnets (left), and a cross-sectional view of the four-layer winding of reinforced conductor in the CMS superconducting solenoid (right) [10].

and accurately performing these tasks allows CMS to measure charged particle momenta, distinguish between particles from the primary and pileup vertices, and identify heavy-flavor decays. The high particle flux necessitates a highly granular, fast, and radiation hard detector that introduces the smallest possible amount of material to the region inside the calorimeters. The resulting detector contains over 200 m^2 of active silicon, making it the largest silicon tracker ever built. The tracker has a length of 5.8 m, a diameter of 2.5 m, and is divided into two subdetectors. Inside a radius of 20 cm, the particle flux demands the use of silicon pixel detectors, while silicon micro-strip detectors suffice in the region beyond 20 cm [10].

The pixel and strip detectors both utilize the same fundamental detection mechanism: the energy depositions of incident charged particles form electron-hole pairs when passing through the depletion region of a reverse-biased p-n junction, and the resulting induced current signifies the presence of a charged particle. The reverse bias

438 voltage sweeps away charge carriers to reduce thermal noise and maximize the sen-
439 sitive volume. The fine two-dimensional segmentation of the pixel detector provides
440 precise two-dimensional position measurements from a single detector layer, while
441 each strip detector layer only provides a one-dimensional location measurement. In
442 both cases, the detector planes are tilted to allow the charge liberated by a single
443 incident particle to spread across multiple pixels or strips. This scheme significantly
444 improves the position resolution by combining the charge measurements of multiple
445 adjacent pixels or strips.

446 The original pixel detector was replaced between the 2016 and 2017 data-taking
447 periods in preparation for higher luminosities [12]. As the analysis presented in Sec-
448 tion 3 uses data collected in 2016–2018 and is particularly dependent on tracker
449 measurements, the original pixel detector, 2017–2018 (Phase-1) pixel detector, and
450 strip detector are described separately below.

451 **Original pixel detector**

452 The original CMS pixel detector covers the $|\eta| < 2.5$ region and is composed of
453 three cylindrical barrel layers at $r = 4.4$, 7.3, and 10.2 cm and four endcap disks
454 34.5 and 46.5 cm up and down the beamline from the nominal collision point. Each
455 layer or disk is instrumented with several pixel modules that are each composed
456 of a silicon sensor bump bonded to custom ASIC read-out chips (ROCs). Each
457 sensor is 285 μm thick and typically comprises 66 560 $100 \times 150 \mu\text{m}$ pixels. The nearly
458 square pixel shape enables approximately 15 μm hit resolution in both the r - ϕ and z
459 directions [14, 10].

460 The silicon pixel sensors are composed of highly doped n-type silicon implants
461 in an n-type silicon substrate with a p-n junction on the opposite side. These “n-
462 on-n” sensors are more expensive than traditional “p-on-n” sensors but are chosen
463 for their radiation hardness. Specifically, the increased electron contribution to the
464 signal charge lessens the impact of the radiation-damage-induced reduction in carrier
465 lifetime [10, 33]. Signals whose analog pulse height exceeds a pre-determined value
466 (set individually for each pixel) are read out and amplified by the bump-bonded
467 ROCs. The resulting hit location and pulse height information are read out at each
468 L1 trigger (see Section 2.2.6).

469 The original pixel detector was designed for a maximum instantaneous luminosity
470 of $10^{34} \text{ cm}^{-2} \text{ s}^{-1}$, which corresponds to approximately 25 pileup collisions per bunch
471 crossing in CMS. As shown in Fig. 2.3, the LHC first exceeded this instantaneous
472 luminosity in 2016. Figure 2.7 shows the resulting hit efficiency loss in the inner-
473 most layer of the pixel detector as a function of instantaneous luminosity and pileup.
474 While the higher-radius pixel layers are less affected, important quantities such as the
475 transverse impact parameter resolution are highly dependent on the measurements of
476 the layer closest to the interaction. To mitigate this effect, CMS replaced the original
477 pixel detector between the 2016 and 2017 data-taking periods.

478 **Phase-1 pixel detector**

479 The Phase-1 pixel detector represents an incremental improvement over the orig-
480 inal CMS pixel detector: the same fundamental technology fills the same physical
481 footprint and reuses many of the existing services but nevertheless achieves higher
482 rate capabilities, improved radiation tolerance, and more robust tracking [12]. This

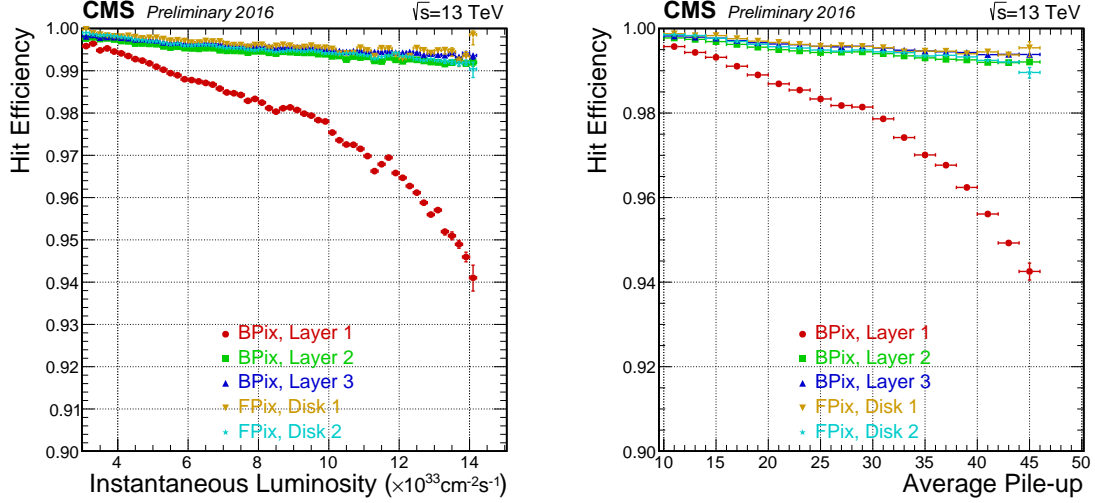


Figure 2.7: Measured single hit efficiency per layer as a function of the instantaneous luminosity (left) and pileup interactions (right) in data taken with the original CMS pixel detector in 2016 [11].

is accomplished by adding one additional layer to the barrel and each endcap, decreasing the radius of the innermost barrel layer to 2.9 cm, upgrading the ROCs, and reducing the material budget of the cooling system and mechanical structure [12, 45].

Figure 2.8 compares the geometries of the original and Phase-1 pixel detectors.

The loss of hit efficiency at high instantaneous luminosity observed in the original pixel detector is significantly reduced in the Phase-1 pixel detector. Despite the higher particle flux that accompanies the shift to a smaller radius, the Phase-1 innermost pixel layer maintains a single hit efficiency well over 98 % when operating at an instantaneous luminosity of $1.4 \times 10^{34} \text{ cm}^{-2} \text{s}^{-1}$ during the 2017 data-taking period [46]. Looking at Fig. 2.7, the equivalent quantity for the original pixel detector is approximately 94 %.

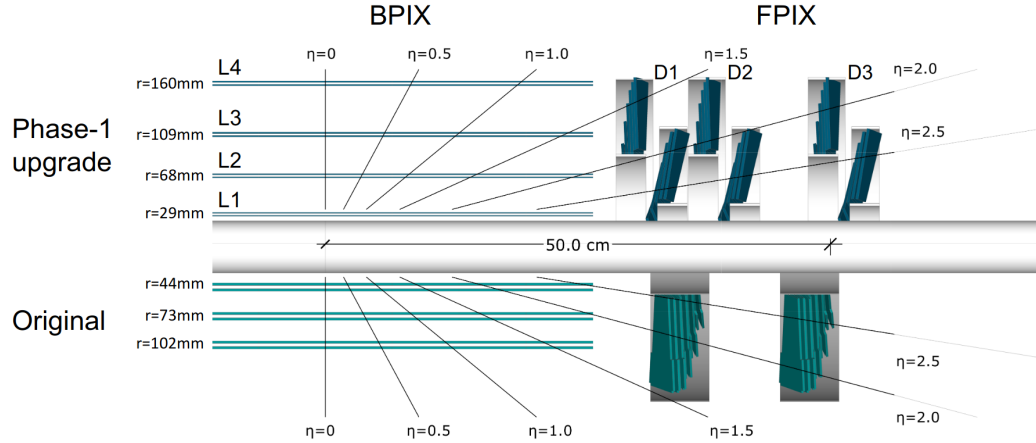


Figure 2.8: Comparison of the original and Phase-1 CMS pixel detector layouts in y - z plane [12].

494 Strip tracker

495 The strip tracker surrounds the pixel detector with silicon micro-strip sensors in
 496 10 cylindrical barrel layers between $r = 20\text{ cm}$ and $r = 110\text{ cm}$ and 12 disks on each
 497 side of the barrel detector that extend to $|z| = 282\text{ cm}$ and cover up to $|\eta| < 2.5$.
 498 The strip pitch generally increases with radius and results in hit resolutions that vary
 499 from 23 to $530\text{ }\mu\text{m}$ [10]. Figure 2.9 shows the layout of the entire silicon tracker.

500 Sitting farther from the interaction point allows the strip tracker to utilize more
 501 typical p-on-n type sensors that are composed of highly doped p-type silicon strips
 502 embedded in an n-type silicon substrate with a layer of highly doped n-type silicon
 503 on the side opposite the strips. As the n-type silicon substrate is slowly converted
 504 to p-type silicon by bulk radiation damage, the p-n junction moves from the strips
 505 to the back side of the sensor. Custom integrated circuits amplify, shape, and store
 506 the analog signals from each strip sensor. At each L1 trigger, the analog signals are

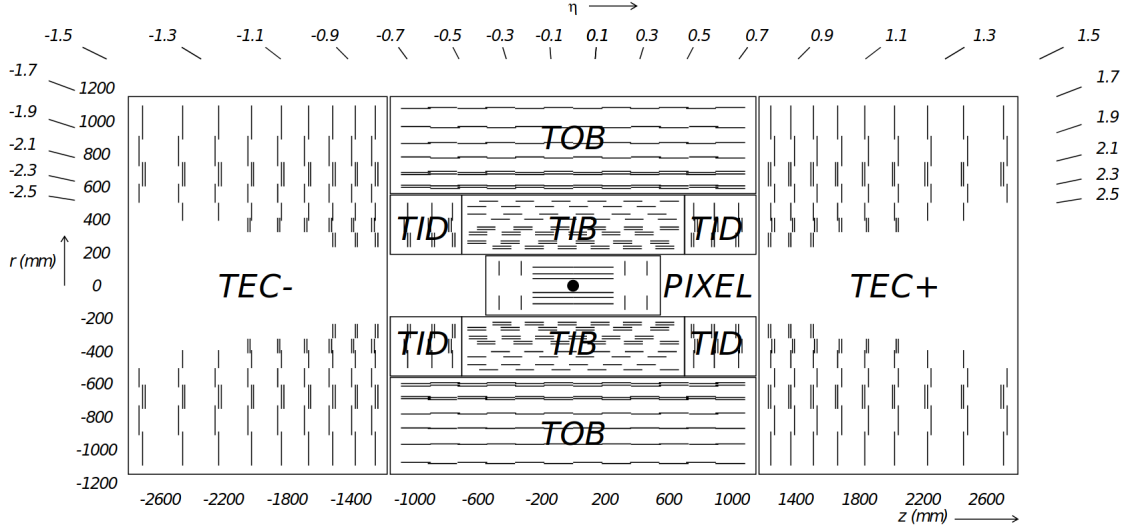


Figure 2.9: Layout of the CMS silicon tracker. TIB, TOB, TID, and TEC refer to subdetectors of the strip detector while PIXEL refers to the original pixel detector. The Phase-1 pixel detector is contained within the same volume [10].

507 transferred off-detector by optical fibers to be processed. Reading out the full analog
 508 information reduces the tracker material budget and need for custom radiation-hard
 509 electronics by performing analog-to-digital conversion, pedestal subtraction, and other
 510 processing outside the detector volume [10].

511 2.2.3 Electromagnetic calorimeter

512 After traversing the inner tracker, particles next encounter the electromagnetic
 513 calorimeter (ECAL). As a homogeneous scintillation calorimeter, ECAL uses 61 200
 514 lead tungstate crystals in the barrel and 7324 in each endcap to reconstruct the en-
 515 ergy deposited during electromagnetic showers. Lead tungstate crystals allow for
 516 a fast (80 % of light emitted within 25 ns), compact (radiation length = 0.89 cm),

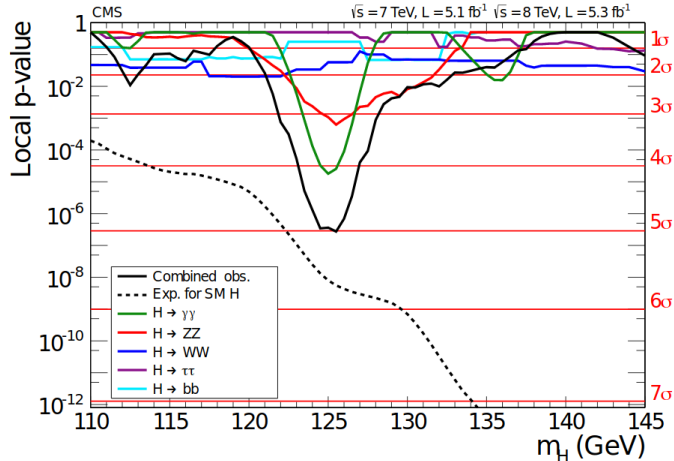


Figure 2.10: The observed local p-value for the five decay modes and the overall combination as a function of the SM Higgs boson mass showing the importance of the ECAL mass resolution in the discovery of the Higgs boson by the CMS experiment. The dashed line shows the expected local p-values for a SM Higgs boson with a mass m_H [13].

517 fine-grained (Molière radius = 2.2 cm), and radiation hard (up to 10 Mrad) calorime-
 518 ter. The main drawback is the relatively low light yield (30 photon/MeV), which
 519 necessitates photodetectors with intrinsic gain that work in magnetic fields [10, 14].

520 The ECAL performance requirements were heavily influenced by the possibility
 521 to reconstruct the decay of a Higgs boson to two photons [43]. Despite the small
 522 branching fraction and irreducible background, this decay channel provides a clean
 523 signature of a narrow mass peak on top of a smoothly falling background. Thanks in
 524 large part to the excellent ECAL energy resolution, the diphoton channel provided
 525 the largest significance and best mass resolution (approximately 1 GeV resolution at
 526 125 GeV) in the CMS Higgs boson discovery in 2012, as shown in Fig. 2.10 [13].

527 The barrel section extends radially from 129 to 177 cm and covers up to $|\eta| < 1.479$.
 528 The crystals are tapered to approximately project back to the nominal collision point

529 but not so perfectly that likely particle trajectories align with cracks. Each crystal is
530 approximately one Molière radius wide and 25 radiation lengths deep. The crystals
531 in each endcap section are arranged in an x - y grid that starts at $|z| = 315$ cm and
532 covers $1.479 < |\eta| < 3.0$.

533 2.2.4 Hadronic calorimeter

534 Particles that survive the ECAL will next encounter the hadronic calorimeter
535 (HCAL). As the ECAL constitutes approximately 25 radiation lengths but only one
536 interaction length, all but the particles that decay through the strong force will be
537 filtered out before reaching the HCAL. In addition to reconstructing the decays of
538 hadrons, the HCAL plays a particularly important role in measuring p_T^{miss} . By max-
539 imizing the coverage in η and overall amount of material in terms of interaction
540 lengths, HCAL ensures that nearly all particles (other than muons, neutrinos, and
541 hypothetical BSM particles) decay and deposit all their energy before reaching the
542 solenoid. Muon momentum is reconstructed with the tracker and muon system, so
543 only neutrinos and hypothetical BSM particles will contribute to p_T^{miss} . Reliable p_T^{miss}
544 measurements are particularly important when searching for new weakly interacting
545 particles with large lifetimes such as potential dark matter candidates or R-parity-
546 conserving LSPs that can pass through the detector without interacting.

547 With these goals and the constraint of fitting within the solenoid volume in mind,
548 HCAL is designed as a sampling calorimeter that uses 3.7 mm thick plates of plastic
549 scintillator interspersed within approximately 5 cm thick brass absorber plates to



Figure 2.11: Layout of the hadron calorimeter barrel (HB), outer (HO), endcap (HE), and forward (HF) subdetectors [10].

550 reconstruct the energy deposited during hadronic showers. Embedded wavelength-
 551 shifting fibers capture the scintillation light and transfer it to clear fibers to be read
 552 out by hybrid photodiodes.

553 The barrel section ($|\eta| < 1.4$) is segmented into 32 towers in η and 64 in ϕ that
 554 each contain 17 active scintillator layers. In the $|\eta| < 1.26$ range, an extra layer of
 555 scintillator tiles (or two at $\eta = 0$) sits just outside the solenoid and increases the
 556 minimum effective HCAL interaction length to greater than 11.8. Each endcap spans
 557 a pseudorapidity range of 1.3 to 3.0 with 14 towers in η and 5 to 10° ϕ segmentation.
 558 Also, a steel and quartz fiber forward calorimeter (HF) sits 11.2 m from the interac-
 559 tion point and covers $3 < |\eta| < 5$. In HF, particles produce Cherenkov light when
 560 traversing the quartz fibers that run parallel to the beamline. Figure 2.11 shows the
 561 layout of the barrel, endcap, and forward HCAL subdetectors.

562 **2.2.5 Muon system**

563 The CMS muon system is composed of three varieties of gaseous detectors em-
564 bedded in the iron return yoke outside the superconducting solenoid. In the central
565 region ($|\eta| < 1.2$), the low muon and neutron rates along with the lower magnetic field
566 allow the use of drift tube (DT) chambers. At higher η ($0.9 \leq |\eta| < 2.4$), cathode
567 strip chambers (CSCs) are required to handle the higher rates and larger magnetic
568 field. Finally, resistive plate chambers (RPCs), which provide more accurate time
569 measurements and worse spatial resolution than the DTs and CSCs, complement the
570 other detectors out to $|\eta| < 1.9$ [14, 47].

571 As shown in Fig. 2.12, the muon momentum resolution of the inner tracker is about
572 an order of magnitude better than that of the muon system for low- p_T muons. The
573 muon system is critical, however, for maintaining the $< 10\%$ momentum resolution
574 that is necessary to unambiguously differentiate muons and anti-muons up to 1 TeV.
575 In addition to improving muon reconstruction, the muon system provides information
576 to the L1 trigger (see Section 2.2.6) and is capable of triggering on muons with good
577 efficiency, high background rejection, and about 15–25% p_T resolution without input
578 from the rest of the detector.

579 The DTs are organized into four stations, each of which contain up to 70 DT
580 chambers that each measure the muon hit position in either the r - ϕ or z direction.
581 Each chamber is composed of two or three collections of four-layer groupings of 13
582 by 42 mm drift cells. As diagrammed in Fig. 2.13, a 2–4 m anode wire runs down the
583 center of each drift cell while electrode and cathode strips line the top, bottom,
584 and walls of the cell. The cells are filled with an Ar/CO₂ gas mixture that is ionized

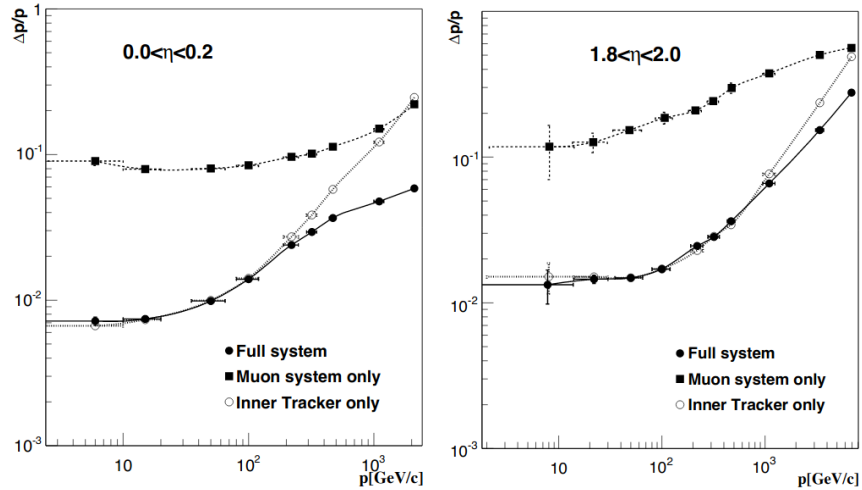


Figure 2.12: Muon momentum resolution as a function of momentum when using the CMS muon system, the CMS inner tracker, and the combination of the two subdetectors in two different η ranges [14].

585 by charged particles traversing the cell. The liberated electrons cause avalanches in
 586 the large electric fields before being collected by the anode wire.

587 Each endcap contains four CSC stations, each with six layers of CSCs whose cath-
 588 ode strips run radially outward to provide muon hit position measurements in the $r\phi$
 589 plane while the anode wires run in the azimuthal direction to provide measurements
 590 in η . As in the DTs, charged particles ionize a gas mixture inside each chamber (this
 591 time an Ar/CO₂/CF₄ mixture), which leads to an avalanche of electrons that are col-
 592 lected by an anode wire. In the CSCs, however, several anode wires share the same
 593 chamber and a two-coordinate position measurement is obtained by also reading out
 594 the induced charge on the perpendicular cathode strips.

595 The barrel and endcap regions also contain several RPC planes that ensure muons
 596 are associated with the correct bunch crossing and serve as a complementary muon

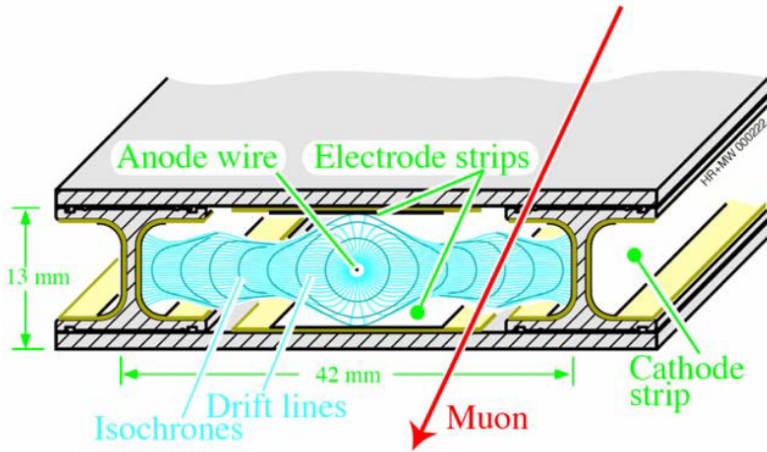


Figure 2.13: Sketch of a CMS muon system drift cell showing drift lines and isochrones. The plates at the top and bottom of the cell are at ground potential while the voltages applied to the electrodes are +3600 V for wires, +1800 V for strips, and -1200 V for cathodes [10].

trigger system. Each RPC plane is composed of parallel resistive plates separated by two 2 mm gas gaps. Charged particles ionize the gas, a voltage differential leads to an avalanche, and the total induced signal is read out as the sum of the induced signal in each gap. The double-gap approach allows for high efficiency operation with lower voltage differentials than would be required for a single gap. At lower voltages, the RPCs operate in ‘‘avalanche mode’’, which allows for stable performance and time resolution on the order of 2 ns despite particle fluxes up to hundreds of Hz cm^{-2} [10, 33, 48].

2.2.6 Trigger

The LHC provides bunch crossings to CMS at a nominal rate of 40 MHz. It is not possible to read out and store full event information at anywhere near this rate, so

608 the CMS trigger system is designed to identify the most interesting events to be read
609 out at approximately 1 kHz. The rate reduction happens in two stages: The Level-1
610 (L1) trigger and High-Level Trigger (HLT). The L1 trigger uses custom electronics
611 to analyze input from ECAL, HCAL, and the muon system to analyze each event in
612 less than 3.8 μ s and select potentially interesting events at a rate of approximately
613 100 kHz. The HLT, which is implemented in software on a dedicated processor farm,
614 uses information from all subdetectors to further reduce the rate to approximately
615 1 kHz [10, 49].

616 The L1 trigger processes calorimeter and muon system information in two separate
617 trigger systems before combining the two outputs in a global trigger system that
618 decides whether to pass a given event along to the HLT. The L1 algorithms are
619 implemented on field programmable gate arrays housed on boards that communicate
620 via optical link at 10 GB s^{-1} . The L1 Calorimeter Trigger uses coarsely segmented
621 information from ECAL and HCAL to reconstruct electron, photon, tau lepton, and
622 jet candidates, and the L1 Muon Trigger combines information from the DTs, CSCs,
623 and RPCs to reconstruct muon candidates [50].

624 The HLT utilizes more than 400 different algorithms (called “paths”) that run on a
625 farm of over 26 000 commercial processors. Each path runs a sequence of modules that
626 either reconstruct or filter physics objects. The modules are ordered such that the
627 fastest algorithms filter the object collections early, and the most resource-intensive
628 algorithms only run when necessary. HLT paths generally mimic the selection and
629 reconstruction algorithms used in CMS analyses, including the Particle Flow concept
630 described in the following section, but are more aggressively optimized to satisfy the
631 significant time and computing constraints imposed by the high event rate [49].

632 **2.2.7 Physics object reconstruction**

633 CMS uses a particle-flow (PF) algorithm to reconstruct the properties of individ-
634 ual particles from the combination of all subdetector measurements. Starting from
635 charged particle tracks from the tracker and muon system and clusters of energy
636 deposited in the ECAL and HCAL, CMS’s PF algorithm aims to reconstruct all
637 final-state electrons, muons, photons, and charged and neutral hadrons in a given
638 event. In this section, I first describe the reconstruction of tracks and energy clus-
639 ters before moving on to the individual particle identification and reconstruction. A
640 complete description of the CMS PF algorithm is available in Ref. [15].

641 **Charged particle tracks**

642 Charged particle tracks are reconstructed with an iterative procedure in which the
643 highest-purity algorithms are run first, and the hits associated with each reconstructed
644 track are masked before moving on to the next step. Despite the middling reconstruc-
645 tion efficiency of each individual step, this approach results in higher efficiency than
646 could be achieved with any single tracking algorithm and without meaningfully in-
647 creasing the rate of misreconstruction. This general principle applies to all charged
648 particle tracks, but the tracks associated with candidate electrons and muons receive
649 special consideration.

650 To better handle electron trajectories affected by radiative energy loss, CMS
651 employs a special iterative tracking procedure that includes a Gaussian-sum filter
652 (GSF) [51]. This approach improves the overall reconstruction efficiency, allows recon-
653 struction of lower- p_T electrons, and helps identify electrons from photon conversions
654 and distinguish electrons from charged hadrons.

655 Muon track reconstruction benefits from measurements in the tracker and the
656 muon system. Candidate muon tracks are placed in one of three categories depending
657 on which subdetectors are used in their reconstruction: standalone muon tracks only
658 use muon system hits; tracker muon tracks only use tracker hits and the requirement
659 of at least one consistent muon system hit; and global muon tracks are reconstructed
660 from a global fit of tracker and muon system hits.

661 **Calorimeter energy clusters**

662 Energy deposits in the calorimeters are clustered separately in ECAL and HCAL
663 with a Gaussian-mixture model that assumes the energy deposits arise from an arbi-
664 trary number of Gaussian energy deposits whose amplitude and location are allowed
665 to vary while the width is determined by the calorimeter properties. The clusters are
666 first seeded by cells with energy above some threshold and greater than the energy
667 of the surrounding cells. Nearby clusters are then merged before being fed to the
668 Gaussian-mixture algorithm. Finally, several corrections are applied to the cluster
669 energies to ensure accurate responses to photons and hadrons.

670 **Particle-flow reconstruction**

671 The tracks and clusters are then identified with and used to reconstruct all in-
672 dividual particles in an event. The first step is to link tracks and clusters together
673 into groups that correspond one or a few particles. Tracker tracks are extrapolated
674 outwards and linked with the nearest ECAL and HCAL clusters that are within a
675 set radius in the η - ϕ plane. In the case of candidate electron tracks, tracker tracks
676 and ECAL deposits consistent with electron radiative losses are also linked with the
677 candidate electron track. ECAL and HCAL clusters are similarly linked together by

678 proximity in the η - ϕ plane. Due to the high granularity of CMS subdetectors, the
679 number of tracks and clusters in a linked group is largely independent of the total
680 number of particles in an event.

681 Each group of linked tracks and clusters is then processed by the PF particle
682 identification and reconstruction algorithm. As in track reconstruction, particle re-
683 construction is an iterative process in which the tracks and clusters are masked after
684 being associated with a particle. Figure 2.14 diagrams the basic concept used to
685 identify muons, electrons, photons, and charged and neutral hadrons. Each step of
686 the PF algorithm is summarized below.

687 Muons are reconstructed first from isolated global muon candidates, then non-
688 isolated global muon candidates, and finally tracker muon (standalone muon) can-
689 didate tracks that are particularly well measured and consistent with hits in the
690 muon system (tracker). Muon momentum is taken from the tracker track when
691 $p_T < 200 \text{ GeV}$ and from the combination of tracker and muon system hits that yields
692 the best fit otherwise.

693 Electron and isolated photon reconstruction, which occur together after muon
694 reconstruction, are necessarily interrelated by the high probability that an electron
695 radiates a photon or a photon pair-produces electrons when interacting with tracker
696 material. Electrons are identified from GSF tracks with a corresponding ECAL cluster
697 while isolated photons are identified from isolated ECAL clusters. The total electron
698 energy accounts for radiative losses that show up as ECAL clusters, and both electrons
699 and isolated photons require a high ratio of ECAL cluster energy to nearby HCAL
700 cluster energy.

701 Next, nonisolated photons and charged and neutral hadrons are reconstructed
702 from the remaining tracks and clusters. Within the tracker acceptance ($|\eta| < 2.5$),
703 ECAL (HCAL) clusters without associated tracks are identified as photons (neutral
704 hadrons). At higher η , nearby ECAL and HCAL clusters are assumed to arise from the
705 same hadron shower and ECAL clusters without nearby HCAL clusters are identified
706 as photons. Discrepancies between track momenta and associated HCAL cluster
707 energy are also used to identify neutral hadrons and muons. Finally, a post-processing
708 step corrects for rare failure modes that can potentially produce inaccurately large
709 p_T^{miss} measurements.

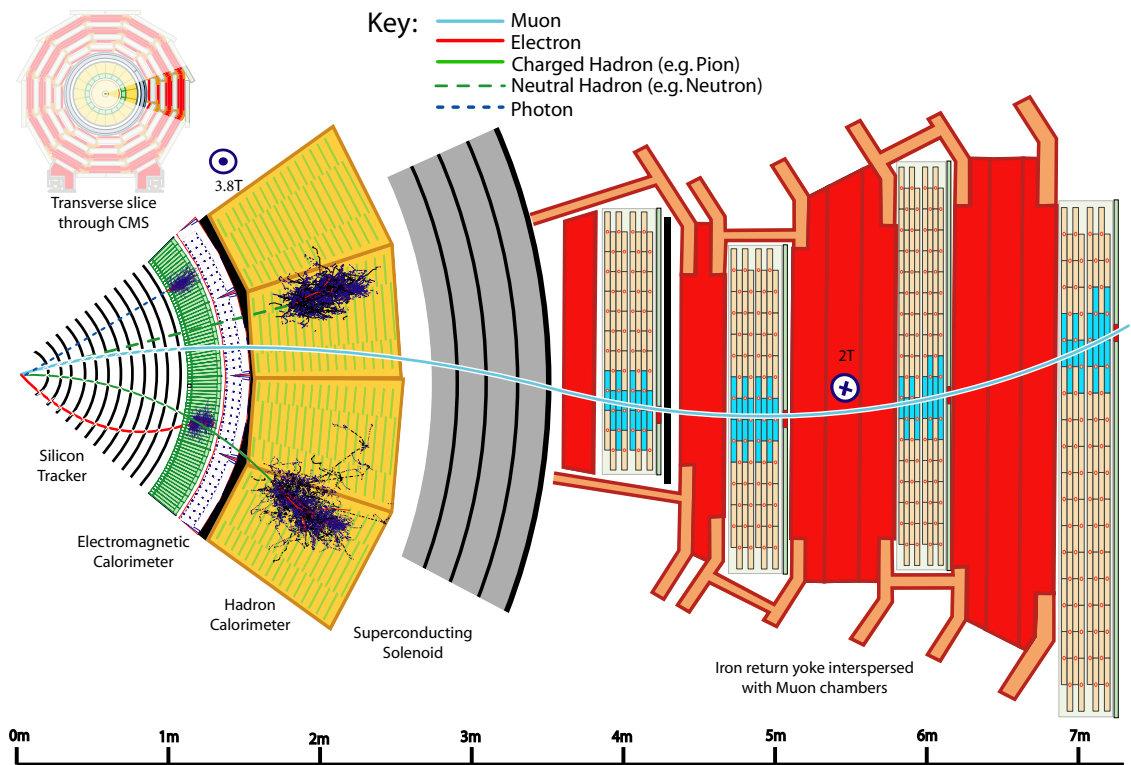


Figure 2.14: A sketch of a transverse slice of the CMS detector showing representative particle interactions used to identify and reconstruct particles with the CMS Particle Flow algorithm [15].

Chapter 3: Search for displaced leptons

711 In this chapter, I present a search for new long-lived particles that could be pro-
712 duced in proton-proton collisions at a center-of-mass energy of 13 TeV at the LHC
713 and detected by the CMS experiment. The search targets the unique signature of
714 “displaced leptons” that could be produced when long-lived particles decay to lep-
715 tons after propagating a measurable distance from the location of the proton-proton
716 collision. The candidate signal events include at least two leptons (one electron and
717 one muon, two electrons, or two muons) whose transverse impact parameters are
718 between 0.01 and 10 cm. Choosing transverse impact parameter as the main discrim-
719 inating variable allows us to target pairs of displaced leptons without requiring that
720 they form a common vertex. We apply an otherwise minimal event selection to retain
721 sensitivity to a wide range of new physics models.

722 The Ohio State CMS group has previously performed two related searches for
723 displaced leptons in the electron-muon final state: one in 19.7 fb^{-1} of 8 TeV data and
724 another in 2.6 fb^{-1} of 13 TeV data [52, 53]. The search presented here is the most
725 sensitive to date. Some of the most significant improvements include:

- 726
- adding sensitivity to the electron-electron and muon-muon final states

727

 - simplifying the event selection to reduce model dependence

- 728 • introducing a custom lepton isolation definition to significantly reduce the back-
729 ground from heavy-flavor meson decays
- 730 • implementing a new, fully data-driven background estimation procedure
- 731 • expanding the signal region to include leptons with smaller transverse impact
732 parameters
- 733 • adding a second signal interpretation
- 734 • analyzing more than a factor of 40 times more data than the previous 13 TeV
735 analysis [53]

736 The remainder of this chapter is organized as follows: Section 3.1 introduces the
737 displaced leptons experimental signature in the context of LLPs at the LHC and
738 gives an overview of the analysis strategy, Section 3.2 defines the data and simulated
739 SM and signal samples used in the analysis, Section 3.3 describes the event selection
740 criteria and defines the signal and control regions, Section 3.4 describes the various
741 corrections applied to the SM and signal simulation, Section 3.5 investigates the
742 sources of background and defines the procedure for estimating their contribution to
743 the signal region, Section 3.6 describes the sources of systematic uncertainty in the
744 efficiency for simulated signal events to pass the signal region selection, and Section 3.7
745 presents the results.

746 3.1 Overview

747 3.1.1 Long-lived particles at the LHC

748 As discussed in Section 1.2.2, LLPs are common in the SM and naturally arise in
749 many BSM scenarios. When produced in proton-proton collisions at the LHC, new

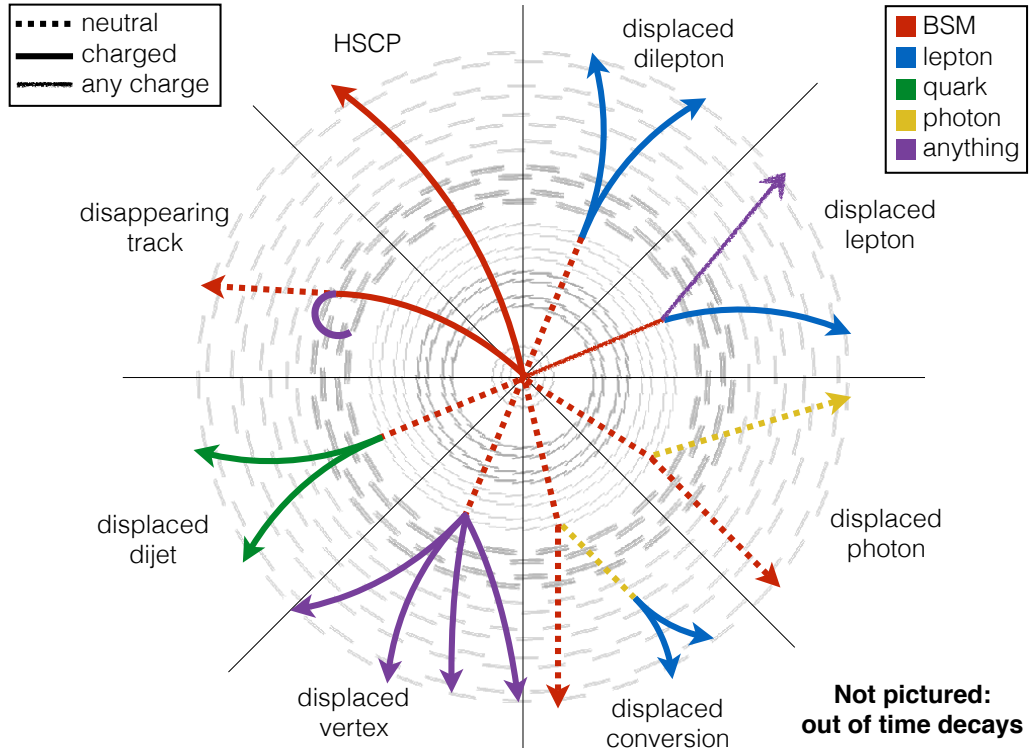


Figure 3.1: Illustration of several possible experimental signatures of long-lived particles [16].

750 LLPs have the potential to produce striking experimental signatures that differentiate
 751 them from SM backgrounds. As diagrammed in Fig. 3.1, new long-lived particles that
 752 decay within the detector volume can produce displaced vertices, physics objects
 753 whose trajectories do not point back to the location of the proton-proton collision,
 754 or particle tracks that vanish before reaching the outer edge of the tracker. Neutral
 755 LLPs that decay farther out can pass undetected through the tracker before producing
 756 signals in the calorimeters or muon system, and heavy, charged LLPs that are stable
 757 on detector length scales can be identified by their unusually large charge depositions.

758 The identification of any of these LLP signatures above the expected background
759 rates would be a clear sign of new physics, but their atypical nature adds an inherent
760 layer of difficulty to studying such signatures. In fact, standard reconstruction algo-
761 rithms and event selections frequently discard such unusual signatures and render the
762 majority of LHC analyses insensitive to many BSM scenarios that include LLPs [54].
763 As a solution to the naturalness problem may require new physics at the LHC energy
764 scale, it is critical that physicists face the challenges posed by LLP analyses and look
765 everywhere BSM physics may be hiding.

766 Interest in LLPs is growing as evidence of BSM physics continues to evade LHC
767 physicists. Recent CMS searches in 13 TeV proton-proton collisions target disappear-
768 ing tracks [55] or use the ECAL timing capabilities to target photons or jets whose
769 production at a displaced vertex delays the time of their detection [56, 57]. All ob-
770 servations thus far agree with SM predictions, but these and other LLP analyses are
771 probing regions of BSM parameter space that are untested by conventional analyses.

772 **3.1.2 Displaced leptons signature**

773 The Displaced Leptons analysis targets electrons and muons produced in the de-
774 cays of new, long-lived particles. Inspired by models such as Displaced SUSY (see
775 Section 1.2.3), we take care to maintain sensitivity to leptons that are produced in
776 separate long-lived decays as well as those that share a common displaced vertex.
777 This goal is achieved by selecting pairs leptons with large transverse impact param-
778 eters and setting no constraints on the presence or absence of displaced vertices.
779 Figure 3.2 shows the benefit of such an approach: the pair-produced new long-lived
780 particles, labeled X , each decay to a single lepton and an unspecified second particle.

CMS Simulation

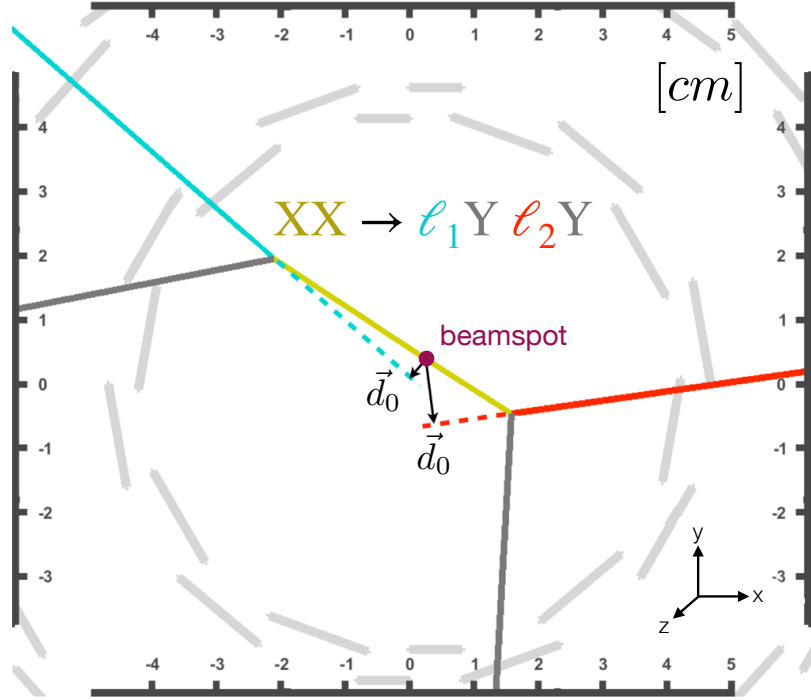


Figure 3.2: Illustration of the displaced leptons signature showing the definition of d_0 in a transverse view of the CMS detector. X denotes a new long-lived particle, ℓ denotes an electron or muon, and Y denotes any other decay products of the new long-lived particle. When interpreting the results of the Displaced Leptons analysis with the Displaced SUSY model, X refers to a top squark and Y refers to a b or d quark.

781 The lepton transverse impact parameter, which is labeled d_0 in the figure and defined
 782 explicitly below, is then used to identify the displaced nature of the lepton decays
 783 without explicitly constraining the other decay products in any way. Note also that
 784 the same strategy would successfully identify two leptons from a single long-lived
 785 particle decay.

786 Lepton transverse impact parameter, d_0 , is defined as the distance of closest ap-
 787 proach in the transverse plane of the helical trajectory of the lepton track to the CMS

788 beamspot, which is the center of the region in which the proton bunches cross. The
789 transverse impact parameter is commonly measured with respect to the primary ver-
790 tex, but in the case of leptons produced in displaced decays, the association between
791 a given primary vertex and the resulting leptons is unreliable. We determine d_0 from
792 measured properties of the lepton track using the following equation:

$$d_0 = \frac{(v_x - x_0)p_y - (v_y - y_0)p_x}{p_T} \quad (3.1)$$

793 where v_x and v_y refer to the x and y coordinates of the lepton track reference point,
794 which is usually chosen to be the point of closest approach to the center of CMS, x_0
795 and y_0 refer to the x and y coordinates of the beamspot, and p_x , p_y , and p_T refer to the
796 magnitudes of the x , y , and transverse components of the lepton's momentum. $|d_0|$
797 is commonly used throughout the Displaced Leptons analysis because we generally
798 care about the magnitude of d_0 but not its direction.

799 If we are to use lepton $|d_0|$ as the discriminating variable in an LLP search, we
800 must ensure it scales appropriately with the parent LLP lifetime. Typically, a particle
801 with lifetime τ will travel a distance $d = \beta\gamma c\tau$, where β and γ are relativistic factors
802 and c is the speed of light, so d and τ are directly correlated. Figure 3.2 shows that
803 lepton $|d_0|$ is determined by the distance travelled by the new LLP in the transverse
804 plane and the angle between the transverse momenta of the new LLP and the lepton.
805 Unless this angle is pathologically constrained to zero, $|d_0|$ and τ will be directly
806 correlated as well. In fact, the maximum value of lepton $|d_0|$, which occurs when
807 the angle between the transverse momenta of the new LLP and the lepton is $\frac{\pi}{2}$, is
808 exactly equal to the transverse distance between the beamspot and location of the
809 LLP decay.

810 Figure 3.3 shows the distribution of data and simulated Displaced SUSY events
811 in the plane defined by electron and muon $|d_0|$. As expected, the data events, which
812 are dominated by leptons from promptly decaying parent particles, are concentrated
813 at low $|d_0|$ values while the Displaced SUSY events are spread across the entire plane.
814 This figure shows the power of $|d_0|$ as a discriminating variable: requiring two leptons
815 with $|d_0| > 100 \mu\text{m}$ eliminates nearly all the SM background without requiring that
816 the leptons form a common vertex.

817 Another possible discriminating variable could be $|d_0|/\sigma_{|d_0|}$, where $\sigma_{|d_0|}$ is the
818 uncertainty in $|d_0|$. Such a discriminating variable could potentially reduce the back-
819 ground from leptons with poorly measured $|d_0|$, but we choose to use $|d_0|$ because of
820 its straightforward correspondence to the parent particle lifetime. We also find that
821 $\sigma_{|d_0|}$ is often underestimated, which reduces the potential benefit of using $|d_0|/\sigma_{|d_0|}$.

822 **3.1.3 Analysis strategy**

823 Having seen that $|d_0|$ can be used to identify leptons from long-lived particle decays
824 without requiring that the leptons form a common vertex, we now define a strategy
825 to target such a signature. The basic analysis strategy is outlined here and described
826 in detail in the following sections.

827 In addition to maximizing our sensitivity to models such as Displaced SUSY,
828 we also strive to develop an analysis that is model independent, signature based,
829 and easy to reinterpret. With these goals in mind, we perform a relatively simple
830 cut-and-count analysis in which our main event selection sets no constraints on any
831 non-lepton physics object. Unlike previous displaced leptons analyses [52, 53], we
832 allow final states with more than two leptons and set no constraints on the lepton

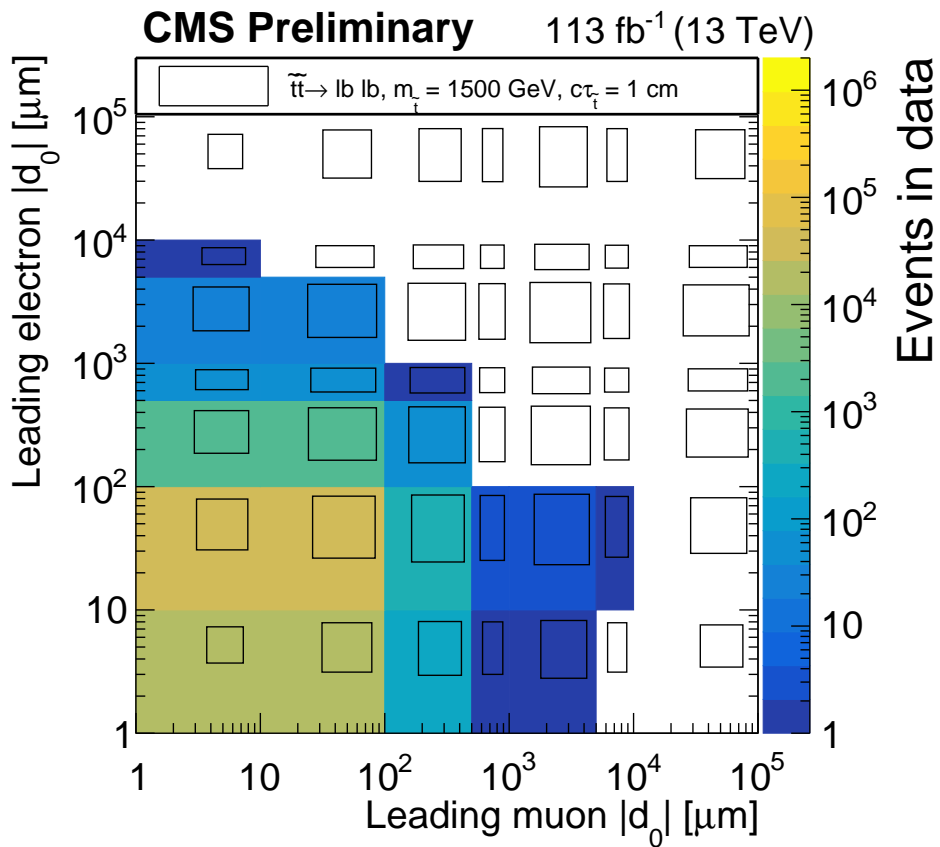


Figure 3.3: Distribution of data (colors) and simulated Displaced SUSY events (black boxes) in the plane defined by electron $|d_0|$ and muon $|d_0|$. The size of the black boxes are proportional to the bin content, and the bins along the x and y axes include underflow. All events are required to pass the $e\mu$ preselection defined in Section 3.3.

charge. As explained in Section 3.3, we select events in three analysis channels: electron-electron (ee), electron-muon ($e\mu$), and muon-muon ($\mu\mu$). We then divide the events into different regions of the plane defined by the $|d_0|$ of the two leptons that define the analysis channel. Figure 3.3, for example, shows this plane in the $e\mu$ channel. The signal region is defined as the region in which both leptons have $|d_0| > 100 \mu\text{m}$.

Following the procedure defined in Section 3.5, we use the data in the non-signal regions to estimate the SM background in the signal region. Finally, we compare the background estimates and data yields in the signal region. In the absence of a significant excess, we use simulated signal events to constrain the available parameter space of the Displaced SUSY model. To avoid biasing the result, we blind ourselves to the data in the signal region and wait to observe the signal-region data until after we define and test the entire analysis procedure and receive pre-approval from the CMS Exotica Physics Analysis Group.

847 **3.2 Data and simulated samples**

848 **3.2.1 Experimental data**

849 This analysis uses proton-proton collision data taken in 2016, 2017, and 2018 at
850 a center-of-mass energy of 13 TeV. In 2016, we use only the last two run periods due
851 to lower displaced tracking efficiency caused by an analog pipeline voltage saturation
852 problem in the silicon strip detector during the earlier run periods (see Appendix A).
853 In 2017, we use all run periods in the ee channel and all but the earliest run period
854 in the $e\mu$ and $\mu\mu$ channels because the $e\mu$ and $\mu\mu$ triggers are not available in the
855 earliest run period. In 2018, we use all available run periods in all three channels.
856 Ultimately, this analysis uses an integrated luminosity of $16.1 \pm 0.4 \text{ fb}^{-1}$ from 2016 in
857 all three channels, $41.5 \pm 1.0 \text{ fb}^{-1}$ ($36.7 \pm 0.8 \text{ fb}^{-1}$) from 2017 in the ee channel ($e\mu$
858 and $\mu\mu$ channels), and $59.7 \pm 1.5 \text{ fb}^{-1}$ from 2018 in all three channels.

859 The search is performed in the MuonEG, DoubleEG (in 2016–2017), EGamma (in
860 2018), and DoubleMu primary datasets. We also use the MET dataset to study the trig-
861 ger efficiency and the Cosmics and NoBPTX datasets to study the displaced tracking ef-
862 ficiency. All data are reconstructed in the 07Aug17, 31Mar2018, 17Sep2018 reprocess-
863 ing campaigns with software versions CMSSW_8_0_31, CMSSW_9_4_8, and CMSSW_10_2_0,
864 respectively. The sole exception is the EGamma 2018D dataset, which was reconstructed
865 in the 22Jan2019 campaign. In all cases, we use the CMS MiniAOD event format.

866 **3.2.2 Simulated background events**

867 This analysis employs a fully data-driven background estimation technique that
868 does not rely on simulated SM events. We do, however, use simulated SM events
869 to study possible sources of background and verify the validity of the background

estimation technique. The samples corresponding to 2016, 2017, and 2018 data conditions are from the `PdmVMCcampaignRunIISummer16`, `PdmVMCcampaignRunIIFall17`, and `PdmVMCcampaignRunIIAutumn18` production campaigns and were reconstructed in `CMSSW_8_0_31`, `CMSSW_9_4_8`, `CMSSW_10_2_0` with the MiniAODSIM event format. The samples simulating Z+jets, W+jets, and $t\bar{t}$ production are generated using `MADGRAPH5_aMC@NLO` [58, 59, 60], while the samples simulating diboson (WW, WZ, and ZZ with leptonic and semi-leptonic decays) and single-top-quark production are simulated with `POWHEG v2` [61, 62, 63, 64, 65]. `PYTHIA 8.2` [66] is used to simulate the parton showering and hadronization for all processes. The modeling of the underlying event is generated using the `CUETP8M1` [67] and `CP5` tunes [68] for simulated samples corresponding to the 2016 and 2017–18 data sets, respectively.

3.2.3 Simulated signal events

We use simulated signal events to guide the analysis strategy and interpret our results. Samples of simulated $pp \rightarrow \tilde{t}\tilde{t}$ events in which the top squarks decay to a lepton and a b quark or d quark are produced at leading order using `PYTHIA 8.2` [66]. For simplicity, all lepton flavors are generated with equal branching fractions. The top squarks can form strongly-produced hadronic states called R-hadrons, which are generated with `PYTHIA`. The interactions of the R-hadrons with matter are not simulated in `GEANT4`, but they are expected to have a negligible impact on the analysis because the lepton identification requirements effectively require the R-hadron to decay in the middle of the tracker volume. Each R-hadron therefore traverses $\lesssim 1$ interaction length, making it unlikely to produce a high quality track, come to a stop in the detector, or flip its charge. To generate the samples, we start with a SUSY

893 Les Houches Accord file [69] corresponding to Snowmass Points and Slopes point
894 1a [70] and modify the mass and width of the top squark according to the sample
895 being produced. We generate samples with top squark masses from 100 to 1800 GeV
896 at 100 GeV intervals and with top squark lifetimes at each decade from 0.1 mm to
897 1 m. After producing these samples, we also employ a lifetime reweighting technique
898 to effectively produce eight additional lifetime points between each pair of adjacent
899 lifetimes. In the case of the 1 m samples, we also use an equivalent technique to ef-
900 fectively produce nine additional lifetime points between 1 and 10 m. The production
901 cross sections for each top squark mass hypothesis are taken from the website of the
902 LHC SUSY Cross Section Working Group and reproduced in Table 3.1. The signal
903 samples are reconstructed in the same campaigns and with the same conditions as
904 the SM background samples described in 3.2.2.

Table 3.1: The top squark production cross sections used when generating the simulated $\tilde{t}\tilde{t} \rightarrow \bar{l}b\bar{l}b$ and $\tilde{t}\tilde{t} \rightarrow \bar{l}d\bar{l}d$ events. Cross sections are calculated at NLO + NLL by the LHC SUSY Cross Section Working Group.

\tilde{t} mass [GeV]	Cross section [pb]	Cross section uncertainty
100	1.52×10^3	15 %
200	6.45×10^1	14 %
300	8.52×10^0	14 %
400	1.84×10^0	14 %
500	5.18×10^{-1}	13 %
600	1.75×10^{-1}	13 %
700	6.70×10^{-2}	13 %
800	2.83×10^{-2}	14 %
900	1.29×10^{-2}	15 %
1000	6.15×10^{-3}	16 %
1100	3.07×10^{-3}	17 %
1200	1.60×10^{-3}	19 %
1300	8.50×10^{-4}	20 %
1400	4.61×10^{-4}	22 %
1500	2.56×10^{-4}	24 %
1600	1.41×10^{-4}	27 %
1700	8.08×10^{-5}	29 %
1800	4.67×10^{-5}	31 %

905 **3.3 Event selection**

906 **3.3.1 Triggers**

907 The events are required to pass different triggers in each channel. Standard CMS
908 electron and muon triggers are not designed for displaced objects, so we use non-
909 standard triggers for both electrons and muons. For muons, we remove all trigger
910 requirements relating to the muon d_0 , longitudinal impact parameter (d_z), or the ver-
911 tex from which the muon originates. For electrons, we actually use photon triggers,
912 which collect events with electrons as well as photons but do not rely on any tracking
913 information. See Section 2.2.6 for a brief overview of the CMS trigger system.

914 In the $e\mu$ channel, 2016 data and corresponding simulated events are required to
915 pass the logical OR of two HLT paths (`HLT_Mu38NoFiltersNoVtx_Photon38_CaloI`
916 `dL_v*` OR `HLT_Mu28NoFiltersNoVtxDisplaced_Photon28_CaloIdL_v*`) that were
917 both originally designed for the 2015 CMS displaced leptons analysis [53]. The first
918 trigger requires at least one muon with $p_T > 38 \text{ GeV}$ and places no constraints on the
919 vertex, d_0 , or d_z . The second trigger requires at least one muon with $p_T > 28 \text{ GeV}$
920 and $|d_0| > 0.01 \text{ cm}$. Each of these two triggers also requires at least one photon that
921 passes a loose calorimeter-based identification. The first (second) trigger requires
922 that the photon E_T is greater than 38 GeV (28 GeV). The signal efficiency with these
923 dedicated triggers is significantly higher than that of standard muon-photon HLT
924 paths.

925 In 2017 and 2018, data and corresponding simulated events in the $e\mu$ channel are
926 required to pass `HLT_Mu43NoFiltersNoVtx_Photon43_CaloIdL_v*`. The muon p_T
927 and photon E_T thresholds are raised with respect to 2016 due to increased pileup. A

928 version of the 2016 trigger that requires displaced muons is not available in 2017 and
929 2018.

930 In the ee channel, 2016 data and corresponding simulated events are required to
931 pass the logical OR of two HLT paths (`HLT_Diphoton30_18_R9Id_OR_IsoCaloId_A`
932 `ND_HE_R9Id_Mass90_v*` OR `HLT_DoublePhoton60_v*`). The first requires a leading
933 photon with $E_T > 30$ GeV and a subleading photon with $E_T > 18$ GeV. Photons must
934 pass calorimeter identification criteria involving isolation, the ratio of HCAL to ECAL
935 energy, and shower shape, and the di-photon invariant mass must be > 90 GeV. This
936 path is highly efficient at low top squark mass. The second trigger simply requires at
937 least two photons with $E_T > 60$ GeV. This path is highly efficient at large top squark
938 mass and lifetime.

939 In 2017 and 2018, data and corresponding simulated events in the ee channel are
940 required to pass `HLT_Diphoton30_22_R9Id_OR_IsoCaloId_AND_HE_R9Id_Mass90_v*`
941 OR `HLT_DoublePhoton70_v*`. The photon E_T thresholds are raised with respect to
942 2016 due to increased pileup.

943 In the $\mu\mu$ channel, 2016 data and corresponding simulated events are required to
944 pass the logical OR of two HLT paths (`HLT_DoubleMu33NoFiltersNoVtx_v*` OR
945 `HLT_DoubleMu23NoFiltersNoVtxDisplaced_v*`) that were both designed for this
946 analysis. The first trigger requires at least two muons with $p_T > 33$ GeV and sets no
947 constraints on the vertex, d_0 , or d_z . The second trigger requires at least two muons
948 with $p_T > 23$ GeV and $|d_0| > 0.01$ cm. The signal efficiency with these dedicated
949 triggers is significantly higher than that of standard di-muon HLT paths.

950 In 2017 and 2018, data and corresponding simulated events in the $\mu\mu$ channel are
951 required to pass `HLT_DoubleMu43NoFiltersNoVtx_v*`. The muon p_T threshold is

952 raised with respect to 2016 due to increased pileup. A version of the 2016 trigger that
953 requires displaced muons is not available in 2017 and 2018.

954 **3.3.2 Preselection**

955 Starting from the events collected with the triggers described above, we next apply
956 a set of preselection criteria to select the events to be analyzed. The preselection
957 criteria vary by channel and year, but the fundamental goal is always to select events
958 with at least one good reconstructed lepton of each flavor required by the channel.

959 Specifically, the $e\mu$ preselection selects events with at least one PF electron and
960 at least one global PF muon, the ee preselection selects events with at least two PF
961 electrons, and the $\mu\mu$ preselection selects events with at least two global PF muons
962 (see Section 2.2.7 for a discussion of the PF algorithm). We set requirements on these
963 electrons and muons as shown in Tables 3.2, 3.3, and 3.4. The electron and muon
964 p_T requirements are chosen such that the trigger efficiency is independent of lepton
965 p_T (see Section 3.4.4), while electron and muon $|\eta|$ requirements are chosen to reduce
966 the fraction of leptons with poorly measured d_0 (see Appendix B). Electrons that
967 traverse the gap between the endcap and barrel detectors are also rejected due to the
968 known decrease in reconstruction performance in this region.

969 We use a tight cut-based identification (ID) on the electrons and muons to select
970 well-reconstructed leptons, but unlike the standard ID definitions used in many CMS
971 analyses, we do not place any requirements on d_0 or d_z . In all other respects, we
972 follow the cut-based ID recommendations of the CMS EGamma and Muon Physics
973 Object Groups. The electron ID corresponds to `egmGsfElectronIDs:cutBasedElectron`
974 `ID-Summer16-80X-V1-tight` in 2016, `egmGsfElectronIDs:cutBasedElectron`

Table 3.2: The $e\mu$ preselection criteria. The electron and muon p_T thresholds increase in 2017 in accordance with the increased HLT electron and muon p_T thresholds.

Selection variable	Object-level selections		
	Electron	Muon	Muon
Number	≥ 1	≥ 1	≥ 1
p_T	$> 42 \text{ GeV}$ (2016) $> 45 \text{ GeV}$ (2017 and 2018)	$> 40 \text{ GeV}$ (2016) $> 45 \text{ GeV}$ (2017 and 2018)	
$ \eta $	< 1.5	< 1.5	
	not in ECAL gap	-	
$\eta - \phi$	veto ($1.0 < \eta < 1.5$ and $\phi > 2.7$) (2017) veto ($0.3 < \eta < 1.2$ and $0.4 < \phi < 0.8$) (2018)	veto ($1.0 < \eta < 1.5$ and $\phi > 2.7$) (2017) veto ($0.3 < \eta < 1.2$ and $0.4 < \phi < 0.8$) (2018)	
ID	Tight (cut-based)	Tight (cut-based)	Tight (cut-based)
Custom isolation	Tight	Tight	Tight
	Event-level selections		
	Zero $\mu\mu$ pairs with $\cos \alpha < -0.99$ Reject $\Delta t < -20$, if both timing ndof > 7 At least one $e\mu$ pair with $\Delta R(e, \mu) > 0.2$ Reject events with candidate leptons form a displaced vertex in the tracker material		

Table 3.3: The ee preselection criteria. The electron p_T threshold increase in 2017 and 2018 in accordance with the increased HLT electron p_T threshold.

Selection variable	Object-level selections	
Number	Electron	
p_T	≥ 2 $> 65 \text{ GeV}$ (2016) $> 75 \text{ GeV}$ (2017 and 2018)	
$ \eta $	< 1.5 not in ECAL gap	
$\eta - \phi$ (pixel power supply issue)	veto ($1.0 < \eta < 1.5$ and $\phi > 2.7$) (2017) veto ($0.3 < \eta < 1.2$ and $0.4 < \phi < 0.8$) (2018)	
ID	Tight (cut-based)	
Custom isolation	Tight	
	Event-level selections	
	At least one ee pair with $\Delta R(e, e) > 0.2$	
	Reject events with candidate leptons form a displaced vertex in the tracker material	
	Reject events with displaced muons in the $e\mu$ channel inclusive signal region	

Table 3.4: The $\mu\mu$ preselection criteria. The muon p_T threshold increase in 2017 and 2018 in accordance with the increased HLT muon p_T threshold.

Selection variable		Object-level selections	
Number	Muon	≥ 2	
p_T		$> 35 \text{ GeV (2016)}$ $> 45 \text{ GeV (2017 and 2018)}$	
$ \eta $		< 1.5	
		$\eta - \phi$ (pixel power supply issue)	veto ($1.0 < \eta < 1.5$ and $\phi > 2.7$) (2017) veto ($0.3 < \eta < 1.2$ and $0.4 < \phi < 0.8$) (2018)
ID		Tight (cut-based)	
Custom isolation		Tight	
		Event-level selections	
		Zero $\mu\mu$ pairs with $\cos\alpha < -0.99$	
		Reject $\Delta t < -20$, if both timing ndof > 7	
		At least one $\mu\mu$ pair with $\Delta R(\mu, \mu) > 0.2$	
		Reject events with candidate leptons from a displaced vertex in the tracker material	
		Reject events with displaced electrons in the $e\mu$ channel inclusive signal region	

Table 3.5: The electron tight ID requirements, which are identical to the tight cut-based ID from the CMS EGamma Physics Object Group with the d_0 and d_z requirements removed. Electron ID quantity definitions are available in Ref. [1].

Electron ID requirements	
full5x5 $\sigma_{in\eta} <$	0.0104 (2018, 2017) 0.00998 (2016)
$ \delta\eta_{\text{Seed}} <$	0.00255 (2018) 0.00353 (2017) 0.00308 (2016)
$ \delta\phi_{\text{In}} <$	0.022 (2018) 0.0499 (2017) 0.0816 (2016)
H/E <	0.026 + 1.15/E + 0.0324 ρ /E (2018) 0.026 + 1.12/E + 0.0368 ρ /E (2017) 0.0414 (2016)
PF isolation <	0.0287 + 0.506/ p_T (2018) 0.0361 (2017) 0.0588 (2016)
$ 1/E - 1/p <$	0.159 (2018) 0.0278 (2017) 0.0129 (2016)
expected missing inner hits \leq	1
pass conversion veto	yes

975 ID-Fall17-94X-V1-tight in 2017, and `egmGsfElectronIDs:cutBasedElectronID`
 976 -Fall17-94X-V2-tight in 2018. The electron and muon tight ID requirements are
 977 summarized in Tables 3.5 and 3.6.

978 We also require that electrons and muons are isolated. Specifically, we use a
 979 modified isolation definition that accounts for the fact that displaced leptons may
 980 be associated with the wrong primary vertex. The standard PF isolation assumes
 981 all energy from primary vertices other than the leading primary vertex is due to

Table 3.6: The muon tight ID requirements, which are identical to the tight cut-based ID from the CMS Muon Physics Object Group with the requirements on d_0 and d_z removed.

Muon ID requirements
Is a global muon
Is a PF muon
χ^2/n_{dof} of the global-muon track fit is < 10
At least one muon-chamber hit included in the global-muon track fit
Muon segments in at least two muon stations
At least 1 valid pixel hit
At least 6 tracker layers with hits

982 pileup, which is not true when the primary vertex ordering is altered by an incorrectly
 983 associated lepton. We have therefore modified the isolation definition to be agnostic
 984 to the primary vertex ordering by allowing PF candidates from any primary vertex
 985 to contribute to the isolation sum and by using a simple ρ -based pileup correction,
 986 where ρ is the total transverse energy of all the PF candidates in an event divided by
 987 the total detector area. The modified isolation is calculated as:

$$\text{relative isolation} = \frac{\max(0, p_T^{h^\pm} + E_T^{h^0} + E_T^\gamma - \rho\pi R^2)}{p_T^\ell} \quad (3.2)$$

988 where R is the radius of a cone in the η - ϕ plane that is centered on the lepton, $p_T^{h^\pm}$ is
 989 the total p_T of charged hadrons in the cone, $E_T^{h^0}$ is the total E_T of neutral hadrons in
 990 the cone, E_T^γ is the total contribution of photons in the cone, ρ is defined as above,
 991 and p_T^ℓ is the lepton p_T . R is set to 0.3 for electrons and 0.4 for muons.

992 Figure 3.4 shows how the size of the pileup correction term depends on lepton
 993 displacement in the standard isolation but not in the modified isolation described here.
 994 We use the modified isolation definition for both electrons and muons while keeping
 995 the original tight working point for electrons and slightly tightening the tight working

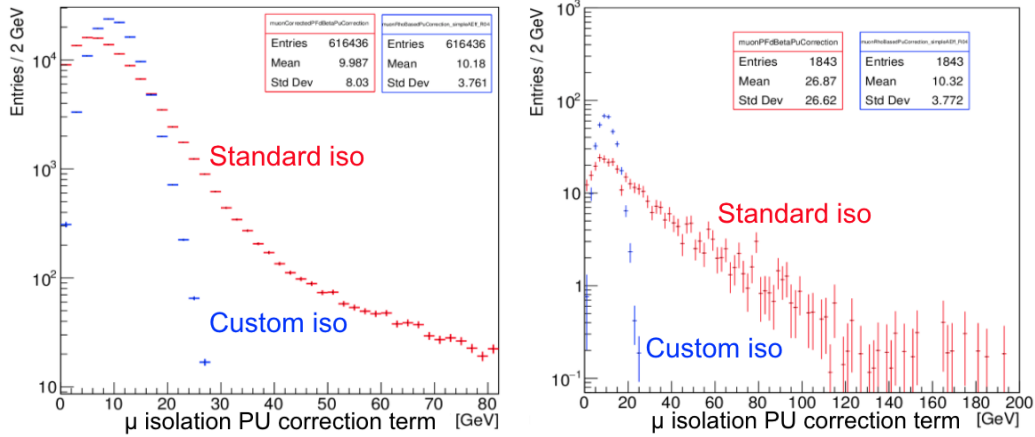


Figure 3.4: Comparison of the the muon isolation pileup correction term in the standard muon isolation and the modified muon isolation in simulated $t\bar{t}$ events that pass the 2018 $e\mu$ preselection. Muon $|d_0|$ is constrained to be less than 100 μm in the plot on the left and between 500 and 1000 μm in the plot on the right.

996 point for muons. In the end, we require that the relative isolation is < 0.10 for muons
 997 and < 0.0588 for electrons in 2016 and $< 0.0287 + 0.506/p_T$ for electrons in 2017 and
 998 2018. As shown in Figs. 3.5 and 3.6, this modified PF isolation rejects substantially
 999 more background when the leptons are displaced but does not significantly alter the
 1000 signal yield. We note, however, that there may still be some minor dependence on the
 1001 primary vertex selection in the PF muon requirement because the PF muon selection
 1002 includes some loose isolation requirements where the charged hadron component is
 1003 constrained to the selected primary vertex.

1004 We also reject electrons and muons in certain regions of the η - ϕ plane where lepton
 1005 d_0 is more likely to be mismeasured. We identify these regions as highly populated
 1006 bins in the electron η - ϕ distribution in a prompt-muon, displaced-electron control
 1007 region in 2017 and 2018 data (see Fig.3.7). No such bins are present in 2016 data.
 1008 The identified regions coincide with regions found by a previous CMS analysis [55] to

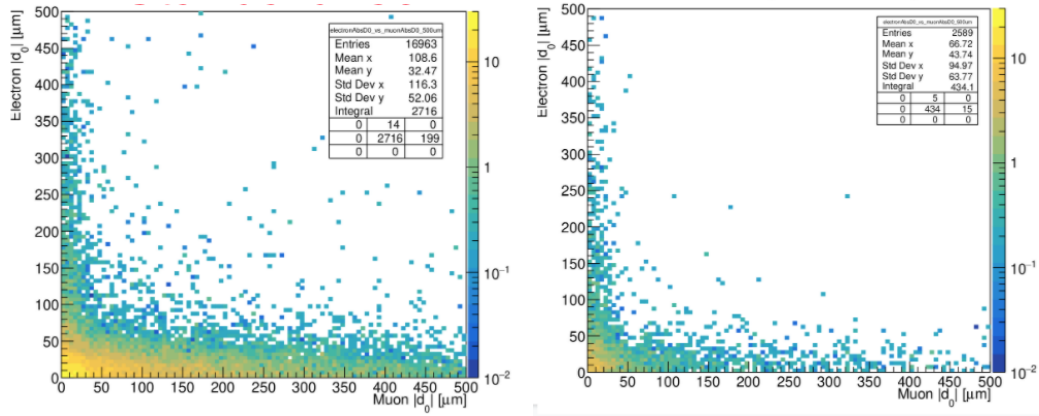


Figure 3.5: The distribution of $t\bar{t}$ simulated events in the plane defined by electron $|d_0|$ and muon $|d_0|$. The standard isolation is applied in the plot on the left, and the modified isolation is applied in the plot on the right, and the events in both plots are required to pass the remaining 2018 $e\mu$ preselection criteria and the additional constraint that the parent of at least one lepton is a heavy-flavor meson.

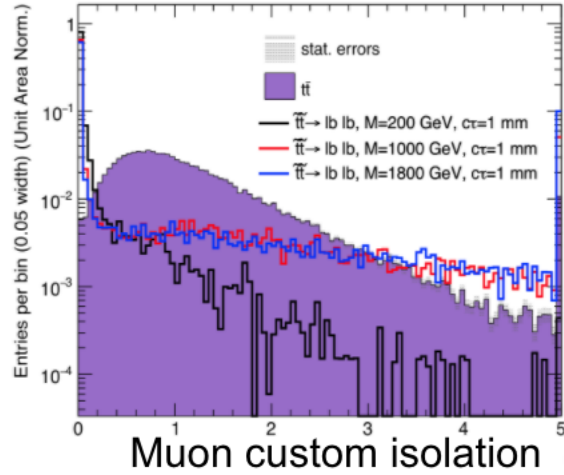


Figure 3.6: The muon modified isolation distribution for simulated $t\bar{t}$ background and $\tilde{t}\tilde{t} \rightarrow l b \bar{l} \bar{b}$ signal events that pass the 2018 $e\mu$ preselection with no isolation criterion applied.

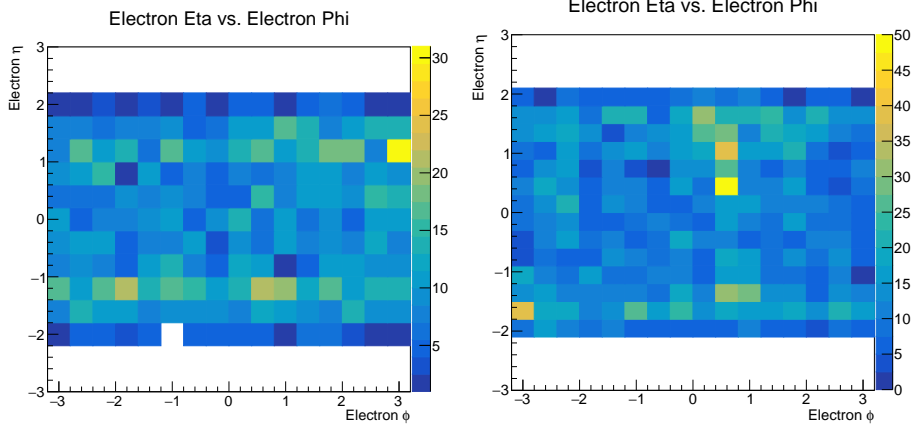


Figure 3.7: The electron $\eta - \phi$ distribution in a prompt-muon, displaced-electron control region in 2017 (left) and 2018 (right) data before vetoing the regions affected by pixel power-supply issues.

1009 be affected by power supply issues in the pixel detector. The $\eta\text{-}\phi$ variation is more
 1010 apparent for displaced electrons than displaced muons, so we use data in a prompt
 1011 muon ($|d_0| < 40 \mu\text{m}$), displaced electron ($100 < |d_0| < 500 \mu\text{m}$) control region to
 1012 define the regions used for both electrons and muons. In 2017, the rejected region is
 1013 $1.0 < \eta < 1.5$ AND $\phi > 2.7$, and in 2018 the rejected region is $0.3 < \eta < 1.2$ AND
 1014 $0.4 < \phi < 0.8$.

1015 In addition to these object-level selections, we also impose a few event-level se-
 1016 lections designed to remove potential backgrounds from cosmic rays, material inter-
 1017 actions, and displaced decays of SM hadrons. To remove cosmic-ray muons in the
 1018 $\mu\mu$ and $e\mu$ channels, we require there be zero pairs of muons with $\cos \alpha < -0.99$,
 1019 where α is the 3D angle between the muons, and that the relative time between the
 1020 leading two muons is inconsistent with the timing of cosmic-ray muons. To do this,
 1021 we look at the muon time measured by the DTs and CSCs, which assume that the

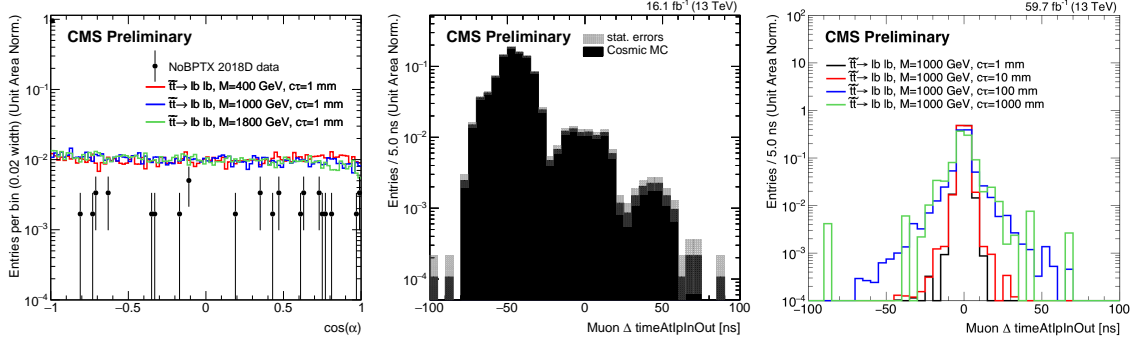


Figure 3.8: The di-muon $\cos(\alpha)$ distribution of 2018 NoBPTX data and simulated $\tilde{t}\tilde{t} \rightarrow \bar{l}b\bar{l}b$ events (left) and the di-muon Δt distribution in simulated cosmic ray muon events in 2016 conditions (center) and $\tilde{t}\tilde{t} \rightarrow \bar{l}b\bar{l}b$ (right) events in 2018 conditions. In each case, all $\mu\mu$ preselection criteria except those relating to cosmic rejection are applied.

1022 muons are traveling outwards from the center of the detector. We then use the muon
 1023 ϕ measurements to determine which muon is above the other and find Δt , the time
 1024 of the lower muon subtracted from the time of the upper muon. We reject events
 1025 with $\Delta t < -20$ if the number of degrees of freedom of the timing measurements for
 1026 both muons is greater than seven. Figure 3.8 shows the $\cos \alpha$ and Δt distributions of
 1027 NoBPTX data and simulated cosmic and $\tilde{t}\tilde{t} \rightarrow \bar{l}b\bar{l}b$ events.

1028 To remove leptons from decays of SM hadrons, we require that the candidate
 1029 leptons not be too close together in the η - ϕ plane. Specifically, we find that requiring
 1030 $\Delta R > 0.2$ significantly reduces the contribution from SM hadrons without noticeably
 1031 affecting the signal acceptance. To remove leptons from material interactions, we
 1032 reject events in which the candidate leptons form a good displaced vertex that overlaps
 1033 with the tracker material. The vertices are reconstructed with the Kalman Vertex
 1034 Fitter, and a “good” vertex is one with $\chi^2/n_{\text{dof}} < 20$. The tracker material map is

1035 obtained from the tracker material budget measurements [71, 72]. See Section 3.5.6
1036 for tests in data that involve inverting the criteria described in this paragraph.

1037 Finally, to ensure that the signal regions of all three channels are orthogonal to
1038 one another, we reject events in the ee ($\mu\mu$) channel with at least one muon (electron)
1039 that passes the $e\mu$ channel preselection and has $|d_0| > 100 \mu\text{m}$.

1040 In contrast to previous displaced leptons analyses [52, 53], we allow for the possi-
1041 bility of more than one lepton of each type in a given channel and set no requirements
1042 on the charge product of the lepton pair. These changes were made at the request of
1043 several theorists, including the authors of Ref. [73].

1044 Figure 3.9 shows the electron and muon $|d_0|$ distributions in simulated signal and
1045 background events that pass the 2018 $e\mu$ preselection, and Fig. 3.10 shows the cumu-
1046 lative number of simulated signal events that pass each 2018 preselection criterion in
1047 all three channels for several top squark lifetime hypotheses.

1048 **3.3.3 Prompt control region**

1049 In order to verify the implementation of our selection and corrections to simula-
1050 tion (see Section 3.4), we define a prompt control region that is dominated by SM
1051 background events. Events in each channel’s prompt control region are selected by
1052 requiring that they pass all of the criteria defined in Section 3.3.2 as well as the
1053 requirement that the candidate leptons have $|d_0| < 50 \mu\text{m}$. We define this region in
1054 each channel in order to check for reasonable agreement between simulated SM events
1055 and data after applying the corrections described in Section 3.4. Some examples are
1056 shown in Figs. 3.11, 3.12, and 3.13, which show the p_T , η , and $|d_0|$ distributions of the
1057 leptons in the $e\mu$, ee , and $\mu\mu$ prompt control regions, respectively, for 2016 data and

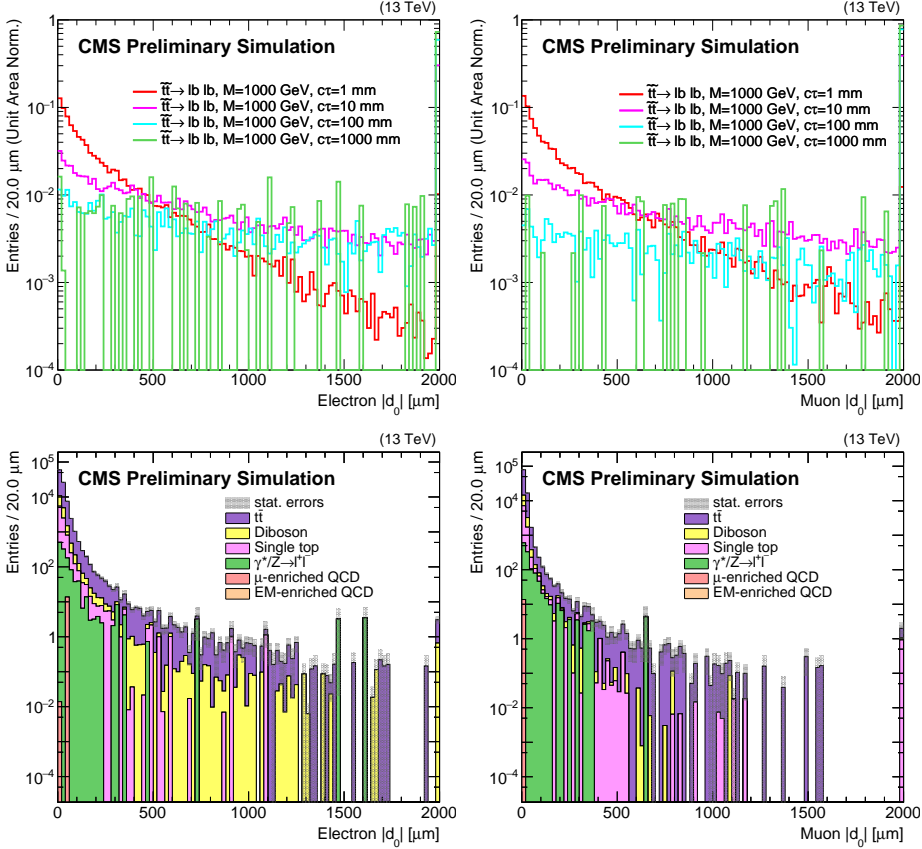


Figure 3.9: The electron (left) and muon (right) $|d_0|$ distributions for 2018 simulation events that pass the $e\mu$ preselection criteria. The upper two plots show $\tilde{t}\bar{t} \rightarrow \bar{l}b\bar{l}b$ simulation for a single \tilde{t} mass and four different proper decay lengths; each histogram is normalized to unity. The lower two plots show the background simulation normalized to the integrated luminosity. In all of the histograms, the last bin includes the overflow. All of the corrections from Section 3.4 are applied.

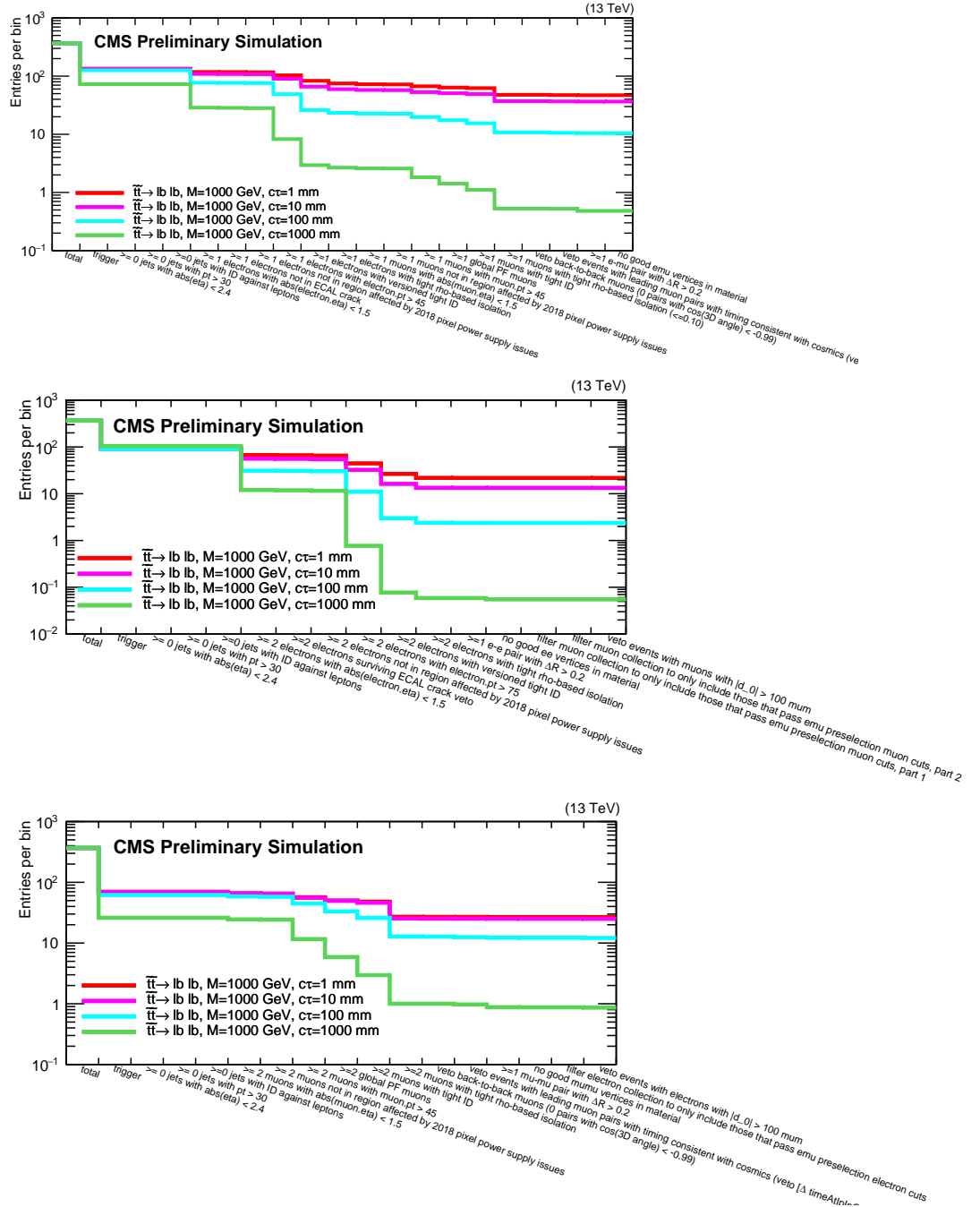


Figure 3.10: The cumulative number of events that pass each criterion in the $e\mu$ (upper), ee (middle), and $\mu\mu$ (lower) preselection, using 2018 signal simulation. Several \tilde{t} proper decay lengths are shown. The jet criteria do not exclude any events and are simply an artifact of the analysis framework.

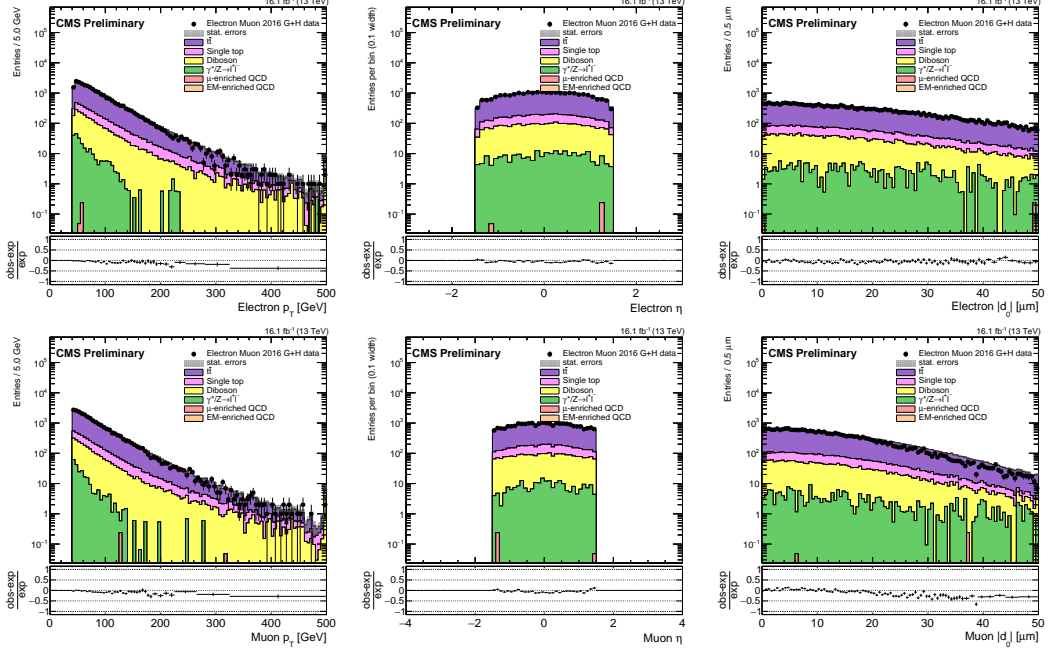


Figure 3.11: The electron (top) and muon (bottom) p_T (left), η (center), and $|d_0|$ (right) distributions in the $e\mu$ prompt control region for 2016 data and simulated background events. The rightmost bin in each plot contains the overflow entries.

background simulation. The data-driven background estimation technique employed in this analysis removes the need for exact agreement between data and simulation, but the absence of any significant discrepancies gives us confidence that we are accounting for the correct sources of prompt SM leptons and that our selection and corrections are functioning as intended.

3.3.4 Inclusive signal region

Finally, we define the region to which new physics may contribute significantly. The inclusive signal region is populated by events that pass all of the criteria defined in Section 3.3.2 as well as the requirement that the candidate leptons each have $100 \mu\text{m} < |d_0| < 10 \text{ cm}$. We do not select leptons with $|d_0| > 10 \text{ cm}$ because the tracking

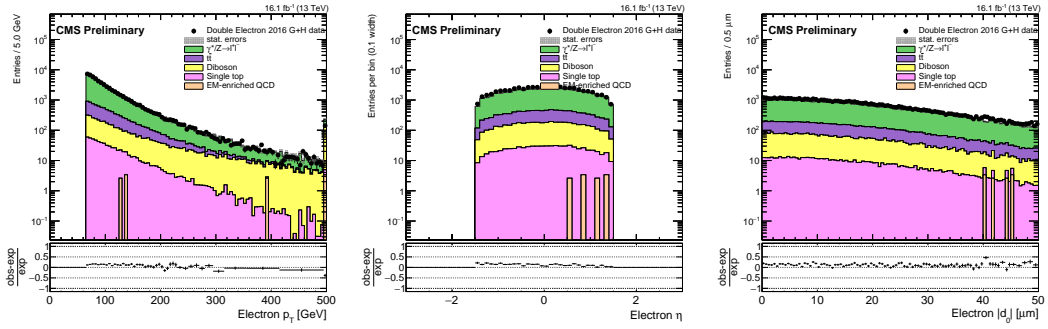


Figure 3.12: The electron p_T (left), η (center), and $|d_0|$ (right) distributions in the ee prompt control region for 2016 data and simulated background events. The rightmost bin in each plot contains the overflow entries.

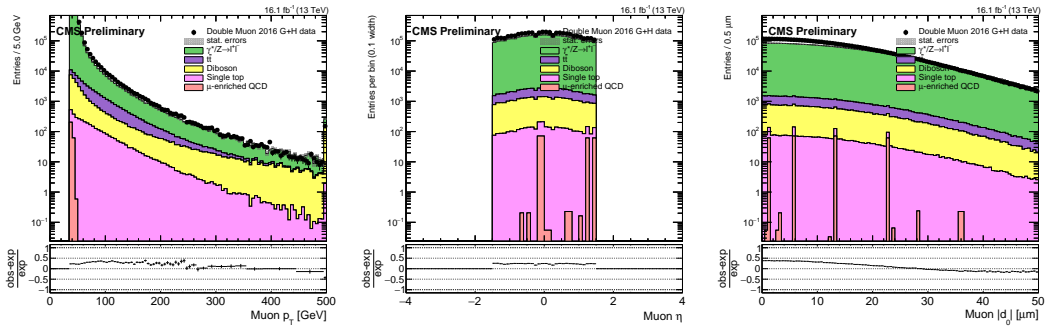


Figure 3.13: The muon p_T (left), η (center), and $|d_0|$ (right) distributions in the $\mu\mu$ prompt control region for 2016 data and simulated background events. The rightmost bin in each plot contains the overflow entries.

Table 3.7: The cumulative efficiency for simulated $\tilde{t}\tilde{t} \rightarrow \bar{l}b\bar{l}b$ signal events to pass the 2018 inclusive signal region selection, for several choices of \tilde{t} mass and $c\tau$. The corrections described in Section 3.4 are applied.

$e\mu$ inclusive signal region			
	200 GeV	1000 GeV	1800 GeV
0.1 cm	2.1%	4.6%	4.6%
1 cm	3.5%	7.9%	8.8%
10 cm	1.0%	2.7%	3.4%
100 cm	0.047%	0.13%	0.16%

ee inclusive signal region			
	200 GeV	1000 GeV	1800 GeV
0.1 cm	0.47%	2.1%	2.1%
1 cm	0.60%	2.8%	3.3%
10 cm	0.11%	0.59%	0.76%
100 cm	0.003%	0.014%	0.022%

$\mu\mu$ inclusive signal region			
	200 GeV	1000 GeV	1800 GeV
0.1 cm	1.4%	2.6%	2.5%
1 cm	3.1%	5.6%	5.9%
10 cm	1.5%	3.2%	3.7%
100 cm	0.11%	0.23%	0.34%

efficiency drops sharply after this point, as shown in Section C. This requirement also ensures that the leptons originate within the pixel volume, which is effectively required by the pixel hit requirement of the tight lepton IDs. Table 3.7 lists the cumulative efficiency for $\tilde{t}\tilde{t} \rightarrow \bar{l}b\bar{l}b$ events to pass the full 2018 inclusive signal region selection for several signal points. To ensure sensitivity to a wide range of new particle masses and lifetimes, we further subdivide the inclusive signal region into bins defined by the $|d_0|$ of each candidate lepton and the p_T of one candidate lepton. The exact binning is described in Section 3.5.2.

1076 **3.4 Corrections to simulation**

1077 We apply several corrections to the simulated background and signal events in
1078 order to account for known differences between simulation and data. Each correction
1079 is described individually in the following sections.

1080 **3.4.1 Pileup**

1081 The simulation is corrected so that its distribution of the number of pileup interac-
1082 tions matches that of 2016, 2017, and 2018 data. Each simulated sample is reweighted,
1083 event-by-event, by scale factors derived by dividing the pileup distribution in data by
1084 the pileup distribution in the given simulated sample.

1085 **3.4.2 Lepton ID**

1086 We apply scale factors provided by the CMS Physics Object Groups to correct for
1087 known differences in the lepton reconstruction and tight ID performance between data
1088 and simulation. Although our lepton ID differs from the standard tight ID in that
1089 we do not set requirements on d_0 or d_z , the standard scale factors are still sufficient
1090 because they are derived from leptons from Z boson decays that are representative
1091 of leptons in the bulk of the $|d_0|$ distribution, and we apply additional systematic
1092 uncertainties to account for possible differences at larger $|d_0|$ (see Section 3.6).

1093 **3.4.3 Lepton d_0 resolution**

1094 As shown in Fig. 3.14, the agreement between data and simulation in the 2017 and
1095 2018 electron and muon $|d_0|$ distributions was initially poor. We found that the aver-
1096 age muon and electron d_0 fluctuated periodically with respect to ϕ in 2017 and 2018
1097 data but not in background simulation, as can be seen in Fig. 3.15. This periodic

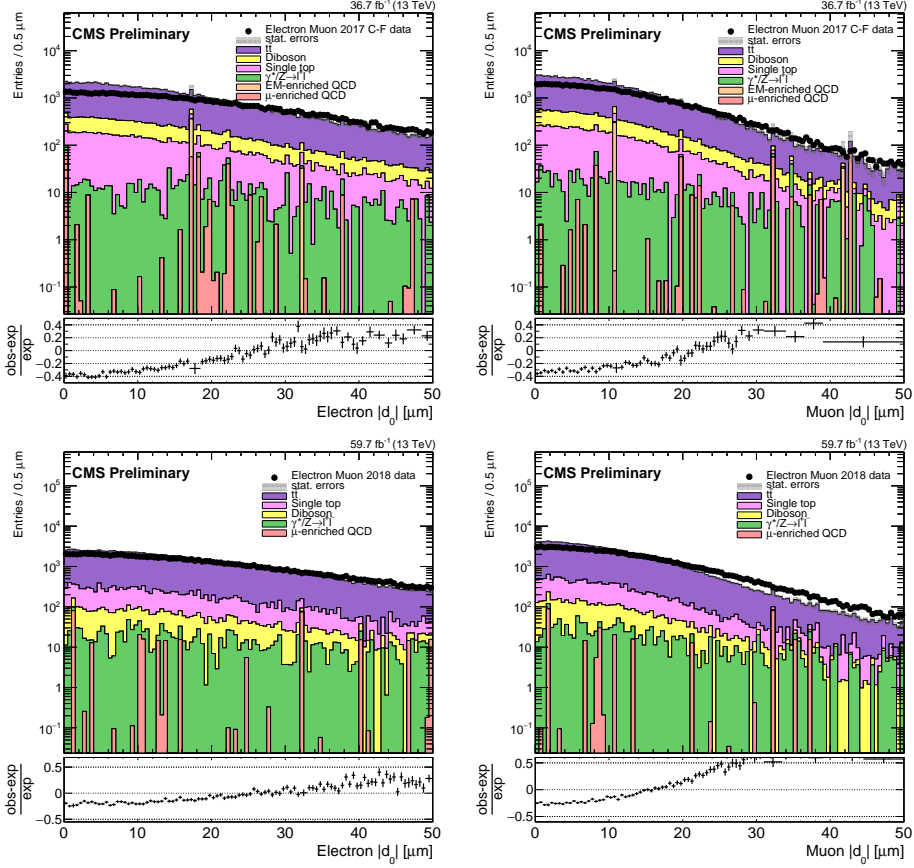


Figure 3.14: The uncorrected lepton $|d_0|$ distributions in the $e\mu$ prompt control region, for electrons (left) and muons (right), for 2017 data and simulation (upper), and 2018 data and simulation (lower). The rightmost bin in each plot contains the overflow entries.

fluctuation in data but not in simulation indicates that an overly optimistic simulated tracker alignment is responsible for the unrealistically narrow d_0 distribution in simulation.

To account for the overly optimistic alignment in simulation, we smear the electron and muon d_0 in 2017 and 2018 simulation in each channel's prompt control region to better model the d_0 distribution in data. To do this, we first fit the central regions of the background simulation and data d_0 distributions with Gaussian functions in each

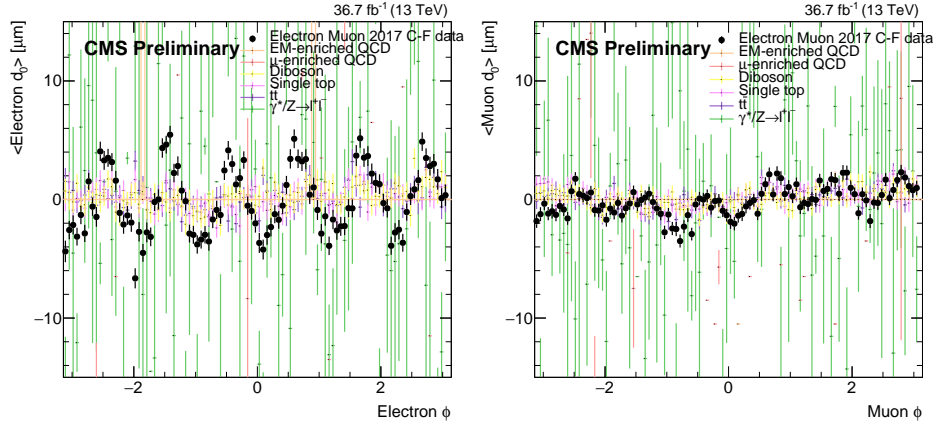


Figure 3.15: The average lepton $|d_0|$ as a function of ϕ in the $e\mu$ prompt control region, for electrons (left) and muons (right), for 2017 data and simulation.

1105 channel's prompt control region and then compare the widths of the Gaussian fits.
 1106 The fitted distributions are shown in Figs. 3.16 and 3.17 for the $e\mu$ channel. Assuming
 1107 that the width of each Gaussian fit is mostly determined by the d_0 resolution, we define
 1108 $\sigma_{data}^2 = \sigma_{bkg}^2 + \sigma_{align}^2$, where σ_{data} is the data Gaussian width, σ_{bkg} is the uncorrected
 1109 background simulation Gaussian width, and σ_{align} is the additional component that
 1110 is needed to make up the difference in d_0 resolution between background simulation
 1111 and data. We find σ_{data} and σ_{bkg} from the fits and compute σ_{align} . The fit results are
 1112 similar in the $e\mu$ channel shown here and in the same-flavor channels. We average
 1113 the σ_{align} derived in the ee channel and the $e\mu$ channel for electrons, and in the $\mu\mu$
 1114 channel and the $e\mu$ channel for muons. The average σ_{align} is shown in Table 3.8. We
 1115 then smear the simulation d_0 values with values drawn from a Gaussian distribution
 1116 centered on zero and with a width of the average σ_{align} . The smearing is applied to
 1117 both background and signal simulation. The corrected $|d_0|$ distributions are shown
 1118 in Fig. 3.18.

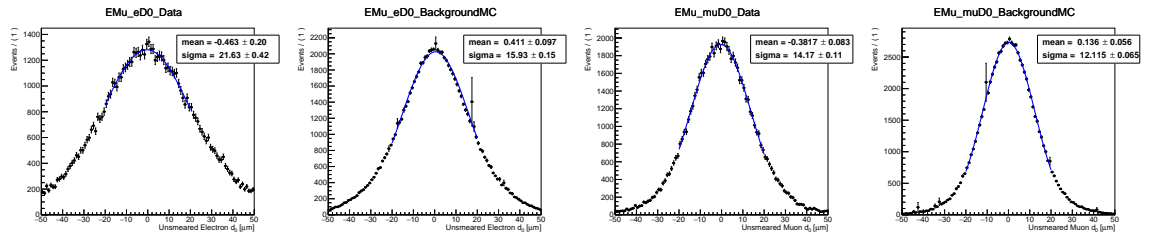


Figure 3.16: The lepton d_0 distributions with Gaussian fits in the 2017 $e\mu$ prompt control region for (working from left to right) electrons in data, electrons in background simulation, muons in data, and muons in background simulation.

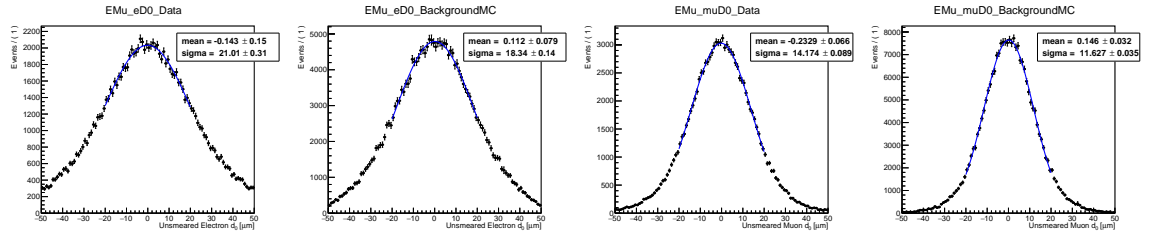


Figure 3.17: The lepton d_0 distributions with Gaussian fits in the 2018 $e\mu$ prompt control region for (working from left to right) electrons in data, electrons in background simulation, muons in data, and muons in background simulation.

Table 3.8: The average σ_{align} for electrons and muons, for the 2017 and 2018 analyses.

	2017	2018
Electrons	$14.75 \pm 0.36 \mu\text{m}$	$9.18 \pm 0.41 \mu\text{m}$
Muons	$7.57 \pm 0.12 \mu\text{m}$	$8.11 \pm 0.08 \mu\text{m}$

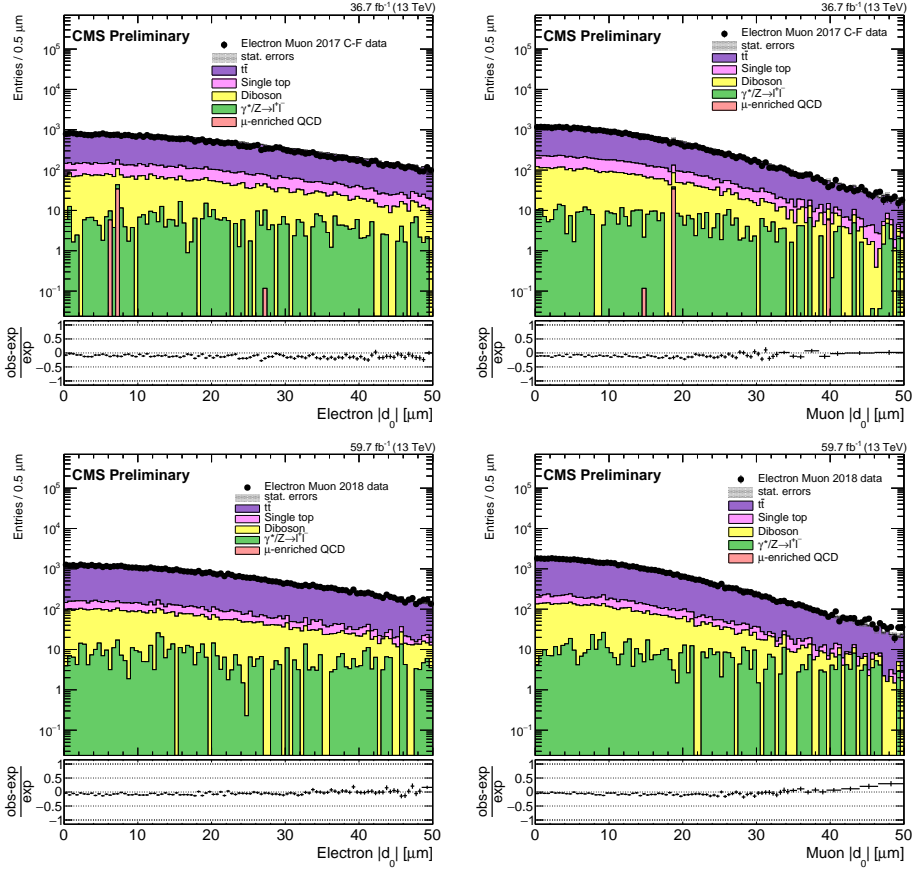


Figure 3.18: The corrected lepton $|d_0|$ distributions in the $e\mu$ prompt control region, for electrons (left) and muons (right), for 2017 data and simulation (upper), and 2018 data and simulation (lower). The rightmost bin in each plot contains the overflow entries.

1119 This d_0 smearing has a minimal effect on the final result because the width of the
1120 Gaussian distribution from which the smearing values are drawn is small relative to
1121 the size of the signal region bins, but understanding the source of the poor agreement
1122 between data and simulation was important to validate our understanding of the SM
1123 background.

1124 3.4.4 Trigger efficiency

1125 We also apply scale factors to the simulated background and signal events to cor-
1126 rect for differences in trigger efficiency between data and simulation. To measure the
1127 trigger efficiency, we first require that events pass an OR of several unprescaled p_T^{miss}
1128 triggers (see Table 3.9) and the preselection criteria with the lepton p_T requirement
1129 excluded. The p_T^{miss} triggers provide a sample of dilepton events that is unbiased
1130 with respect to the main triggers used in the analysis, and excluding the lepton p_T
1131 requirement allows us to study the trigger efficiency as a function of lepton p_T . In
1132 the $e\mu$ channel, the electron (muon) p_T is required to be greater than 50 GeV when
1133 plotting against the muon (electron) p_T to disentangle the effect from the other leg of
1134 the muon-photon trigger. Data events are taken from the MET primary dataset (which
1135 contains events that pass p_T^{miss} triggers) and simulated background events are taken
1136 from $t\bar{t}$ simulation for the $e\mu$ channel and Drell-Yan simulation for the same-flavor
1137 channels.

1138 To calculate the efficiency, we divide the lepton p_T distribution in events that
1139 pass the standard analysis triggers in addition to the OR of the p_T^{miss} triggers and
1140 the preselection by the lepton p_T distribution in events that pass the OR of the
1141 p_T^{miss} triggers and the preselection. We then compute the scale factor as the ratio of

Table 3.9: The unprescaled p_T^{miss} triggers used to create an orthogonal data sample for the trigger efficiency calculation.

2016
HLT_MET200
HLT_MonoCentralPFJet80_PFMETNoMu110_PFMHTNoMu110_IDTight
HLT_PFMET120_PFMHT120_IDTight
HLT_PFMET170_HBHECleaned
HLT_PFMET300
HLT_PFMETNoMu120_PFMHTNoMu120_IDTight
2017
HLT_CaloMET350_HBHECleaned
HLT_MonoCentralPFJet80_PFMETNoMu120_PFMHTNoMu120_IDTight
HLT_PFMET120_PFMHT120_IDTight
HLT_PFMET250_HBHECleaned
HLT_PFMETNoMu120_PFMHTNoMu120_IDTight
2018
HLT_CaloMET350_HBHECleaned
HLT_MonoCentralPFJet80_PFMETNoMu120_PFMHTNoMu120_IDTight
HLT_PFMET120_PFMHT120_IDTight
HLT_PFMET200_HBHE_BeamHaloCleaned
HLT_PFMET250_HBHECleaned
HLT_PFMETNoMu120_PFMHTNoMu120_IDTight

Table 3.10: The trigger efficiency scale factors in each channel and year.

	2016	2017	2018
$e\mu$ channel, electrons	0.974 ± 0.016	0.961 ± 0.013	0.965 ± 0.012
$e\mu$ channel, muons	0.975 ± 0.016	0.972 ± 0.014	0.967 ± 0.012
ee channel	1.000 ± 0.099	1.000 ± 0.131	1.000 ± 0.185
$\mu\mu$ channel	0.956 ± 0.012	0.930 ± 0.010	0.935 ± 0.011

¹¹⁴² the efficiency in data to the efficiency in simulation in the plateau of the efficiency
¹¹⁴³ distribution. The $e\mu$ channel efficiency distributions are shown in Fig. 3.19, and the
¹¹⁴⁴ resulting scale factors for all channels are listed in Table 3.10.

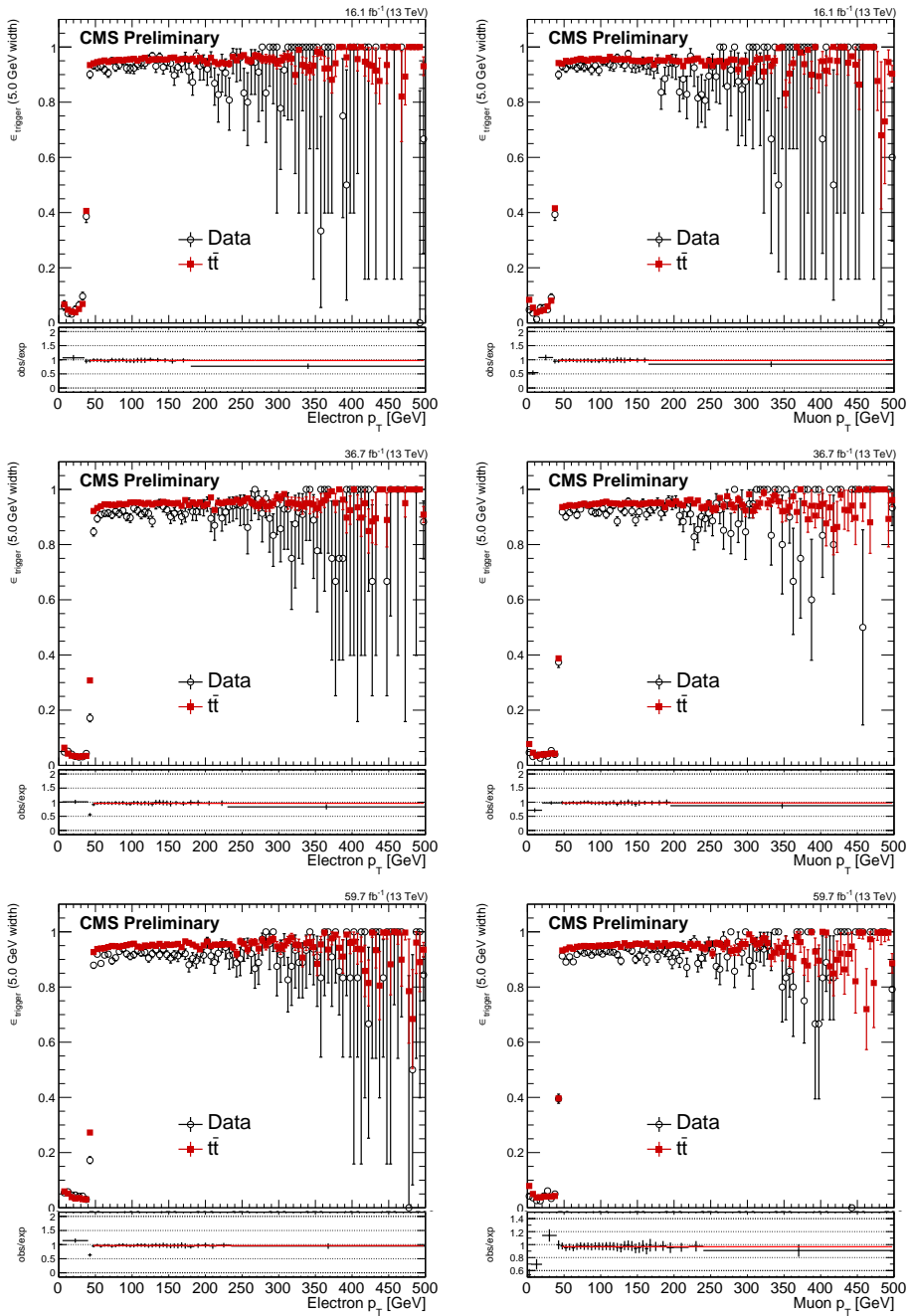


Figure 3.19: Trigger efficiency as a function of leading electron (left) or leading muon (right) p_T in the $e\mu$ channel in 2016 (top), 2017 (middle), and 2018 (bottom) in data and simulated background $t\bar{t}$ events.

1145 **3.5 Background estimation**

1146 **3.5.1 Background sources**

1147 The vast majority of leptons from SM processes are prompt. There are, however,
1148 a few notable processes that produce leptons with large $|d_0|$ values that may pass our
1149 selection: (1) leptons from prompt decays whose $|d_0|$ is poorly measured ("mismeas-
1150 urements"), (2) leptons from decays of tau leptons ("taus"), and (3) leptons from
1151 decays of B or D mesons ("heavy flavor"). Note that the leptons from these processes
1152 generally do not share a common displaced vertex. We perform several cross checks
1153 to ensure that processes in which leptons share a common displaced vertex do not
1154 contribute significantly in the signal regions (SRs). Section 3.5.6 presents several
1155 additional studies that confirm that the SR contribution of leptons from material
1156 interactions, cosmic rays, and SM hadrons are either negligible or already accounted
1157 for by the background estimation procedure.

1158 The $|d_0|$ distributions of leptons from the three main background sources vary
1159 according to lepton flavor and parent particle. Tau leptons have a lifetime of 87 μm ,
1160 B mesons have a lifetime around 500 μm , and D mesons have a lifetime of around
1161 100 μm , so leptons from taus will generally have smaller $|d_0|$ values than leptons from
1162 heavy flavor. Furthermore, mismeasurements are more common for electrons than for
1163 muons due to the superior muon d_0 resolution. Figure 3.20, which shows the relative
1164 contribution of each source of leptons as a function of $|d_0|$ in simulated $t\bar{t}$ events that
1165 pass the $e\mu$ channel preselection, shows how mismeasurements dominate at all $|d_0|$
1166 values for electrons while taus and heavy-flavor contribute meaningfully for muons
1167 with $|d_0| \gtrsim 100 \mu\text{m}$.

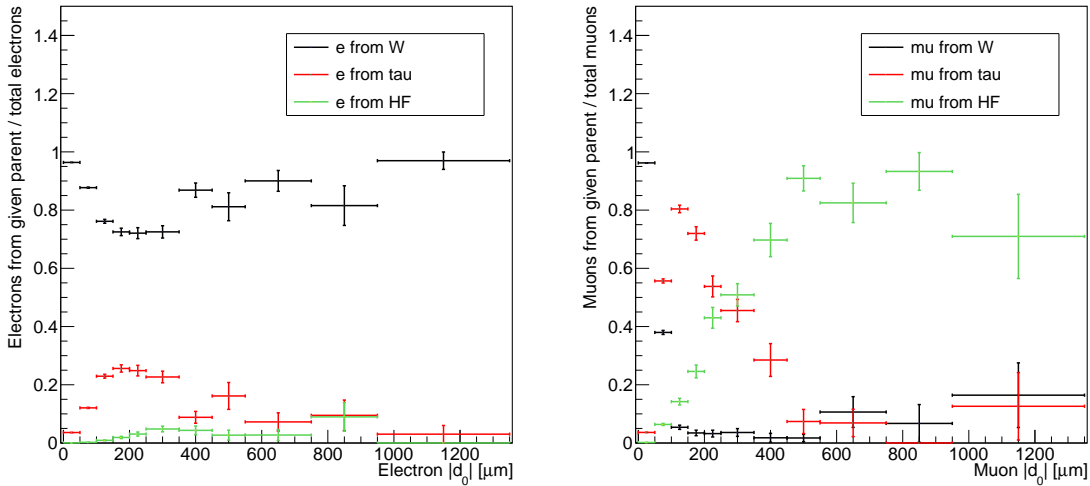


Figure 3.20: The fraction of electrons (left) and muons (right) from different parents as a function of lepton $|d_0|$, for simulated $t\bar{t}$ events that pass the 2018 $e\mu$ channel preselection. In $t\bar{t}$ events, the vast majority of leptons whose parent is a W boson are produced in a prompt decay.

1168 In the $\mu\mu$ channel, it is worth examining which long-lived SM parents will con-
 1169 tribute to $|d_0|$ - $|d_0|$ correlation. The correlation specifically comes from DY-type pro-
 1170 cesses in which the parentage is correlated between muons. Figure 3.21, which shows
 1171 the fraction of muons from different background sources in DY simulation, indicates
 1172 that tau lepton decays are the main source of muons that may be correlated in this
 1173 way, and that the heavy-flavor contribution is negligible. This is reasonable because
 1174 while tau leptons and heavy-flavor mesons both produce displaced muons, the iso-
 1175 lation criteria rejects the vast majority of muons from heavy-flavor mesons. Muons
 1176 from tau leptons contribute significantly from about 100 to 500 μm , so we expect the
 1177 most significant $|d_0|$ - $|d_0|$ correlation to appear in this range and peak around 200 μm .

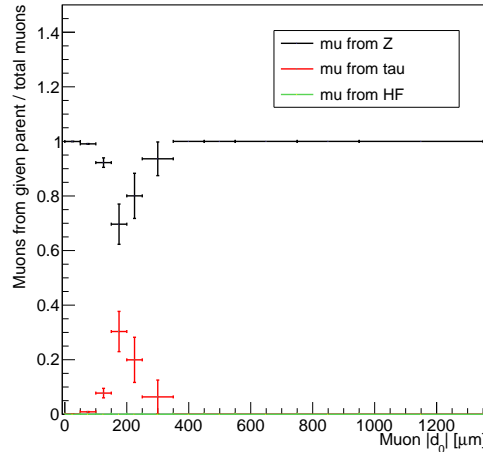


Figure 3.21: The fraction of muons from different parents as a function of muon $|d_0|$, for simulated DY events that pass the 2018 $\mu\mu$ channel preselection and the additional constraint that the leading and subleading muon both come from the same type of parent particle.

₁₁₇₈ Furthermore, the correlation will be most pronounced in the regions where the $|d_0|$
₁₁₇₉ measurements are the best.

₁₁₈₀ 3.5.2 Data-driven ABCD method

₁₁₈₁ We estimate the SR background yields with a data-driven method in which the lep-
₁₁₈₂ ton $|d_0|$ distributions serve as composite models of all background processes. Specif-
₁₁₈₃ ically, we employ an ABCD method using the $|d_0|$ of two leptons. We label the two
₁₁₈₄ $|d_0|$ values in each channel as $|d_0^a|$ and $|d_0^b|$, which correspond to the leading e and
₁₁₈₅ leading μ in the $e\mu$ channel, the leading and subleading e in the ee channel, and the
₁₁₈₆ leading and subleading μ in the $\mu\mu$ channel. As a first step, we categorize the events
₁₁₈₇ that pass the preselection criteria into four regions (A, B, C, and D) of the $|d_0^a|$ - $|d_0^b|$
₁₁₈₈ plane, as shown in Fig. 3.22.

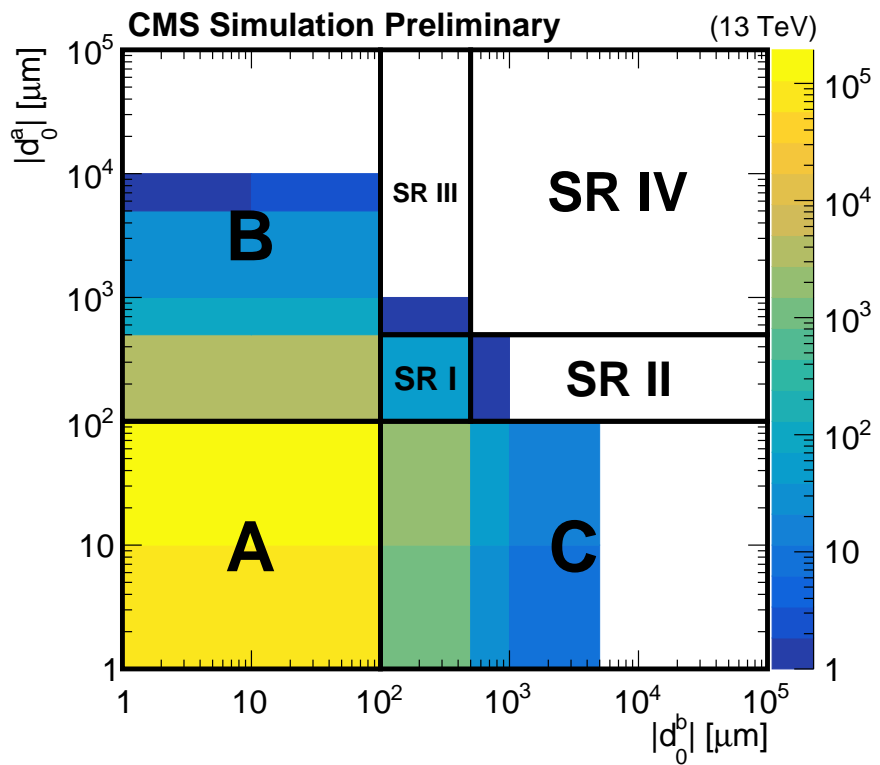


Figure 3.22: A diagram of the ABCD method overlaid on simulated background events passing the 2018 $e\mu$ preselection. A, B, and C are control regions, and D corresponds to the inclusive SR, which includes SRs I, II, III, and IV. Underflow events are included in the bins along the left and bottom edges. When performing the background estimate, regions B and C are further subdivided to coincide with the SR for which the estimate is being performed.

1189 We then use the number of events in regions A, B, and C to estimate the expected
1190 background in each SR. The basic estimation procedure depends on the assumption
1191 that $|d_0^a|$ and $|d_0^b|$ are uncorrelated. If this assumption holds, then $N_B/N_A = N_D/N_C$
1192 and the number of background events in D is equal to $N_B \times N_C/N_A$, where N_X is
1193 the number of background events in the given region. We find that $|d_0^a|$ and $|d_0^b|$ are
1194 indeed uncorrelated over much of the $|d_0|$ - $|d_0|$ plane, but the correlation discussed in
1195 Section 3.5.1 renders the basic ABCD method insufficient to estimate the background
1196 in SR I. After quantifying the degree of correlation in Section 3.5.3, we define a
1197 procedure to correct the basic ABCD estimate in Section 3.5.4.

1198 In order to maximize sensitivity to a wide range of new particle lifetimes, we
1199 further subdivide region D into the following four SRs:

- 1200 • SR I: $100 \leq |d_0^a| < 500 \mu\text{m}$, $100 < |d_0^b| < 500 \mu\text{m}$
- 1201 • SR II: $100 \leq |d_0^a| < 500 \mu\text{m}$, $500 \mu\text{m} < |d_0^b| < 10 \text{ cm}$
- 1202 • SR III: $500 \mu\text{m} \leq |d_0^a| < 10 \text{ cm}$, $100 < |d_0^b| < 500 \mu\text{m}$
- 1203 • SR IV: $500 \mu\text{m} \leq |d_0^a| < 10 \text{ cm}$, $500 \mu\text{m} < |d_0^b| < 10 \text{ cm}$

1204 The exact boundaries between the four SRs are motivated by the expected contribu-
1205 tions of the different background sources, as explained in 3.5.1. This approach also
1206 necessitates that the definitions of regions B and C vary in accordance with the SR for
1207 which a given estimate is performed (e.g. only the events in the $100 \leq |d_0^a| < 500 \mu\text{m}$
1208 range of region B are considered when estimating the yields of SR I and II). Finally,
1209 we subdivide SR I into two bins using one lepton's p_T to further increase sensitivity to
1210 high-mass, low-lifetime new physics. Table 3.11 lists the p_T boundary in each channel
1211 and year.

Table 3.11: The p_T boundaries between the low- and high- p_T bins of SR I in each channel.

	p_T boundary [GeV]
2016 $e\mu$	leading μ $p_T = 90$
2017+2018 $e\mu$	leading μ $p_T = 140$
2016 ee	leading e $p_T = 300$
2017+2018 ee	leading e $p_T = 400$
2016 $\mu\mu$	leading μ $p_T = 100$
2017+2018 $\mu\mu$	leading μ $p_T = 100$

When performing the background estimate and closure tests, we treat the 2016 data and simulation separately from the 2017–2018 data and simulation to avoid any correlations between $|d_0^a|$ and $|d_0^b|$ that may arise from the differences between the original and Phase-1 pixel detectors employed by CMS in 2016 and 2017–2018, respectively (see Section 2.2.2).

3.5.3 Closure tests in control regions

We perform several closure tests of the background estimation procedure in data and simulation to test the method and quantify the degree of $|d_0^a|-|d_0^b|$ correlation from the processes discussed in 3.5.1. Two series of tests are performed, the first in the 100–500 μm subregions of regions B and C and the second in the 500 μm –10 cm subregions of regions B and C.

100–500 μm tests

We perform closure tests in subregions of regions B and C where one lepton is more prompt (20–100 μm) and the other is more displaced (100–500 μm). In these closure tests, we estimate the background yield using the simple ABCD method and

1227 then use the ratio of the actual number of events to the estimated number of events as
1228 the measure of nonclosure (and therefore $|d_0^a|$ - $|d_0^b|$ correlation). With this approach, a
1229 ratio of 1 corresponds to closure and no $|d_0^a|$ - $|d_0^b|$ correlation while ratios greater than
1230 1 correspond to nonclosure and positive $|d_0^a|$ - $|d_0^b|$ correlation. Using the procedure
1231 outlined in Section 3.5.4, we estimate the corresponding degree of nonclosure in SR I
1232 by fitting the resulting ratios and extrapolating from the closure test regions to SR I.
1233 We perform identical procedures in regions B and C and then average the resulting
1234 extrapolated ratios.

1235 Table 3.12 shows the average extrapolated ratios for three rounds of closure tests:
1236 one in background simulation with the $Z \rightarrow \tau\tau \rightarrow ll$ events removed, one in the full
1237 background simulation, and one in data. The average extrapolated ratios are always
1238 compatible with one in background simulation without $Z \rightarrow \tau\tau \rightarrow ll$ events, but they
1239 generally increase when the $Z \rightarrow \tau\tau \rightarrow ll$ events are included. Furthermore, the average
1240 extrapolated ratios from the full background simulation generally describe the average
1241 extrapolated ratios in data. From these results, we conclude that within our statistical
1242 uncertainties, $Z \rightarrow \tau\tau \rightarrow ll$ events are the only meaningful source of correlation and that
1243 the degree of correlation observed in data is modeled reasonably well in simulation.
1244 We also observe that the variation in the degree of correlation across channels matches
1245 our expectations: correlation increases with the number of muons in the final state
1246 and is greater in 2017–2018 than 2016 because of the improved d_0 resolution made
1247 possible by the Phase-1 tracker upgrade (described in Section 2.2.2).

1248 **500 μm –10 cm tests**

1249 We next perform closure tests in subregions of regions B and C where one lepton
1250 is more prompt ($20\text{--}100\,\mu\text{m}$) and the other is more displaced ($500\,\mu\text{m}$ –10 cm). We

Table 3.12: Closure test results in background simulation (with and without $Z \rightarrow \tau\tau \rightarrow ll$ events) and in data, in the 100–500 μm region. The average extrapolated ratios and their statistical uncertainties are given. The A, B, C, and D regions are defined as follows: A is 20–30 μm in prompt lepton $|d_0|$ and 20–100 μm in displaced lepton $|d_0|$, B is 20–30 μm in prompt lepton $|d_0|$ and 100–500 μm in displaced lepton $|d_0|$, C is always 20–100 μm in displaced lepton $|d_0|$, D (the test region) is always 100–500 μm in displaced lepton $|d_0|$, and we perform repeated tests while simultaneously varying the C and D prompt lepton $|d_0|$ s within the 30–100 μm range.

	Bkg. simulation without $Z \rightarrow \tau\tau \rightarrow ll$	Full bkg. simulation	Data
2016 $e\mu$	0.9 ± 0.3	1.6 ± 0.6	0.9 ± 1.3
2017+2018 $e\mu$	1.1 ± 0.4	1.6 ± 0.7	3.1 ± 1.0
2016 ee	0.8 ± 0.5	0.8 ± 0.5	0.6 ± 0.6
2017+2018 ee	0.8 ± 1.0	1.6 ± 0.9	1.5 ± 0.4
2016 $\mu\mu$	1.1 ± 0.8	2.0 ± 0.8	2.5 ± 1.0
2017+2018 $\mu\mu$	2.6 ± 2.8	7.8 ± 3.7	4.2 ± 1.8
Average	1.2 ± 0.5	2.6 ± 0.7	2.1 ± 0.5

again use the ratio of the actual number of events to the estimated number of events as the measure of nonclosure, but in these tests we expect the ratio to be consistent with one because $Z \rightarrow \tau\tau \rightarrow ll$ events do not contribute meaningfully beyond 500 μm . Table 3.13 shows that this is indeed the case for background simulation (with and without $Z \rightarrow \tau\tau \rightarrow ll$ events) and for data. These results imply that $|d_0^a|$ and $|d_0^b|$ are uncorrelated beyond 500 μm , which means that a simple ABCD procedure will be adequate for estimating the background yields in SRs II, III, and IV.

3.5.4 ABCD correction and systematic uncertainty

The closure tests of Section 3.5.3 show that $|d_0^a|$ and $|d_0^b|$ are frequently positively correlated in the 100–500 μm region but are uncorrelated otherwise. To account for this correlation as well as other possible unforeseen sources of nonclosure, we define

Table 3.13: Closure test results in data and background simulation (with and without $Z \rightarrow \tau\tau \rightarrow ll$ events), in the $500 \mu\text{m}$ – 10 cm region. The ratios of the actual yield to the estimated yield and their statistical uncertainties are given. The A, B, C, and D regions are defined as follows: A is 20 – $30 \mu\text{m}$ in prompt lepton $|d_0|$ and 20 – $100 \mu\text{m}$ in displaced lepton $|d_0|$, B is 20 – $30 \mu\text{m}$ in prompt lepton $|d_0|$ and $500 \mu\text{m}$ – 10 cm in displaced lepton $|d_0|$, C is 30 – $100 \mu\text{m}$ in prompt lepton $|d_0|$ and 20 – $100 \mu\text{m}$ in displaced lepton $|d_0|$, and D (the test region) is 30 – $100 \mu\text{m}$ in prompt lepton $|d_0|$ and $500 \mu\text{m}$ – 10 cm in displaced lepton $|d_0|$.

Region B			
	Bkg. simulation without $Z \rightarrow \tau\tau \rightarrow ll$	Bkg. simulation	Data
2016 $e\mu$	$1.1^{+0.3}_{-0.3}$	$1.1^{+0.3}_{-0.3}$	$0.4^{+1.0}_{-0.4}$
2017+2018 $e\mu$	$0.9^{+0.3}_{-0.2}$	$0.9^{+0.3}_{-0.2}$	$0.7^{+0.3}_{-0.3}$
2016 ee	$0.4^{+0.6}_{-0.3}$	$0.4^{+0.6}_{-0.3}$	$1.4^{+1.6}_{-0.9}$
2017+2018 ee	$0.5^{+0.8}_{-0.4}$	$0.3^{+0.4}_{-0.2}$	$1.0^{+0.3}_{-0.3}$
2016 $\mu\mu$	$0.7^{+0.3}_{-0.3}$	$0.7^{+0.3}_{-0.3}$	$0.8^{+0.3}_{-0.3}$
2017+2018 $\mu\mu$	$0.8^{+1.8}_{-0.7}$	$0.4^{+1.0}_{-0.4}$	$1.8^{+0.6}_{-0.7}$

Region C			
	Bkg. simulation without $Z \rightarrow \tau\tau \rightarrow ll$	Bkg. simulation	Data
2016 $e\mu$	$0.8^{+0.4}_{-0.3}$	$0.8^{+0.4}_{-0.3}$	1.0 (0 vs 0)
2017+2018 $e\mu$	$0.8^{+0.3}_{-0.2}$	$0.8^{+0.3}_{-0.2}$	$0.7^{+1.3}_{-0.7}$
2016 ee	$4.0^{+5.8}_{-3.1}$	$4.0^{+5.8}_{-3.1}$	$0.7^{+1.0}_{-0.6}$
2017+2018 ee	$3.5^{+2.6}_{-1.8}$	$2.1^{+2.6}_{-1.5}$	$1.0^{+0.3}_{-0.3}$
2016 $\mu\mu$	$1.2^{+0.5}_{-0.4}$	$1.3^{+0.6}_{-0.4}$	$0.6^{+0.4}_{-0.3}$
2017+2018 $\mu\mu$	$0.4^{+0.4}_{-0.3}$	$0.5^{+0.5}_{-0.3}$	$0.5^{+0.3}_{-0.2}$

1262 a procedure to correct the simple ABCD estimate in SR I and assign a systematic
1263 uncertainty to the simple ABCD estimate in all SRs.

1264 **100–500 μm correction and systematic uncertainty**

1265 Figures 3.23, 3.24, and 3.25 show the results of the data closure tests in the $e\mu$
1266 ee , and $\mu\mu$ channels, respectively, in the one-prompt (20–100 μm)/one-displaced (100–
1267 500 μm) sidebands. These plots show the ratio of the actual to the estimated number
1268 of events as a function of the prompt lepton $|d_0|$. In all of these plots, the binning of
1269 the prompt lepton axis is initially 10 μm wide. Starting from most-displaced bin, we
1270 test to see if any bin has fewer than 5 events, and if so, we combine it with whichever
1271 neighboring bin has fewer events, repeating until all bins have at least 5 events.

1272 In each of the two sidebands, we then fit the resulting ratios with a straight
1273 line, where the slope and y-intercept are allowed to vary, and extrapolate the fit to
1274 200 μm , which is where we expect the largest contribution from tau lepton decays (see
1275 Section 3.5.1). 200 μm also happens to be approximately the center-of-mass of the
1276 100–500 μm bin in background simulation. We average the two extrapolated ratios
1277 and derive a correction and systematic uncertainty from this average extrapolated
1278 ratio.

1279 If the average extrapolated ratio is > 1.0 , we take the central value as a multi-
1280 plicative correction to the background estimate and the uncertainty in the average as
1281 a systematic uncertainty in the background estimate. In this case, we also vary the
1282 200 μm extrapolation point by $\pm 50 \mu\text{m}$ (the approximate width of the peak in the tau
1283 lepton contribution as a function of $|d_0|$). We apply the difference from this varia-
1284 tion in extrapolation point as an additional systematic uncertainty in the background

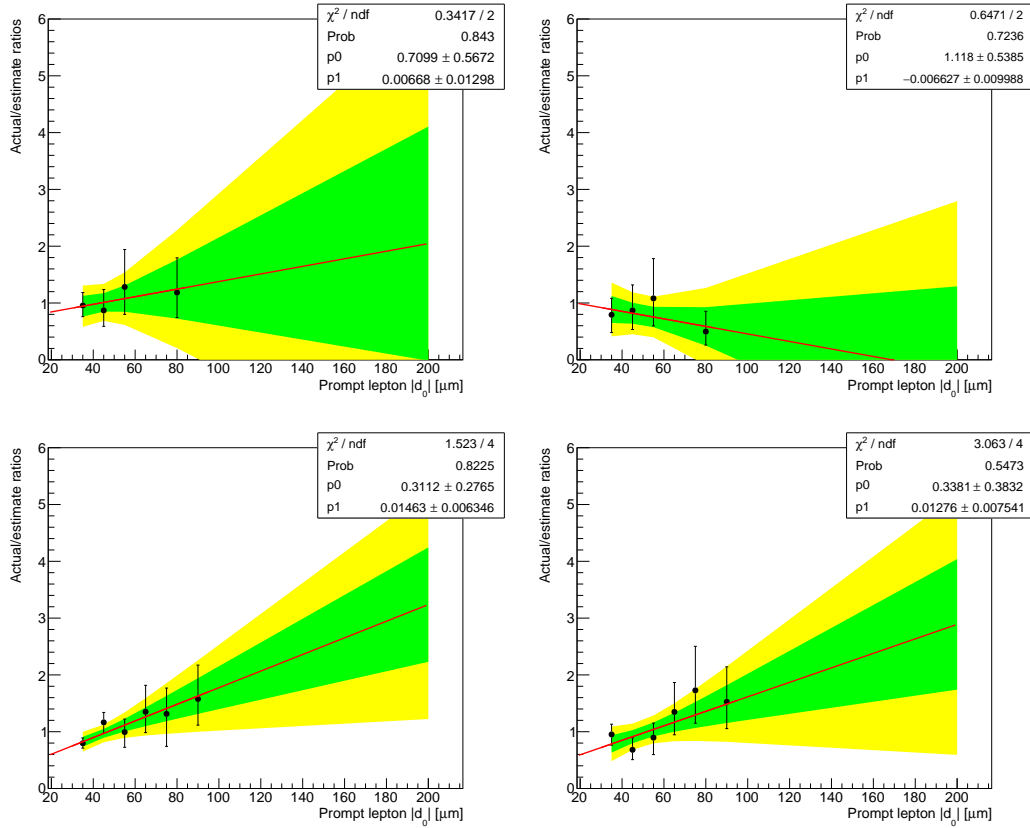


Figure 3.23: Background estimation closure tests in data, in 100–500 μm subregions of regions B (left) and C (right) in the $e\mu$ channel. Each plot shows the ratio of the actual to the estimated number of events as a function of the prompt lepton $|d_0|$ in 2016 (top) and 2017–18 (bottom). A linear fit is shown in black along with the 68 % and 95 % confidence intervals of the extrapolated fit value.

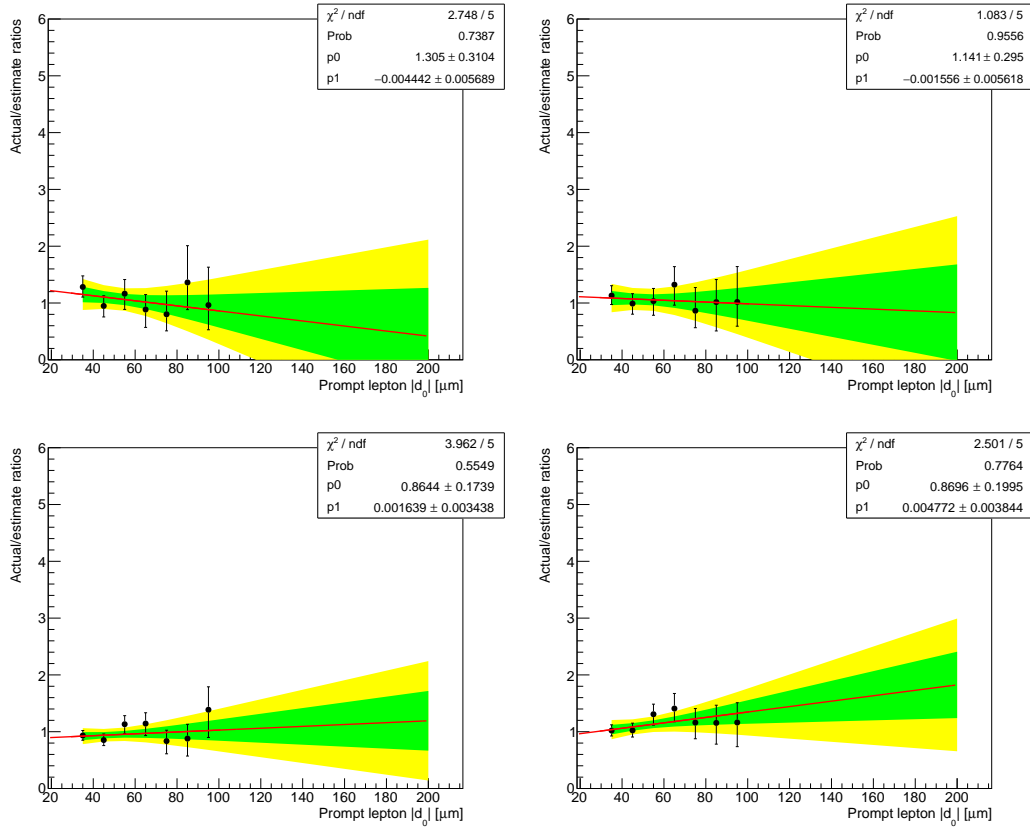


Figure 3.24: Background estimation closure tests in data, in 100–500 μm subregions of regions B (left) and C (right) in the ee channel. Each plot shows the ratio of the actual to the estimated number of events as a function of the prompt lepton $|d_0|$ in 2016 (top) and 2017–18 (bottom). A linear fit is shown in black along with the 68 % and 95 % confidence intervals of the extrapolated fit value.

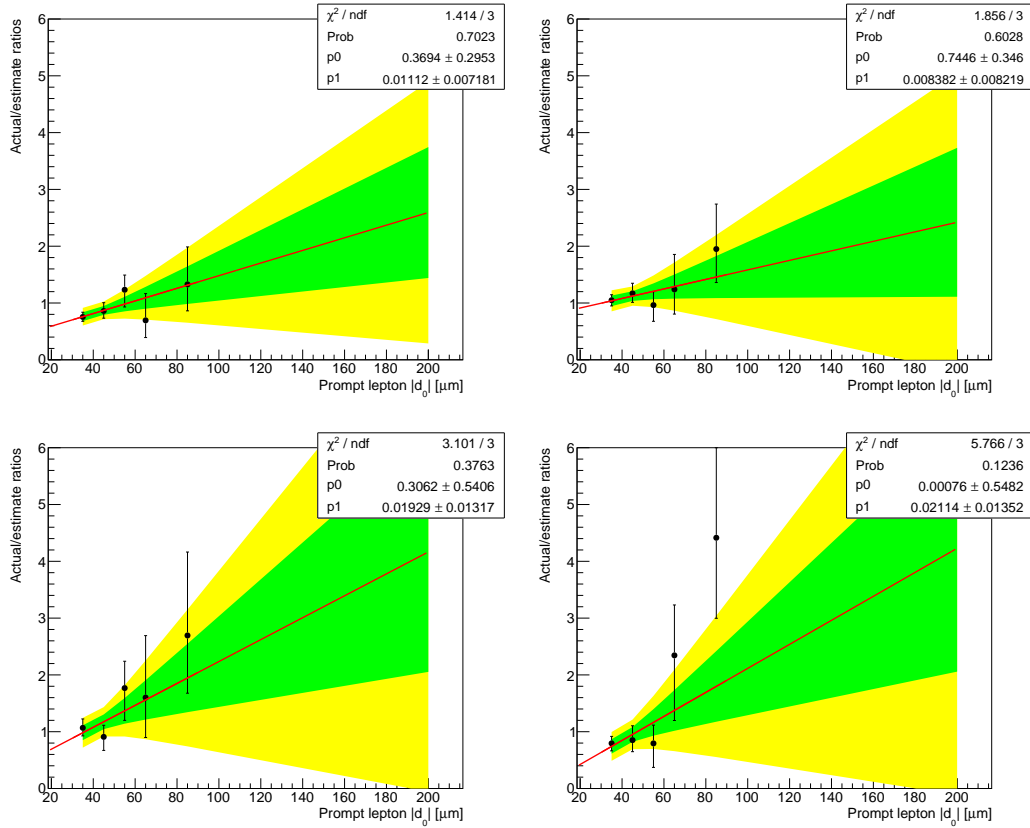


Figure 3.25: Background estimation closure tests in data, in 100–500 μm subregions of regions B (left) and C (right) in the $\mu\mu$ channel. Each plot shows the ratio of the actual to the estimated number of events as a function of the prompt lepton $|d_0|$ in 2016 (top) and 2017–18 (bottom). A linear fit is shown in black along with the 68 % and 95 % confidence intervals of the extrapolated fit value.

Table 3.14: The correction factors and the uncorrected and corrected background estimates in SR I . The correction factor uncertainties include both the uncertainty in the average and the additional uncertainty obtained from varying the fit extrapolation point. The total uncertainty (statistical plus systematic) is given for the corrected background estimates.

	Correction factor	Uncorrected estimate	Corrected estimate
2016 $e\mu$	$1.0^{+1.3}_{-1.0}$	$4.21^{+0.38}_{-0.40}$	$4.2^{+5.4}_{-4.2}$
2017+2018 $e\mu$	3.0 ± 1.0	$12.53^{+0.64}_{-0.61}$	38 ± 13
2016 ee	1.00 ± 0.60	$18.30^{+0.94}_{-0.91}$	18 ± 11
2017+2018 ee	$1.51^{+0.43}_{-0.42}$	41.6 ± 1.3	63^{+18}_{-17}
2016 $\mu\mu$	2.5 ± 1.0	3.07 ± 0.08	7.7 ± 3.1
2017+2018 $\mu\mu$	4.2 ± 1.8	1.00 ± 0.04	4.2 ± 1.8

1285 estimate. If the average is ≤ 1.0 , we set the correction equal to 1.0 and use the un-
 1286 certainty in the average as a symmetric systematic uncertainty about 1.0. Table 3.14
 1287 shows the resulting correction factors along with the uncorrected and corrected SR I
 1288 background estimate.

1289 **500 μm –10 cm systematic uncertainty**

1290 In the 500 μm –10 cm region, we derive a systematic uncertainty in the background
 1291 estimate from the data closure tests shown in Section 3.5.3. We take the largest
 1292 deviation from 1.0 that occurs in the ratio of the actual to the estimated number
 1293 of events plus its uncertainty, in either of the two closure tests that correspond to a
 1294 given SR, as a systematic uncertainty. This is a conservative approach that produces
 1295 a large systematic uncertainty in the small background yields that we predict in these
 1296 regions. Table 3.15 shows the systematic uncertainty and the predicted number of
 1297 events in SRs II, III, and IV.

Table 3.15: The systematic uncertainty and the background estimates in SRs II, III, and IV. The total uncertainty (statistical plus systematic) is given for each estimate.

	Systematic uncertainty	SR II	SR III	SR IV
2016 $e\mu$	98%	0.15 ± 0.15	$0.09^{+0.12}_{-0.09}$	$0.003^{+0.004}_{-0.003}$
2017+2018 $e\mu$	106%	$0.71^{+0.76}_{-0.71}$	$0.23^{+0.27}_{-0.23}$	$0.01^{+0.02}_{-0.01}$
2016 ee	199%	$0.51^{+1.02}_{-0.51}$	$0.43^{+0.85}_{-0.43}$	$0.01^{+0.02}_{-0.01}$
2017+2018 ee	37%	3.6 ± 1.4	2.8 ± 1.1	$0.24^{+0.10}_{-0.09}$
2016 $\mu\mu$	64%	0.17 ± 0.11	0.19 ± 0.12	0.01 ± 0.01
2017+2018 $\mu\mu$	140%	$0.14^{+0.19}_{-0.14}$	$0.08^{+0.12}_{-0.08}$	$0.01^{+0.02}_{-0.01}$

3.5.5 Testing full background estimation procedure

Having defined the full background estimation procedure and seen that the $|d_0^a|$ -
 $|d_0^b|$ correlation observed in data is also present in simulated background events, we
now perform a final closure test of the full background estimation method using
simulated background events in SRs I–IV.

Table 3.16 shows the estimated and actual number of simulated background events
in SRs I–IV. The listed estimates include all corrections and statistical and system-
atic uncertainties as discussed in 3.5.4. The uncertainties in the actual values are
purely statistical. The general agreement between estimated and actual yields leads
us to conclude that the background estimation procedure is valid and the assigned
systematic uncertainties are sufficient to cover any potential sources of nonclosure
that we have not explicitly considered.

Table 3.16: Closure test results in background simulation in the SRs, with the correction applied. The estimated number of events, the actual number of events, and their total uncertainties (statistical plus systematic) are given. In cases where the actual number of events is zero, the uncertainty is given by the product of the average background simulation event weight and the upper bound of the 68% Poisson interval given by a single observation of zero events.

	SR I	SR II	SR III	SR IV
2016 $e\mu$ estimated	$7.4^{+4.8}_{-4.2}$	0.07 ± 0.07	$0.096^{+0.105}_{-0.096}$	0.001 ± 0.001
2016 $e\mu$ actual	$5.0^{+1.5}_{-1.2}$	$0.07^{+0.09}_{-0.05}$	$0.005^{+0.011}_{-0.004}$	$0.000^{+0.037}_{-0.000}$
2017+2018 $e\mu$ estimated	13.5 ± 6.4	$0.37^{+0.40}_{-0.37}$	$0.34^{+0.36}_{-0.34}$	0.02 ± 0.02
2017+2018 $e\mu$ actual	$19.1^{+11.4}_{-7.6}$	$0.52^{+0.41}_{-0.25}$	$0.00^{+0.24}_{-0.00}$	$0.00^{+0.24}_{-0.00}$
2016 ee estimated	9.3 ± 5.0	$0.12^{+0.23}_{-0.12}$	$0.14^{+0.28}_{-0.14}$	$0.002^{+0.004}_{-0.002}$
2016 ee actual	$13.4^{+3.4}_{-2.8}$	$0.15^{+0.19}_{-0.09}$	$1.03^{+1.36}_{-0.67}$	$0.000^{+0.550}_{-0.000}$
2017+2018 ee estimated	18 ± 11	$0.59^{+0.27}_{-0.26}$	$0.45^{+0.21}_{-0.20}$	0.02 ± 0.01
2017+2018 ee actual	$8.2^{+6.5}_{-3.9}$	$0.17^{+0.23}_{-0.11}$	$0.00^{+0.17}_{-0.00}$	$0.00^{+0.17}_{-0.00}$
2016 $\mu\mu$ estimated	1.3 ± 0.6	0.04 ± 0.04	0.03 ± 0.03	0.002 ± 0.002
2016 $\mu\mu$ actual	$3.3^{+1.8}_{-1.2}$	$0.11^{+0.14}_{-0.07}$	$0.06^{+0.14}_{-0.05}$	$0.000^{+0.110}_{-0.000}$
2017+2018 $\mu\mu$ estimated	2.7 ± 1.4	0.04 ± 0.04	0.02 ± 0.02	0.002 ± 0.002
2017+2018 $\mu\mu$ actual	$7.1^{+6.9}_{-3.8}$	$0.00^{+0.15}_{-0.00}$	$0.00^{+0.15}_{-0.00}$	$0.078^{+0.179}_{-0.064}$

1310 **3.5.6 Additional background checks**

1311 We perform a few additional studies to check for other potential sources of back-
1312 ground. We find that their SR contributions are either negligible or already covered
1313 by the background estimation method described above.

1314 **Material interactions**

1315 In order to further study the material interactions, we invert the preselection
1316 criterion that rejects good vertices in the material. In data, we find seven events,
1317 across all channels and years, that pass the preselection with this inverted criterion.
1318 As shown in Table 3.17, three of these events are in the prompt control region and
1319 four are in region B or region C. The lepton vertices in these events coincide with the
1320 material as we expect: two are in the beampipe, one is in the pixel detector inner
1321 shield, and four are in the first layer of the pixel detector. Even with the material
1322 interaction veto inverted, we find no SR events resulting from material interactions
1323 and therefore conclude that material interactions are not a significant background
1324 after the full selection is applied.

Table 3.17: Some properties of the seven events found in data with the material interactions selection inverted.

Channel, Era	(d_0^a , d_0^b) [μm]	Region	Vertex (x, y, z) [cm]	Material
$e\mu$, 2017C	(-14, -10)	A	(-2.5, 1.4, 6.8)	pixel L1
$e\mu$, 2018D	(46, -14)	A	(0.9, 2.1, 0.1)	beampipe
ee , 2018D	(198, -34)	B	(-1.9, 0.5, 2.7)	beampipe
$\mu\mu$, 2016G	(407, -8)	B	(-1.4, 4.0, 6.3)	pixel L1
$\mu\mu$, 2016G	(-17, -2215)	C	(-2.6, 3.1, 6.6)	pixel L1
$\mu\mu$, 2016H	(2, 0)	A	(-1.6, -3.5, 12)	inner shield
$\mu\mu$, 2017F	(522, -13)	B	(-1.1, -3.0, -7.5)	pixel L1

1325 **Cosmic-ray muons**

1326 To estimate the SR contribution of cosmic-ray muons, we perform a study in which
1327 we invert the Δt and $\cos \alpha$ criteria in the $\mu\mu$ preselection and check how many events
1328 are in the SRs. We find three data events with the criteria inverted (one event per year,
1329 all in SR IV). Next, we use NoBPTX data, which is dominated by cosmic-ray muon
1330 events, to estimate the efficiency for cosmic-ray muons to pass the Δt and $\cos(\alpha)$
1331 criteria after passing the rest of the $\mu\mu$ preselection criteria. While 3736 NoBPTX
1332 data events pass the preselection criteria with the Δt and $\cos(\alpha)$ criteria removed,
1333 zero NoBPTX data events pass the full preselection. To conservatively estimate the
1334 efficiency, we fluctuate the number of passing events up to 1 and find an efficiency
1335 of $1/3736$. We therefore find the approximate upper bound on the SR contribution
1336 of cosmic ray muons to be $3 \times \frac{1}{3736} = 0.0008$, which is negligible compared to the
1337 background estimation in each SR.

1338 **Heavy-flavor mesons**

1339 We perform two studies to estimate an upper limit on the SR contribution of
1340 leptons from heavy-flavor mesons. First, we estimate SR yields with a simple ABCD
1341 method in 2018 $\mu\mu$ preselection data while additionally requiring at least one medium
1342 CSVv2 b -tagged jet [74]. The test is performed in the $\mu\mu$ channel because it contains
1343 the smallest relative SR contribution from mismeasurements and should therefore be
1344 most sensitive to heavy flavor. As shown in Table 3.18, the background estimates are
1345 about an order of magnitude smaller than when no b -tagged jet is required in our
1346 usual preselection.

Table 3.18: Background estimates in data while applying the 2018 $\mu\mu$ preselection and the additional requirement of at least one b -tagged jet. The estimates with at least one b -tagged jet are about an order of magnitude below the nominal prediction.

	SR I	SR II	SR III	SR IV
Preselection (corrected)	2.6 ± 1.0	$0.09^{+0.12}_{-0.09}$	$0.05^{+0.07}_{-0.05}$	$0.007^{+0.010}_{-0.007}$
Preselection + 1 b jet	0.19 ± 0.03	$0.008^{+0.007}_{-0.004}$	$0.005^{+0.004}_{-0.002}$	$0.0002^{+0.0002}_{-0.0001}$

1347 Next, we look at 2018 data and simulated QCD multijet events that pass the $\mu\mu$
 1348 preselection with the isolation criterion inverted. These samples are dominated by
 1349 muons from B meson decays, and the QCD simulation describes the data well in the
 1350 region outside of the Z boson peak, as shown in Fig. 3.26. We use this QCD multijet
 1351 sample to test the heavy-flavor background in two ways. First, we perform a simple
 1352 ABCD estimate in the simulated QCD multijet events to check for $|d_0^a| - |d_0^b|$ correlation.
 1353 As shown in Table 3.19, we find no evidence of correlation, which indicates that the
 1354 background estimation already accounts for the heavy-flavor background. Second,
 1355 we estimate the approximate heavy-flavor background in the SRs by taking the ratio
 1356 of SR to prompt control region events in QCD multijet simulation from the anti-
 1357 isolated region and the normalization from the number of simulated QCD multijet
 1358 events that pass the $\mu\mu$ preselection. Using this approach, we estimate that the
 1359 heavy-flavor background to be $0.06^{+0.13}_{-0.05}$ events in SR I and $0.0015^{+0.0034}_{-0.0012}$ events in
 1360 SR IV, which is small relative to the nominal prediction shown in the first row of
 1361 Table 3.18.

1362 We therefore conclude that the heavy-flavor SR contribution is small and already
 1363 accounted for in our background estimates.

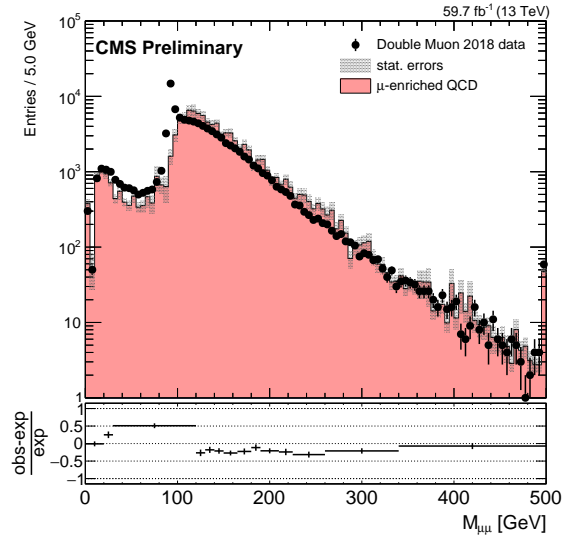


Figure 3.26: The dimuon invariant mass distribution in the $\mu\mu$ channel with the muon isolation criterion inverted, for 2018 data and QCD multijet simulation.

Table 3.19: A closure test of the ABCD method in 2018 QCD simulation in the $\mu\mu$ channel with the muon isolation criterion inverted. The estimates from the ABCD method, the actual yields in simulation, and the ratios of the actual to the estimated yields are shown.

Region	Estimated yield	Actual yield	Ratio of actual to estimate
SR I	9500 ± 1100	11000 ± 1000	1.2 ± 0.2
SR II	1740^{+310}_{-280}	2200^{+330}_{-290}	1.3 ± 0.3
SR III	1450^{+280}_{-240}	1500^{+180}_{-160}	1.0 ± 0.2
SR IV	265^{+62}_{-54}	268^{+61}_{-50}	1.0 ± 0.3

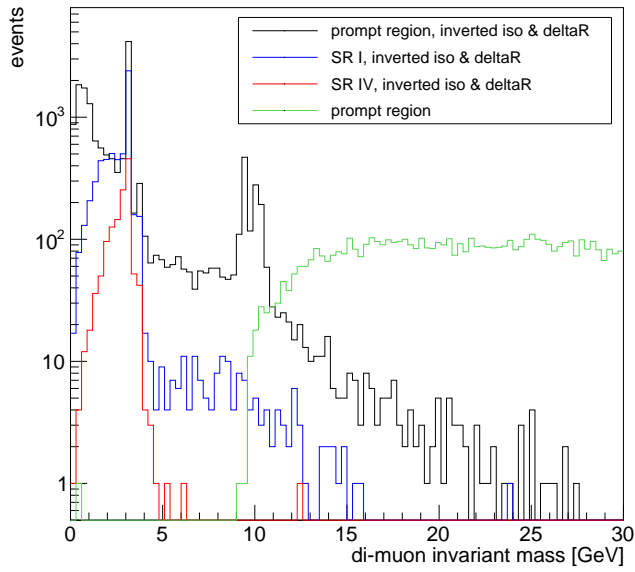


Figure 3.27: The dimuon invariant mass distribution in 2018 data in the $\mu\mu$ channel, in the prompt control region (black), SR I (blue), SR IV (red), with the muon isolation and di-muon ΔR criteria inverted. The equivalent distribution from the prompt control region is also shown in green.

1364 **Low-mass SM hadrons**

1365 To estimate an upper limit on the SR contribution of leptons from decays of low-
1366 mass SM hadrons, we examine 2018 data and QCD multijet simulation in the $\mu\mu$
1367 channel with both the muon isolation and the ΔR requirements inverted. As shown
1368 in Fig. 3.27, this region is dominated low-mass $\mu\mu$ pairs, with clear J/ψ , ψ' , and Υ
1369 mass peaks. Many of these leptons are displaced, especially those in the J/ψ mass
1370 range. To estimate the fraction of such leptons that will be displaced, we take the
1371 ratio of SR to prompt control region events of SM hadrons that decay to leptons from
1372 data in this region.

Even though the inverted-isolation region is dominated by low-mass muon pairs, the only QCD multijet simulation event that survives the 2018 $\mu\mu$ preselection has a di-muon invariant mass of approximately 300 GeV. Furthermore, the muons are not near each other in the η - ϕ plane ($\Delta R \approx 3$), which is inconsistent with the low-mass SM hadron events that dominate the region with the inverted isolation and ΔR criteria. To find a normalization from which to estimate the low-mass SM hadron SR contribution, we therefore turn to the inverted-isolation sample used above in the heavy-flavor meson cross check. In this sample, the ratio of events with $\Delta R < 0.5$ to events with $2.8 < \Delta R < 3.2$ is about 0.1. We find 0.2 QCD multijet simulated events that pass the nominal preselection, and so we estimate that of the events passing the 2018 $\mu\mu$ preselection, about 0.02 contain pairs of muons produced in low-mass SM hadron decays. We estimate the SR contributions using this preselection normalization and the ratio of SR to prompt control region events from the sample of SM hadrons that decay to leptons in data. We find this contribution is less than 0.006 $^{+0.013}_{-0.005}$ events in SR I and less than 0.001 $^{+0.002}_{-0.001}$ events in SR IV, which, if compared with the nominal prediction shown in the first row of Table 3.26, are respectively negligible and easily covered by the 140 % systematic uncertainty already applied to the background prediction in this region.

1391 **3.6 Systematic uncertainties**

1392 Several systematic uncertainties are applied to the simulated signal efficiency to
1393 account for uncertainty in the signal yields arising from possible mismodeling of the
1394 detector conditions and response. The following subsections describe each systematic
1395 uncertainties in turn, and Table 3.20 summarizes all systematic uncertainties applied
1396 to the simulated signal.

1397 **3.6.1 Integrated luminosity**

1398 The integrated luminosities of the 2016, 2017, and 2018 data-taking periods are
1399 individually known with uncertainties in the 2.3–2.5 % range [75, 76, 77], while the
1400 total Run 2 (2016–2018) integrated luminosity has an uncertainty of 1.8 %, the im-
1401 provement in precision reflecting the uncorrelated time evolution of some systematic
1402 effects. The full table of 2016–2018 integrated luminosity uncertainties are taken from
1403 Ref. [78], with the correlations specified therein.

1404 **3.6.2 Pileup**

1405 The simulation of pileup events assumes a total inelastic proton-proton cross sec-
1406 tion of 69.2 mb with an associated uncertainty of 5 % [79]. The systematic uncertainty
1407 arising as a result of the modeling of pileup events is estimated by varying the cross
1408 section of the minimum bias events by 5 % when generating the target pileup distri-
1409 butions. The pileup weights are recomputed with these new distributions and applied
1410 to the simulated events to obtain the variation in the yields in the inclusive signal
1411 region. The average uncertainty is between 1 and 2 %. We treat these uncertainties
1412 as 100 % correlated across the three years of data taking.

Table 3.20: Systematic uncertainties in the signal efficiency for all three years and the three channels. The mean is provided in cases where the uncertainty varies by signal sample. Uncertainties in the same row are treated as correlated among the years of data taking, except for the displaced tracking and muon pixel hit efficiencies, where the 2016 uncertainty is treated as uncorrelated with the 2017 and 2018 uncertainties.

Systematic uncertainty	2016	2017	2018
<i>Integrated luminosity</i>	1.8%	1.8%	1.8%
<i>Pileup</i>			
- $e\mu$ channel	0.5%	0.6%	0.5%
- ee channel	0.5%	0.9%	0.8%
- $\mu\mu$ channel	0.2%	0.1%	0.2%
<i>Displaced tracking efficiency</i>	14%	5.8%	2.4%
<i>Trigger efficiency</i>			
- $e\mu$ channel, electrons	1.6%	1.3%	1.2%
- $e\mu$ channel, muons	1.6%	1.4%	1.2%
- ee channel	10%	13%	19%
- $\mu\mu$ channel	1.2%	1.0%	1.1%
<i>Muon trigger efficiency at large d_0</i>			
- $e\mu$ channel, muons	20%	20%	20%
- $\mu\mu$ channel	20%	20%	20%
<i>Lepton identification and isolation</i>			
- $e\mu$ channel, electrons	1.2%	3.6%	3.5%
- $e\mu$ channel, muons	0.05%	0.07%	0.06%
- ee channel	2.4%	7.2%	7.0%
- $\mu\mu$ channel	0.10%	0.14%	0.12%
<i>Muon pixel hit efficiency</i>			
- $e\mu$ channel, muons	32%	12%	16%
- $\mu\mu$ channel	73%	23%	30%
<i>Lepton d_0 correction</i>			
- $e\mu$ channel, electrons	—	0.001%	0.001%
- $e\mu$ channel, muons	—	0.003%	0.001%
- ee channel	—	0.11%	0.11%
- $\mu\mu$ channel	—	0.11%	0.11%

1413 **3.6.3 Displaced tracking efficiency**

1414 The systematic uncertainty associated with the modeling of the displaced tracking
1415 efficiency is derived from a dedicated study using cosmic ray muons. Following the
1416 results of the study presented in Appendix C, we assign 14.1%, 5.8%, and 2.4%
1417 systematic uncertainties in 2016, 2017, and 2018, respectively. Because the CMS pixel
1418 detector was upgraded between 2016 and 2017 data taking, we treat the 2017 and
1419 2018 systematic uncertainties as fully correlated and the 2016 systematic uncertainty
1420 as uncorrelated with 2017 and 2018.

1421 **3.6.4 Trigger efficiency**

1422 The trigger efficiency systematic uncertainty is given by the uncertainty in the
1423 measured trigger efficiency scale factors (see Section 3.4.4). These uncertainties are
1424 1% or less for the $e\mu$ and $\mu\mu$ channels and about 10% for the ee channel. In addition,
1425 we have studied the trigger efficiency in signal as a function of $|d_0|$ for events in the
1426 trigger p_T plateau. To cover the change observed in the muon trigger efficiency over
1427 the full $|d_0|$ range, we assign an additional 20% uncertainty.

1428 We treat the trigger efficiency uncertainties as 100% correlated across the three
1429 years of data taking.

1430 **3.6.5 Lepton ID and isolation**

1431 To find the systematic uncertainty associated with the corrections to the lepton
1432 ID and isolation, we fluctuate the lepton scale factors up and down by their uncer-
1433 tainty and observe the change in the event yields in the inclusive signal region. The
1434 average uncertainty for electrons is about 3% in the $e\mu$ channel and about 7% in

1435 the ee channel, while the average uncertainty for muons is $< 1\%$. We treat these
1436 uncertainties as 100 % correlated across the three years of data taking.

1437 **3.6.6 Muon pixel hit efficiency**

1438 The requirement in the muon ID that muons have at least one pixel hit could in
1439 principle have some appreciable $|d_0|$ dependence, so we perform a dedicated study
1440 to ensure that we account for any differences in $|d_0|$ dependence between data and
1441 simulation. Figure 3.28 shows the efficiency of this requirement in cosmic simulation
1442 and NoBPTX data (described in appendix C) as a function of muon $|d_0|$. For events
1443 in the denominator of these plots, we require that at least 2 global, PF muons have
1444 $|\eta| < 1.0$, $p_T > 25 \text{ GeV}$, no displaced vertices in the tracker material, $|d_z| < 15 \text{ cm}$,
1445 and pass all the tight ID criteria except the pixel hit requirement. We also require
1446 the muons to be separated by $\Delta R > 0.2$. The events in the numerator must pass the
1447 same requirements in addition to the requirement that the muons have at least one
1448 pixel hit. From this plot, we calculate the mean efficiency to identify the muons in the
1449 simulated signal events using the same procedure as is used for the displaced tracking
1450 efficiency systematic uncertainty described in Appendix C. We repeat the procedure
1451 in both cosmic simulation and in NoBPTX data, and using the ratio of these two
1452 efficiencies, we derive the relative systematic uncertainty in the signal. The average
1453 uncertainty is about 16 % (32 %) in the $e\mu$ ($\mu\mu$) channel. As the pixel detector was
1454 upgraded after 2016, the 2017 and 2018 systematic uncertainties are treated as fully
1455 correlated while the 2016 uncertainty is treated as uncorrelated with the 2017 and
1456 2018 uncertainties.

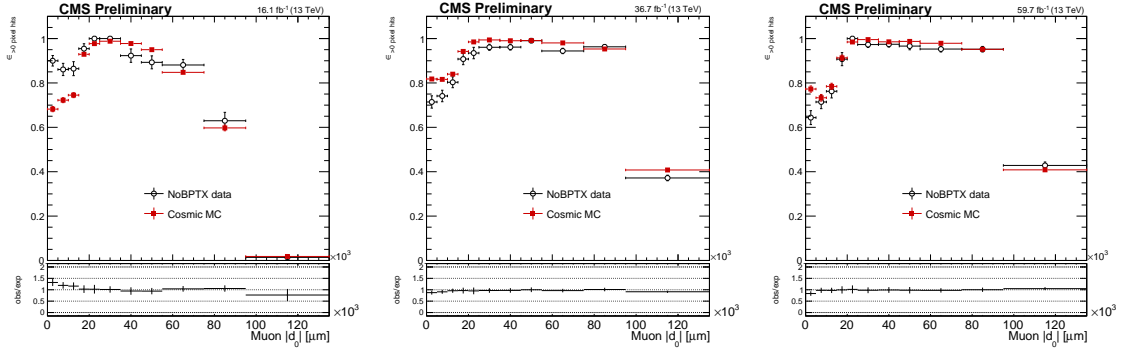


Figure 3.28: The pixel hit efficiency as a function of muon $|d_0|$, for cosmic simulation and NoBPTX data in 2016 (left), 2017 (middle), and 2018 (right) conditions.

1457 3.6.7 Lepton d_0 resolution

1458 To find the systematic uncertainty associated with the corrections to the lepton
 1459 d_0 (see Section 3.4.3), we fluctuate the lepton d_0 corrections up and down by their
 1460 uncertainty and observe the change in the event yields in the inclusive signal region.
 1461 The average uncertainty is $< 1\%$. We treat these uncertainties as 100 % correlated
 1462 in 2017 and 2018. No d_0 correction or systematic uncertainty is needed for 2016
 1463 simulation.

1464 **3.7 Results**

1465 After unblinding and comparing the observed SR yields with the predicted back-
1466 ground yields, we find no significant excess. Table 3.21 shows the predicted number
1467 of background events and the observed yields in each SR, and Figs. 3.29 and 3.30
1468 visually summarize this same information.

1469 **3.7.1 Observed events**

1470 In general, the observed SR events appear to be SM events from proton-proton
1471 collisions. Specifically, we see no evidence of leptons from cosmic rays, material inter-
1472 actions, or signal. Figure 3.31 shows two-dimensional $|d_0|$ distributions of data events
1473 that pass the preselection, and Fig. 3.32 shows the same but for data events in the
1474 inclusive SR. As expected for SM background, the observed events are concentrated
1475 in the low $|d_0|$ region.

1476 We also use event display visualizations to examine each observed SR event indi-
1477 vidually and record our observations below.

1478 In the $e\mu$ channel, the SR events tend to have several jets and often have $p_T^{\text{miss}} >$
1479 100 GeV. Many events have muon ϕ values such that the muon system hits are all
1480 near the edges of detector sections or muon η values such that the muon is near the
1481 barrel/endcap transition in the muon system. There are also a few events in which
1482 the electron and/or muon are associated with a different primary vertex than their
1483 associated track.

1484 In the ee channel, the majority of SR events contain at least one electron with
1485 $|\eta| > 1.1$, which increases the probability that their d_0 is poorly measured. Across all
1486 three years, most events fall into one of three categories:

Table 3.21: The number of estimated background and observed events in each channel and SR. For each estimate, the total uncertainty is given. The p_T boundaries that separate the low- and high- p_T bins of SR I are listed in Table 3.11.

	SR I, low p_T bin	SR I, high p_T bin	SR II	SR III	SR IV
<i>2016 eμ</i>					
- estimated	$3.8^{+4.8}_{-3.8}$	$0.41^{+0.53}_{-0.41}$	$0.09^{+0.12}_{-0.09}$	0.15 ± 0.15	$0.003^{+0.004}_{-0.003}$
- observed	8	1	0	0	0
<i>2017+2018 eμ</i>					
- estimated	38 ± 13	$0.75^{+0.41}_{-0.34}$	$0.23^{+0.27}_{-0.23}$	$0.71^{+0.76}_{-0.71}$	$0.01^{+0.02}_{-0.01}$
- observed	28	3	0	1	0
<i>2016 ee</i>					
- estimated	18 ± 11	$0.22^{+0.17}_{-0.16}$	$0.51^{+1.02}_{-0.51}$	$0.43^{+0.85}_{-0.43}$	$0.01^{+0.02}_{-0.01}$
- observed	40	0	0	1	0
<i>2017+2018 ee</i>					
- estimated	62^{+18}_{-17}	$0.85^{+0.33}_{-0.35}$	2.8 ± 1.1	3.6 ± 1.4	$0.24^{+0.10}_{-0.09}$
- observed	48	0	1	4	0
<i>2016 $\mu\mu$</i>					
- estimated	7.4 ± 3.0	0.25 ± 0.11	0.17 ± 0.11	0.19 ± 0.12	0.01 ± 0.01
- observed	15	0	0	1	0
<i>2017+2018 $\mu\mu$</i>					
- estimated	3.5 ± 1.5	0.69 ± 0.31	$0.08^{+0.12}_{-0.08}$	$0.14^{+0.19}_{-0.14}$	$0.01^{+0.02}_{-0.01}$
- observed	1	1	1	1	0

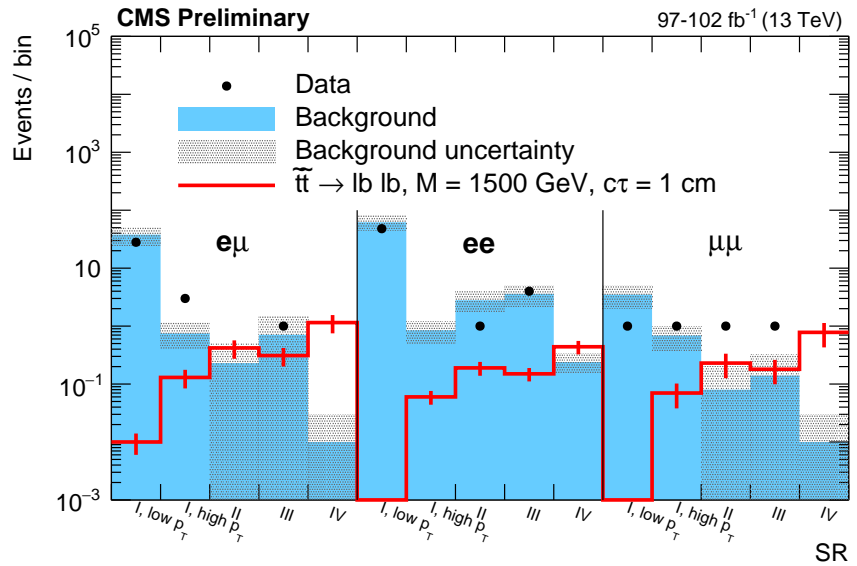
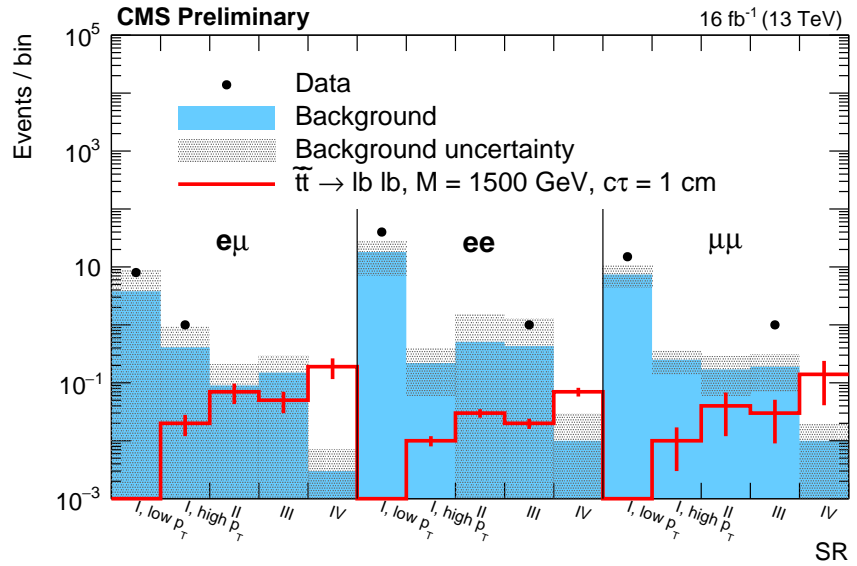


Figure 3.29: The number of estimated background and observed events in each channel and SR, with a representative signal overlaid, for 2016 (top) and 2017–2018 (bottom). For each background estimate and signal yield, the total uncertainty is given.

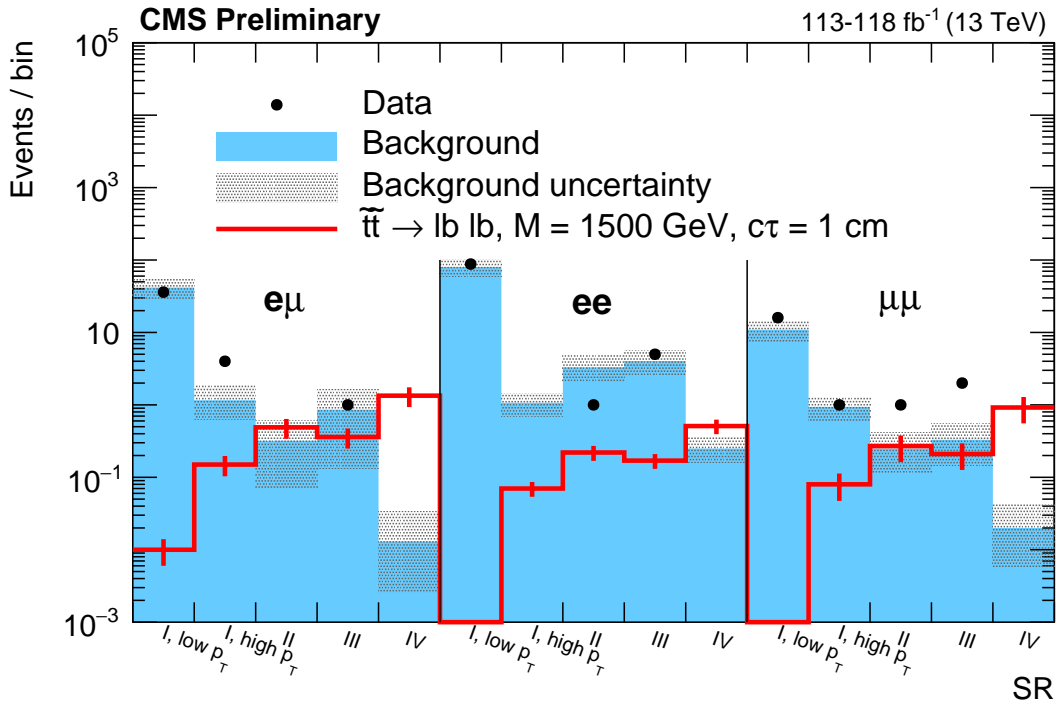


Figure 3.30: The number of estimated background and observed events in each channel and SR, with a representative signal overlaid, for 2016–2018. For each background estimate and signal yield, the total uncertainty is given.

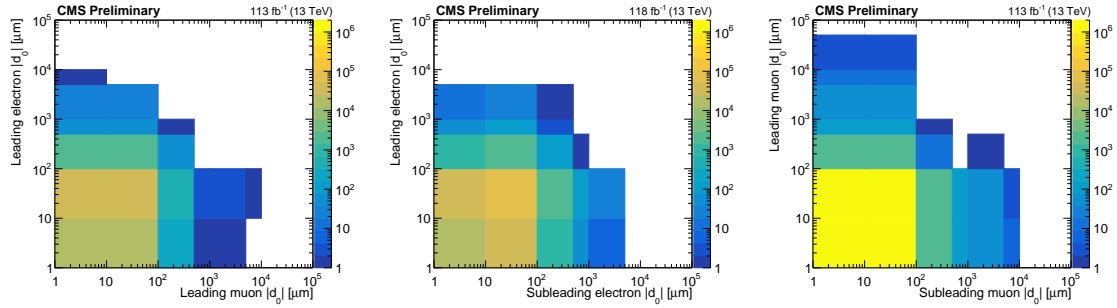


Figure 3.31: Two-dimensional distributions of $|d_0^a|$ and $|d_0^b|$, for the events in data that pass the $e\mu$ (left), ee (middle), and $\mu\mu$ (right) preselection. The bins along the x and y axes contain underflow. The inclusive signal region covers the region between $100 \mu\text{m}$ and 10 cm in each $|d_0|$ variable shown.

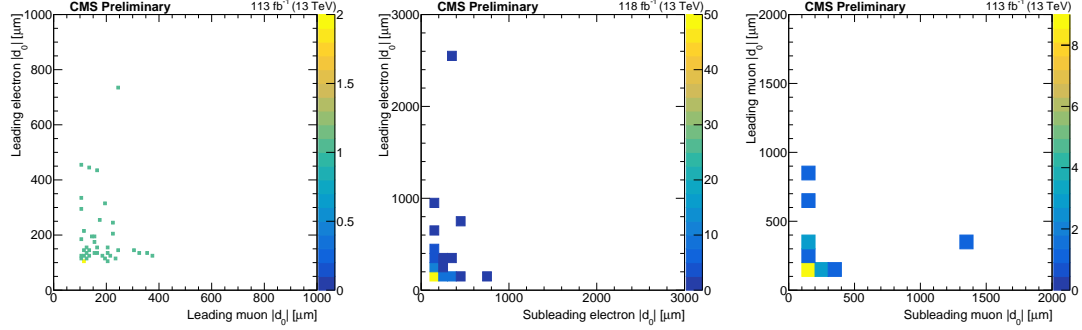


Figure 3.32: Two-dimensional distributions of $|d_0^a|$ and $|d_0^b|$, for data events in the inclusive SR in the $e\mu$ (left), ee (middle), and $\mu\mu$ (right) channels.

- 1487 1. Events with two electrons that appear to be from a boosted Z boson, with an
- 1488 invariant mass between 80 and 100 GeV, opposite one or two jets
- 1489 2. Events with two electrons approximately back-to-back in ϕ with an invariant
- 1490 mass greater than 100 GeV and p_T^{miss} usually between 10 and 40 GeV
- 1491 3. Events that are similar to type 2 but with at least one jet and frequently p_T^{miss}
- 1492 between 70 and 110 GeV

- 1493 In the $\mu\mu$ channel, many events have an invariant mass consistent with the mass
- 1494 of the Z boson and p_T^{miss} less than about 60 GeV. Most of the events found in 2017
- 1495 and 2018 have an invariant mass higher than than the Z boson mass and could be $t\bar{t}$
- 1496 events. Eight of the sixteen SR events in 2016 have two muons with ϕ values of about
- 1497 $\pm\pi/2$ (i.e. in the y - z plane). Every muon pair in these eight events have an invariant
- 1498 mass consistent with a Z boson, and the $\cos(\alpha)$ and Δt distributions of these muons
- 1499 confirm that they are not from cosmic rays. As shown in Fig. 3.33, these features are
- 1500 clearly visible in the ϕ and di-muon invariant mass distributions of the SR data when
- 1501 compared with background simulation. Thirteen of the sixteen muons in these eight

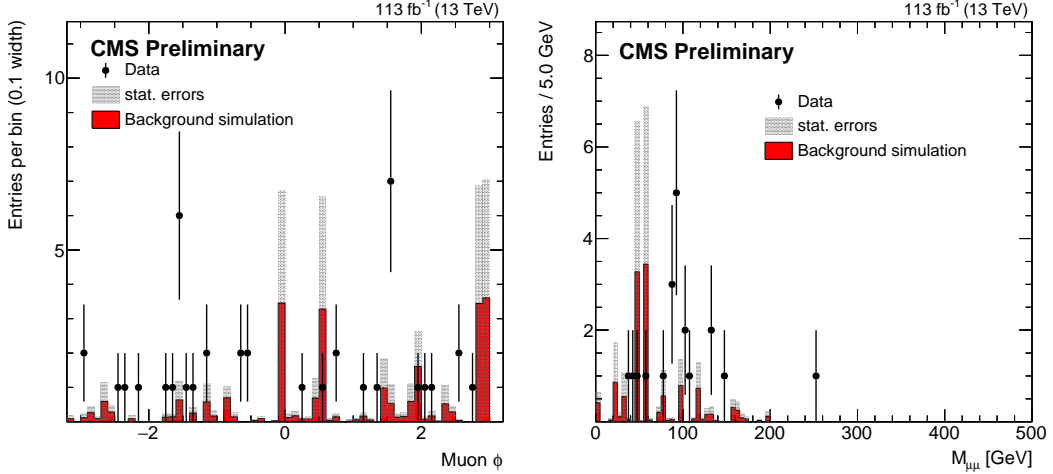


Figure 3.33: Muon ϕ and di-muon invariant mass distributions for data and composite background simulation in the $\mu\mu$ channel in the inclusive SR. The background simulation is normalized to the ABCD method background prediction.

1502 events have only one valid pixel hit, and event displays of these events show that the
 1503 muon track often passes between or at the edge of pixel modules near the place where
 1504 the two halves of the original pixel detector barrel are joined. We believe that this
 1505 feature causes the muon d_0 values to be poorly measured.

1506 3.7.2 Limits

1507 The data show no significant excess over background, so we set upper limits on the
 1508 product of the signal production cross section (σ) and branching fraction (\mathcal{B}) using
 1509 the HybridNew statistical method of the “Combine” tool developed by the CMS
 1510 Higgs working group [80, 81, 82, 83]. The ABCD estimate is performed in Combine,
 1511 which means that any signal contamination in the control regions is accounted for
 1512 automatically. We perform a simultaneous counting experiment in each signal region

1513 bin. Figure 3.34 shows the 95% confidence level (CL) upper limits on the top squark
1514 mass as a function of its lifetime.

1515 The variation in the size and shape of the exclusion regions between the three
1516 channels is mostly explained by variation in signal yields between the three channels.
1517 Looking at the high- p_T bin of SR I, which is the most sensitive bin for top squarks with
1518 large masses and small lifetimes, we find that the simulated signal yield is highest
1519 in the $e\mu$. This difference between the $e\mu$ and same-flavor channels is a result of
1520 simple combinatorics: the two independent top squark decays will result in an $e\mu$ final
1521 state twice as often as an ee or $\mu\mu$ final state. In this bin, the ee - and $\mu\mu$ -channel
1522 signal yields are similar. SR IV drives the sensitivity for top squarks with large
1523 lifetimes. Because CMS identifies muons with higher efficiency than it does electrons,
1524 the $\mu\mu$ channel has the largest simulated signal yield in SR IV when considering top
1525 squarks with lifetimes $\gtrsim 10$ cm. For this same reason, the ee channel has the smallest
1526 signal yield out of the three channels in SR IV when considering top squark lifetimes
1527 $\gtrsim 10$ cm. Taking all of these effects together, we find that the $e\mu$ channel is the most
1528 sensitive for lifetimes $\lesssim 10$ cm while the $\mu\mu$ channel is the most sensitive for lifetimes
1529 $\gtrsim 10$ cm.

1530 Figure 3.35 shows the 95% CL upper limits for the combination of the three
1531 channels. The top squark limits assume $\mathcal{B}(\tilde{t} \rightarrow bl) = \mathcal{B}(\tilde{t} \rightarrow dl) = 100\%$, and each l
1532 has an equal probability of being an electron, a muon, or a tau lepton.

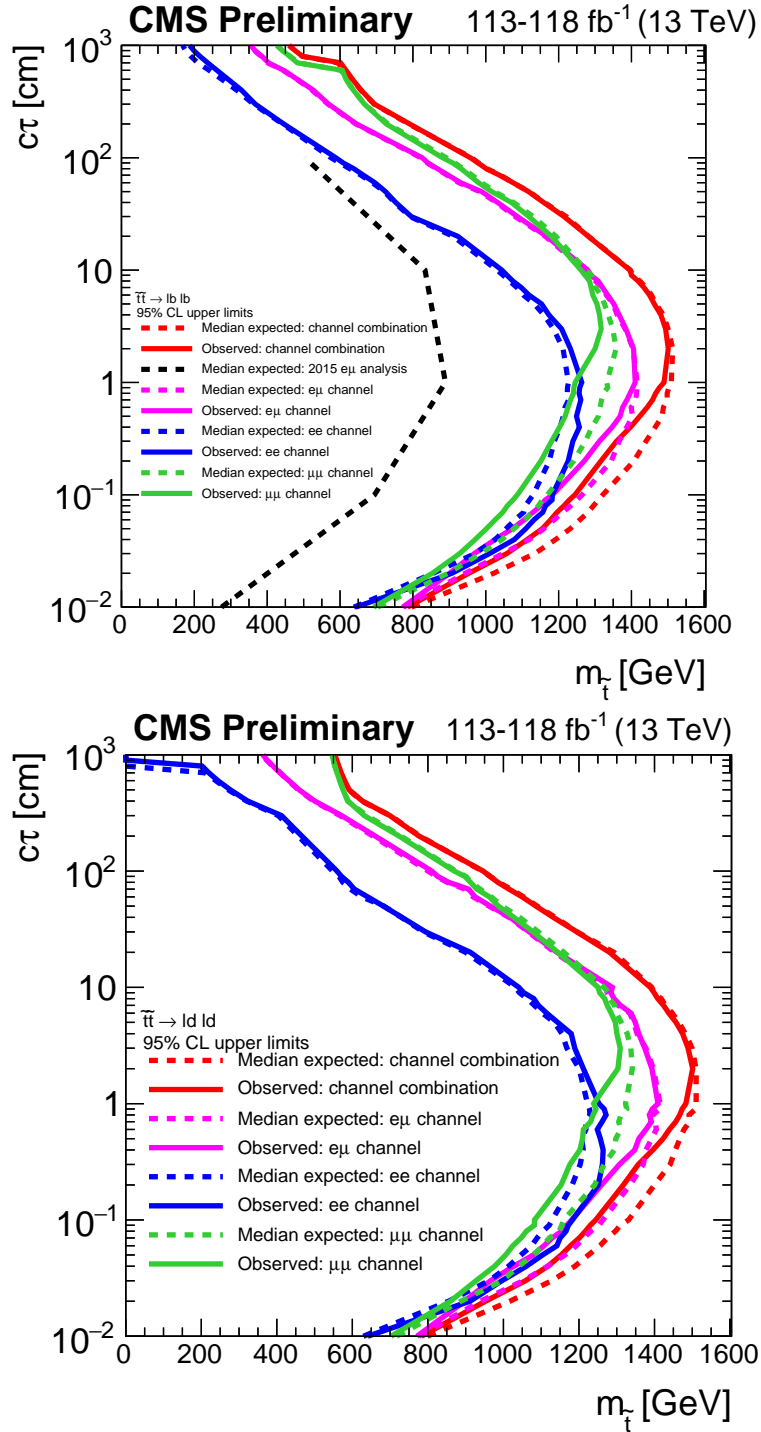


Figure 3.34: The 95% CL upper limits on the long-lived particle mass ($m_{\tilde{t}}$) as a function of its lifetime ($c\tau$), for the $e\mu$, ee , and $\mu\mu$ channels. The $\tilde{t}\tilde{t} \rightarrow \bar{l}b\bar{l}b$ (top) and $\tilde{t}\tilde{t} \rightarrow \bar{l}d\bar{l}d$ (bottom) processes are shown.

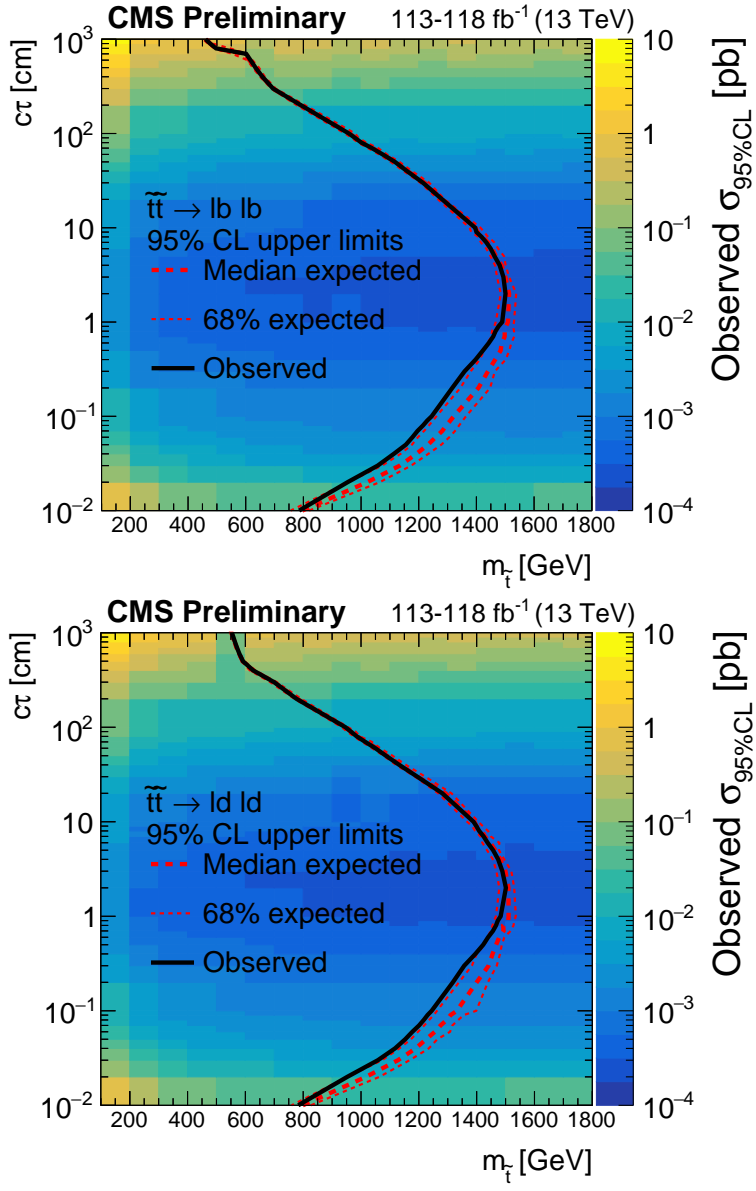


Figure 3.35: The 95% CL upper limits on the long-lived particle mass ($m_{\tilde{t}}$) as a function of its lifetime ($c\tau$). The colors indicate the observed 95% CL upper limit on the cross section. The $\tilde{t} \tilde{t} \rightarrow l b \bar{l} \bar{b}$ (left) and $\tilde{t} \tilde{t} \rightarrow l d \bar{l} \bar{d}$ (right) processes are shown.

1533 **3.7.3 Additional likelihood tests**

1534 We also perform several statistical tests to help assess the significance of the
1535 differences between the observed and predicted SR yields and to ensure that the
1536 likelihood is handling the observed yields in a reasonable way.

1537 We first compare the best-fit background yields under the background-only hy-
1538 pothesis while masking the signal regions with the best-fit background yields under
1539 the signal+background hypothesis using the full information from all signal and con-
1540 trol regions. For simplicity, we refer to the first quantity as the pre-fit prediction and
1541 the second as the post-fit prediction. Table 3.22 lists the pre- and post-fit predictions
1542 for each channel and SR, and Fig. 3.36 (left) shows associated pull distribution. We
1543 find that the differences between the pre- and post-fit predictions are consistent with
1544 the variation one would expect from purely statistical effects.

1545 Next, we examine the equivalent pull distribution for background yield nuisance
1546 parameters. Figure 3.36 (right) shows that the differences in nuisance parameter
1547 values before and after the fit are also consistent with the variation one would expect
1548 from purely statistical effects.

1549 Finally, we check the observed asymptotic significance of the $\tilde{t}\bar{t} \rightarrow \bar{l}b\bar{l}\bar{b}$ signal
1550 model. As shown in Fig. 3.37, the observed significance is less than two for all signal
1551 points we consider when looking at the combination of all channels as well as each
1552 channel individually. We therefore conclude that the observed yields do not constitute
1553 a significant excess.

Table 3.22: The pre- and post-fit predictions for each signal region bin.

	SR I, low p_T bin	SR I, high p_T bin	SR II	SR III	SR IV
<i>2016 eμ</i>					
- pre-fit	3.8 ± 3.9	0.40 ± 0.45	0.09 ± 0.11	0.15 ± 0.13	0.003 ± 0.003
- post-fit	7.1 ± 2.0	0.76 ± 0.31	0.08 ± 0.08	0.14 ± 0.14	0.003 ± 0.003
<i>2017+2018 eμ</i>					
- pre-fit	38 ± 14	0.75 ± 0.40	0.23 ± 0.37	0.71 ± 0.90	0.01 ± 0.02
- post-fit	31 ± 5	0.68 ± 0.25	0.20 ± 0.17	0.65 ± 0.48	0.01 ± 0.01
<i>2016 ee</i>					
- pre-fit	18 ± 11	0.22 ± 0.17	0.51 ± 2.41	0.43 ± 2.06	0.01 ± 0.06
- post-fit	35 ± 5	0.40 ± 0.14	0.50 ± 0.75	0.44 ± 0.53	0.01 ± 0.02
<i>2017+2018 ee</i>					
- pre-fit	62 ± 17	0.85 ± 0.31	2.8 ± 0.9	3.6 ± 1.2	0.25 ± 0.09
- post-fit	50 ± 6	0.65 ± 0.19	2.5 ± 0.7	3.2 ± 0.9	0.22 ± 0.06
<i>2016 $\mu\mu$</i>					
- pre-fit	7.4 ± 3.3	0.25 ± 0.11	0.17 ± 0.11	0.19 ± 0.12	0.01 ± 0.01
- post-fit	11 ± 2	0.37 ± 0.10	0.19 ± 0.10	0.21 ± 0.12	0.01 ± 0.01
<i>2017+2018 $\mu\mu$</i>					
- pre-fit	3.4 ± 1.6	0.69 ± 0.32	0.08 ± 0.12	0.14 ± 0.18	0.01 ± 0.02
- post-fit	2.5 ± 1.1	0.51 ± 0.22	0.14 ± 0.36	0.23 ± 0.63	0.02 ± 0.05

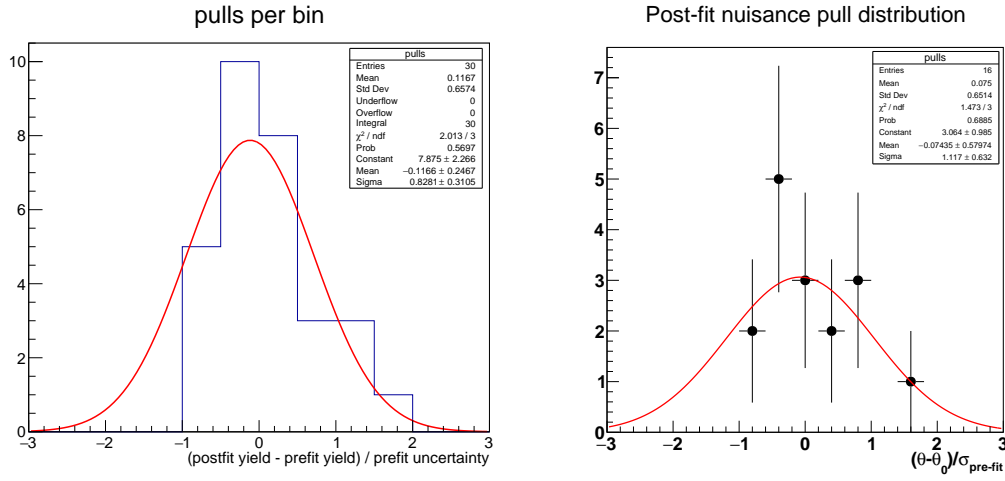


Figure 3.36: The distribution of pulls for each signal region bin, where pulls are calculated as the difference between the post-fit background yield and the pre-fit background yield divided by the pre-fit background uncertainty (left). The distribution of pulls for each background nuisance parameter, where pulls are calculated as the difference between the post-fit value and the pre-fit value divided by the pre-fit uncertainty (right).

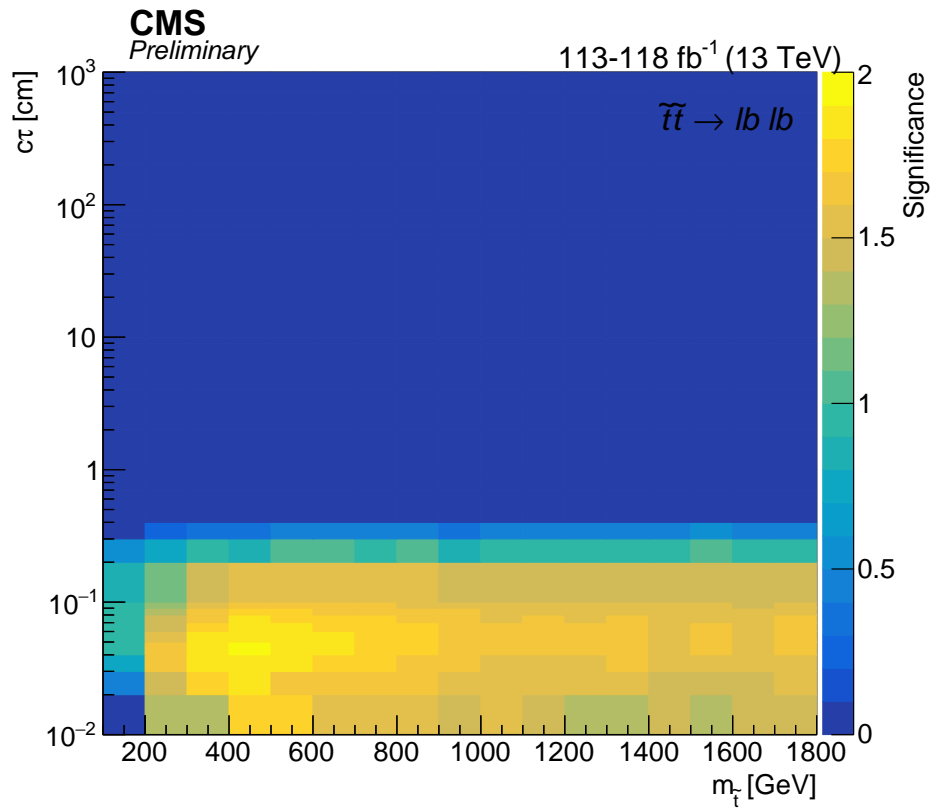


Figure 3.37: The observed asymptotic significances for the $\tilde{t}\tilde{t} \rightarrow l\bar{b} l\bar{b}$ process as a function of \tilde{t} mass and lifetime using the combined results.

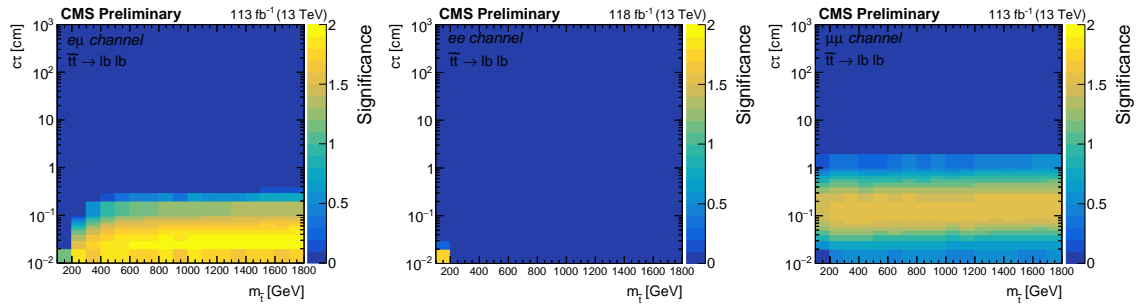


Figure 3.38: The observed asymptotic significances for the $\tilde{t}\tilde{t} \rightarrow l\bar{b} l\bar{b}$ process as a function of \tilde{t} mass and lifetime in the ee (left), $e\mu$ (center), $\mu\mu$ channels (right).

Chapter 4: Conclusion

1555 A search has been presented for new long-lived particles that propagate a mea-
1556 surable distance before decaying to leptons inside the CMS detector. The resulting
1557 displaced lepton signature is targeted by selecting events with two leptons (an electron
1558 and a muon, two electrons, or two muons) whose transverse impact parameters are
1559 between 0.01 and 10 cm. The search is performed in $113\text{--}118 \text{ fb}^{-1}$ of proton-proton
1560 collision data produced by the CERN LHC at a center-of-mass energy of 13 TeV and
1561 collected by the CMS detector in 2016, 2017, and 2018. This analysis is the first
1562 at CMS to target pairs of displaced electrons or muons without requiring that they
1563 form a common vertex. The observation is consistent with the background-only hy-
1564 pothesis, and limits are set on the product of the cross section of top squark pair
1565 production and the branching fraction to a lepton and a b or d quark through an
1566 R-parity-violating vertex. For a proper decay length hypothesis of 2 cm, top squarks
1567 with masses up 1500 GeV are excluded at the 95 % confidence level.

1568 Looking to the future, there are several opportunities to increase the sensitivity to
1569 new long-lived particles that decay to leptons. Aside from the incremental improve-
1570 ments offered by the expected increases in integrated luminosity and center-of-mass
1571 energy provided by the LHC (14 TeV proton-proton collisions may be available as

1572 soon as 2022 [84, 85]), there are a few changes to the analysis strategy that may be
1573 worth pursuing.

1574 The most straightforward improvement would be to study the electron and muon
1575 identification requirements with an eye to improving the signal efficiency, especially
1576 at large $|d_0|$. In particular, the missing inner hit and pixel hit requirements applied
1577 to electrons and muons, respectively, in the current analysis effectively limit the max-
1578 imum LLP decay length to the radius of the CMS pixel detector, which is 16 cm.
1579 Any gains in signal efficiency would of course have to be balanced against the likely
1580 increase in the mismeasurement background. Thinking along similar lines, it may be
1581 interesting to investigate the effects of relaxing the lepton isolation requirement.

1582 A more challenging angle would be to explicitly consider tau leptons in the final
1583 state. The analysis presented here is sensitive to displaced taus that decay leptonically
1584 to electrons and muons, but a future analysis could likely expand this sensitivity by
1585 explicitly studying the $|d_0|$ behavior of displaced taus. Given the tau decay branching
1586 fractions [33], the largest gain would likely come from considering hadronic tau decays,
1587 though this route would also likely represent a considerable challenge.

1588 Finally, one could perform an analysis similar to the one presented here but specif-
1589 ically target new low-mass long-lived particles. The lepton p_T requirements imposed
1590 by the trigger limit the low-mass sensitivity of the current analysis. One possible ap-
1591 proach would be to adopt a different triggering strategy in the next data-taking period,
1592 but it may be that CMS has already collected the ideal dataset in which to perform
1593 such a search. In 2018, CMS debuted a novel trigger strategy in which specialized
1594 triggers collected approximately ten billion unbiased b-hadron-decay events [86]. The
1595 triggers use a tag-and-probe strategy that actually require the presence of at least

1596 one displaced muon whose p_T can be as low as 7 GeV. The trade-off is that most of
1597 the muons will be embedded in b-tagged jets, which will likely necessitate changes to
1598 the analysis strategy. Such a search could be an interesting way to cover new ground
1599 with existing data.

1600 Searches for BSM LLPs are critical to exploring the available new-physics param-
1601 eter space and ultimately to understanding whether new physics exists at currently
1602 accessible energy scales. The analysis presented here explicitly constrains the natural
1603 parameter space of RPV SUSY models, but more importantly, it also constrains any
1604 not-yet-imagined new physics scenarios that could produce displaced leptons. There
1605 are still many stones unturned, and the analysis presented in this thesis shines a light
1606 on one more region of this unexplored space.

Appendix A: Impact of APV25 saturation on displaced tracking

A portion of the data collected by the CMS detector in 2016 is affected by the APV saturation effect described in Ref. [87]. The APV25 saturation effect is a byproduct of the production of heavily ionising particles (HIPs) in inelastic interactions between hadrons and the nuclei of silicon sensors. The energy deposits of HIPs can be up to 1000 times greater than those of typical particles produced in LHC collisions. These large energy deposits can saturate the analog readout of the APV25 chips [88] that are used to read out the CMS silicon strip tracker, which is described in Section 2.2.2. Due to a feature of the APV25 powering scheme that normally helps stabilize the pulse-height baseline, a single saturated channel can inadvertently suppress the outputs of the 127 other APV25 channels for hundreds of nanoseconds.

Only around one in every 1000 incident hadrons will result in saturating HIP events, so the effect is only significant at high instantaneous luminosities. In 2016, the instantaneous luminosity increased to greater than the original LHC design goal, and the effect began influencing detector performance. Starting in run 278802, the tracker front-end electronics were reconfigured to substantially reduce their sensitivity to the APV25 saturation effect.

1625 The deadtime associated with the a saturating HIP event can cause some tracker
1626 hits to be lost. This effect can lead to reduced tracking efficiency, and it is reasonable
1627 to suspect that the lose of efficiency may be more significant for displaced particles
1628 that may have fewer tracker hits to begin with. To investigate the impact on displaced
1629 tracking, one of our collaborators, Ian Tomalin, performed a study with $K_S^0 \rightarrow \pi^+\pi^-$
1630 decays. From this study, we conclude that only data taken after the APV25 saturation
1631 effect was mitigated should be used in the Displaced Leptons analysis. We therefore
1632 use only eras G and H in 2016 and all available data from 2017 and 2018.

1633 Using data collected in 2016, 2017, and 2018 with the `HLT_ZeroBias` trigger, the
1634 reconstructed K_S^0 candidate decay lengths are compared among several different runs
1635 that correspond to a wide range of instantaneous luminosities and data-taking periods.
1636 The K_S^0 candidates used come from the `generalV0Candidates:Kshort` collection.
1637 Each candidate must have a pair of oppositely charged tracks consistent with the K_S^0
1638 mass and coming from a common vertex that is at least 2 cm from the beam line.
1639 The tracks are required to have at least one pixel hit and $|\eta| < 2$. In 2016 (2017-18),
1640 the tracks are required to have $p_T > 0.7$ GeV (1.5 GeV).

1641 Figure A.1 shows the reconstructed transverse decay length of the K_S^0 candidates
1642 for data from all three years. Each distribution is normalized to the integrated lumi-
1643 nosity of the run from which it is taken. In the 2016 plot, the solid (dashed) lines
1644 correspond to runs taken before (after) the APV25 saturation effect was mitigated.
1645 In the pre-mitigation runs, the K_S^0 transverse decay length distribution falls rapidly
1646 with increasing instantaneous luminosity, but the dependence on instantaneous lumi-
1647 nosity is significantly reduced in the post-mitigation runs and in all 2017 and 2018

1648 runs. The narrower transverse decay length at higher luminosity in the 2016 pre-
1649 mitigation runs is interpreted as an instantaneous-luminosity-dependent decrease in
1650 tracking efficiency.

1651 Given the size of this effect, we decide not to use 2016 data taken before run
1652 278802 in the Displaced Leptons search. The instantaneous-luminosity-dependent
1653 displaced tracking efficiency would be difficult to quantify, which would lead to large
1654 systematic uncertainties. Furthermore, the signal yield would be suppressed by the
1655 lower displaced tracking efficiency. Finally, studies of displaced tracking efficiency
1656 with cosmic ray data are insensitive to the APV25 saturation effect because the
1657 instantaneous luminosity during dedicated cosmic runs is zero.

1658 A small dependence on instantaneous luminosity is also apparent in the 2017
1659 and 2018 distributions shown in Fig. A.1. The runs with the lowest (highest) in-
1660 stantaneous luminosity examined in each data taking period are shown with dashed
1661 (solid) lines. This may be due to a residual APV saturation effect or possibly another
1662 luminosity-related tracker inefficiency. We do not find it necessary to take any special
1663 measures to account for this small effect in 2017 and 2018.

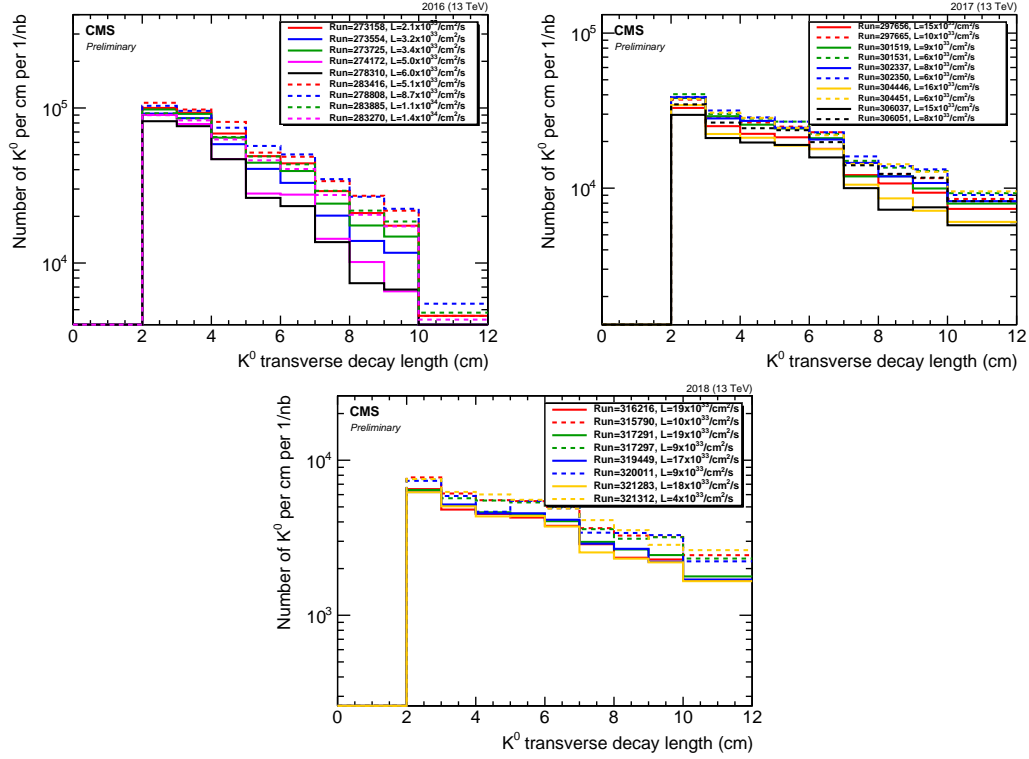


Figure A.1: Transverse decay length distribution of reconstructed $K_S^0 \rightarrow \pi^+\pi^-$ candidates for various runs in 2016 (top left), 2017 (top right) and 2018 (bottom). The peak instantaneous luminosity of each run is indicated in the legend, and each distribution is normalized to the integrated luminosity of the run. In the 2016 plot, runs taken before (after) the APV25 saturation effect was mitigated are shown by solid (dashed) lines. In the 2017 plot, the run with lowest (highest) instantaneous luminosity examined in each data taking era is plotted with a dashed (solid) line. Towards the end of 2017 (orange and black lines) the LHC ran with approximately 20% fewer proton bunches, meaning that the instantaneous luminosity per bunch crossing was higher than one might naively expect from the instantaneous luminosities shown in the legend.

1664

Appendix B: Poorly measured lepton $|d_0|$ at large $|\eta|$

1665

We require muons to have $|\eta| < 1.5$ due to the observed increase in width of the muon d_0 distribution at large $|\eta|$ in DY simulation with $Z \rightarrow \tau\tau \rightarrow ll$ events removed (see Fig. B.1 (left)). The width visibly increases at large $|\eta|$ in all three years but is less pronounced in 2017 and 2018 due to the improved performance of the Phase-1 pixel detector. The upgraded pixel detector is also responsible for the overall difference in d_0 width between years. Requiring muon $|\eta| < 1.5$ has two effects: (1) it dramatically reduces the mismeasurement background in 2016 data in the $\mu\mu$ channel, and (2) it removes a possible source of $|d_0^a| - |d_0^b|$ correlation in which the correlation between muons in η leads to correlation between muons in $|d_0|$. As shown in Fig. B.1 (right), muons from $\tilde{t}\tilde{t} \rightarrow \bar{l}b l\bar{b}$ events tend to have small $|\eta|$, so requiring muon $|\eta| < 1.5$ has a minimal effect on the signal acceptance.

1676

Electron d_0 resolution also worsens at large $|\eta|$. Furthermore, Fig. B.2 (left) shows that electrons from SM mesons are particularly concentrated $|\eta| > 1.5$. As in the muon case, electrons from $\tilde{t}\tilde{t} \rightarrow \bar{l}b l\bar{b}$ events tend to have $|\eta| < 1.5$ (see Fig. B.2), which implies that requiring electron $|\eta| < 1.5$ will reduce the mismeasurement and SM meson backgrounds without significantly reducing signal acceptance.

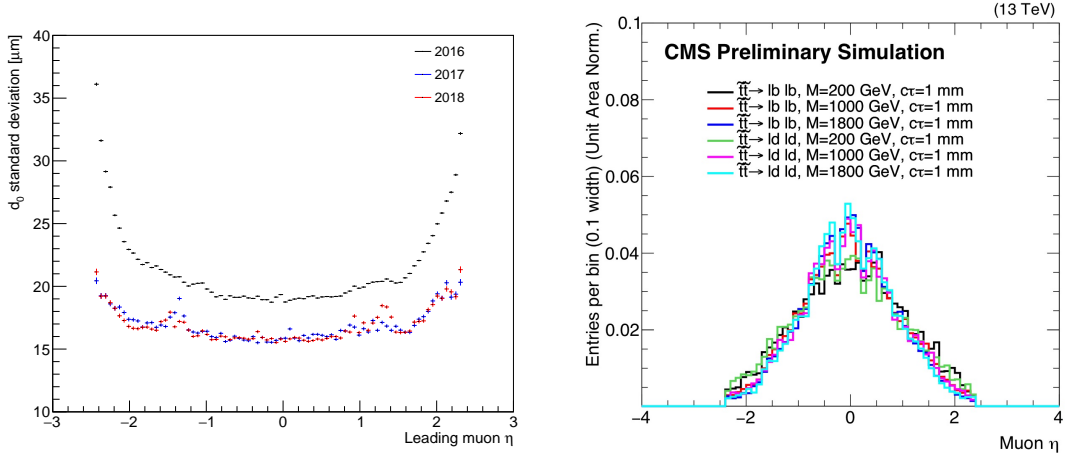


Figure B.1: The standard deviation of the leading muon d_0 as a function of the leading muon η for simulated background events (left). To ensure that the variation in width is purely due to d_0 resolution effects, we use a sample of simulated Drell-Yan events from which the $Z \rightarrow \tau\tau \rightarrow ll$ events have been removed. Muon η distribution for simulated $\tilde{t}\tilde{t} \rightarrow l\bar{b} l\bar{b}$ events (right). The $\mu\mu$ preselection with a loosened $|\eta|$ requirement is applied in both plots.

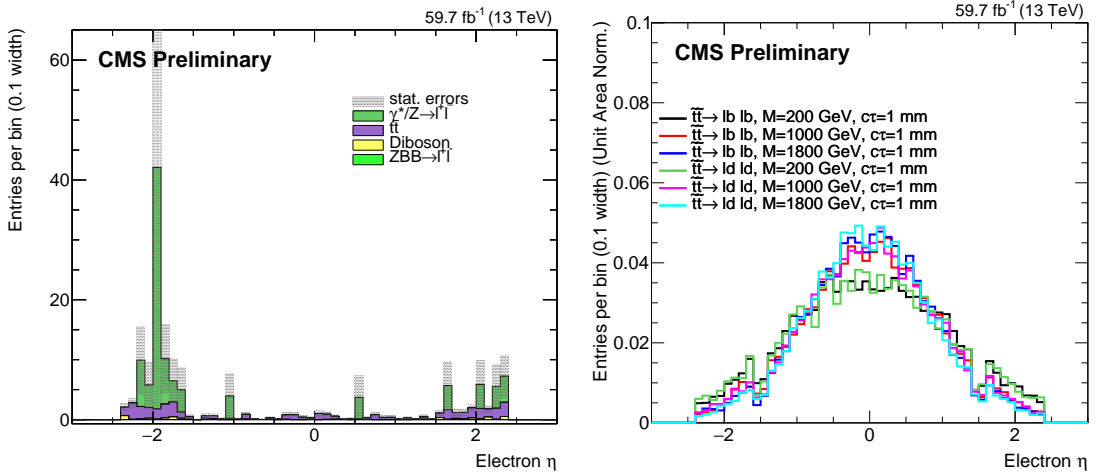


Figure B.2: Electron η distribution for simulated background events in which the electron parent particles are required to be SM mesons (left). Electron η distribution for simulated $\tilde{t}\tilde{t} \rightarrow l\bar{b} l\bar{b}$ events (right). The $e\mu$ preselection with a loosened η requirement is applied in both plots.

Appendix C: Displaced tracking efficiency

1682 To measure the efficiency to reconstruct displaced, isolated, high- p_T muons, our
1683 collaborator Ian Tomalin performed a study with cosmic rays. The basic idea is to ap-
1684 proximate the displaced tracking efficiency in data and simulation from the fraction of
1685 cosmic ray muons reconstructed in the muon system that have a corresponding track
1686 in the tracker. The results of this study are used to assign a systematic uncertainty
1687 in the signal efficiency (see Section 3.6) and define the upper bound of 10 cm on the
1688 inclusive signal region (see Section 3.3).

1689 First, the cosmic ray dataset is chosen. CMS collects cosmic ray data in two types
1690 of runs: (1) dedicated cosmic runs in which cosmic ray muons are reconstructed
1691 with dedicated reconstruction algorithms and (2) parasitic cosmic runs in which the
1692 triggers veto bunch-crossing events to collect cosmic ray data in otherwise normal
1693 proton-proton running conditions. In the parasitic cosmic runs, the cosmic ray muons
1694 are reconstructed with the standard reconstruction algorithms as well as some dedi-
1695 cated reconstruction algorithms. These two types of runs are then collected into two
1696 datasets: (1) `Cosmics`, which contains only the dedicated cosmic runs and (2) `NoBPTX`,
1697 which contains both the dedicated and parasitic cosmic runs. In each case, the strip
1698 tracker electronics operate in the same mode used for proton-proton collisions. The

1699 NoBPTX datasets are used in this study because they include the same reconstruction
1700 algorithms as used in the Displaced Leptons analysis.

1701 Events are collected with the `HLTL2Mu10NoVertexNoBPTX3BXv*` trigger, which ve-
1702 toes events with proton-proton collisions and requires that a muon with $p_T > 10 \text{ GeV}$
1703 is reconstructed in the muon system. As in the Displaced Leptons analysis, the trig-
1704 ger does not explicitly constrain the muon d_0 or d_z . Following the study presented
1705 in Appendix A, only eras G and H are used in 2016. The set of data-taking periods
1706 with reliable detector performance is identified with particular attention paid to the
1707 following properties: (1) suitable cosmic trigger timing configuration, (2) data qual-
1708 ity assessed from reconstructed (as opposed to trigger-level) quantities, (3) trigger,
1709 tracker, muon system, and track reconstruction known to be functioning well, and
1710 (4) magnetic field value in normal range.

1711 To compare the displaced tracking efficiency between data and simulation, sim-
1712 ulated cosmic ray events are produced using the CMSCGEN generator [89]. The
1713 simulated cosmic ray muons have $p_T > 20 \text{ GeV}$, $|d_0| < 40 \text{ cm}$, $|d_z| < 80 \text{ cm}$, and arrive
1714 within a 30 ns window centered on the time at which tracker readout efficiency is
1715 greatest. The detector response is modeled with GEANT [90].

1716 In both data and simulated events, cosmic rays are reconstructed in the tracker
1717 using the same track reconstruction algorithm that is used during proton-proton
1718 collisions. This algorithm assumes particles propagate outwards from the center of
1719 the detector, so cosmic ray muons are typically reconstructed as two tracks: one
1720 moving upward and one moving downwards. In the muon system, cosmic ray muons
1721 are reconstructed with two dedicated algorithms. The first is a two-leg algorithm
1722 that reconstructs each cosmic ray muon as two separate muons, one in the top half of

1723 CMS and the other in the bottom. The second is a one-leg algorithm that reconstructs
1724 cosmic rays as a single muon that traverses the entire detector. The longer lever arm
1725 provided by the one-leg algorithm generally results in more accurate measurements
1726 of the muon curvature in the magnetic field.

1727 A preliminary event selection is then applied to the data and simulation. The
1728 events are required to have one one-leg muon with $p_T > 20 \text{ GeV}$ and at least 50 hits
1729 in the muon system. While the p_T requirement of the muons selected in this study
1730 is lower than the Displaced Leptons muon p_T requirement, the tracking efficiency
1731 does not depend significantly on p_T in the relevant range. The one-leg muon is also
1732 required to be within 0.3 rad of two two-leg muons in ϕ in order to reject cosmic ray
1733 muon candidates that do not traverse the entire detector.

1734 The tracking efficiency is inferred from the fraction of selected one-leg muons that
1735 are associated with a tracker track that has $p_T > 15 \text{ GeV}$ and is within 0.2 rad in ϕ of
1736 the selected one-leg muon. To mimic the Displaced Leptons event selection, tracker
1737 tracks are also required to have at least one pixel hit. Because each cosmic ray muon
1738 generally results in two tracker tracks, two separate efficiencies are measured. These
1739 efficiencies are referred to as “upward” and “downward” according to the direction of
1740 the relevant tracker track. The downward efficiency is expected to be more reliable
1741 because the tracker readout electronics assume that particles propagate outward from
1742 the center of the detector. The upward and downward efficiencies measured in this
1743 study agree within a few percent, but the downward efficiencies are used for the
1744 definitive measurement.

1745 The muon system also measures the cosmic ray muon arrival time. The average
1746 of the two two-leg muon arrival times provides the most precise measurement of the

Table C.1: Cosmic ray muon arrival time requirements used when measuring displaced tracking efficiency in data and simulation.

	2016–2017	2018
Data	$-13 \text{ ns} < t_{\mu\text{on}} < -7 \text{ ns}$	$-8 \text{ ns} < t_{\mu\text{on}} < -2 \text{ ns}$
Simulation	$-38 \text{ ns} < t_{\mu\text{on}} < -32 \text{ ns}$	$-40 \text{ ns} < t_{\mu\text{on}} < -34 \text{ ns}$

1747 cosmic ray muon arrival time. This approach provides a time resolution on the order
1748 of 5 ns, whereas the time resolution provided by one-leg muons can be an order of
1749 magnitude greater.

1750 The selected one-leg muons with $|d_0| < 8 \text{ cm}$ and $|d_z| < 20 \text{ cm}$ are used to study the
1751 tracking efficiency dependence on cosmic ray muon arrival time. Figure C.1 shows the
1752 distribution of the measured arrival time while Fig. C.2 shows the measured downward
1753 tracking efficiency as a function of measured arrival time. The disagreement between
1754 data and simulation in measured arrival time is simply an artifact of the specified
1755 simulation time window. Despite this offset, the efficiency shows a clear peak with a
1756 width of approximately 15 ns in both data and simulation. Based on the results of
1757 Fig. C.2, muons used in the downward tracking efficiency measurement must also pass
1758 the requirements listed in Table C.1. Using the upward efficiency produces similar
1759 results that are shifted by approximately 5 ns. The same sample of one-leg muons is
1760 also used to measure the downward tracking efficiency as a function of run number.
1761 No meaningful dependence is identified.

1762 The downward tracking efficiency is then measured using all selected one-leg
1763 muons that meet the timing requirements specified in Table C.1. The downward track-
1764 ing efficiency as a function of $|d_0|$ and $|d_z|$ is shown for all three years in Fig. C.3. The

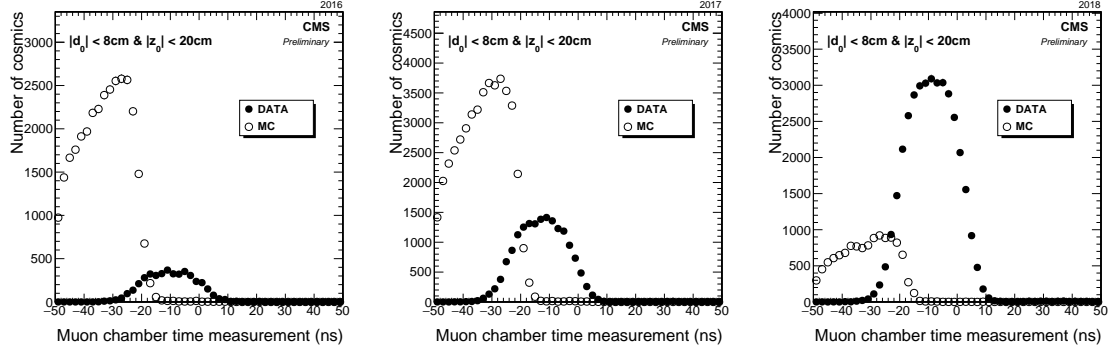


Figure C.1: Distribution of the arrival time of cosmic rays at their point of closest approach to the beamline as measured by the muon system in 2016 (left), 2017 (center), and 2018 (right) in data and simulation. Only cosmic ray muons with $|d_0| < 8\text{ cm}$ and $|z_0| < 20\text{ cm}$ are considered.

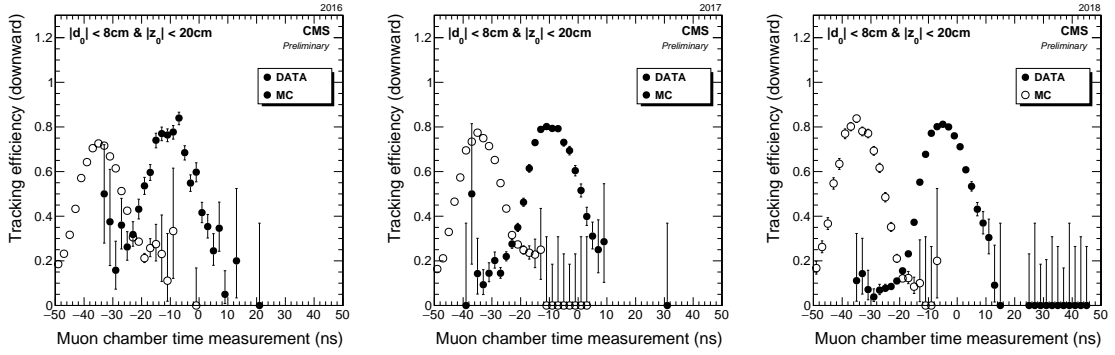


Figure C.2: Measured downward tracking efficiency versus cosmic ray muon arrival time in 2016 (left), 2017 (center), and 2018 (right) in data and simulation. Only cosmic ray muons with $|d_0| < 8\text{ cm}$ and $|z_0| < 20\text{ cm}$ are considered.

1765 tracking efficiency is found to be nonzero out to at least $|d_0| \leq 10$ cm and $|d_z| \leq 30$ cm
1766 in all three years. We also note that removing the pixel-hit requirement increases this
1767 range to approximately $|d_0| \leq 30$ cm and $|d_z| \leq 50$ cm.

1768 The results of Fig. C.3 are used to estimate a systematic uncertainty in the sim-
1769 ulated signal efficiency arising from the displaced tracking efficiency. A simulated
1770 $\tilde{t}\tilde{t} \rightarrow \bar{l}b \bar{l}b$ sample with a top squark mass of 1800 GeV and proper decay length
1771 $c\tau = 100$ cm is considered as it produces leptons with the largest impact parameters
1772 and therefore represents the most challenging scenario for the displaced track recon-
1773 struction. To accommodate the pixel hit requirements, only those events in which
1774 both top squarks decay within the volume of the pixel detector are considered. First,
1775 the $|d_0|$ and $|d_z|$ of both leptons in this subset of signal events are noted. Next, a
1776 two-dimensional plot of tracking efficiency as a function of $|d_0|$ and $|d_z|$, $\epsilon(|d_0|, |d_z|)$, is
1777 produced from the cosmic ray muons in data and simulated cosmic ray events. Using
1778 this plot, the mean efficiency to reconstruct both lepton tracks in the simulated signal
1779 events is evaluated as:

$$\frac{1}{N} \sum_i \epsilon(|d_0|_i^{(1)}, |z_0|_i^{(1)}) \epsilon(|d_0|_i^{(2)}, |z_0|_i^{(2)}) \quad (\text{C.1})$$

1780 where the sum extends over the N events in the signal sample and the superscripts (1)
1781 and (2) denote the two leptons in each event. For each year, the relative systematic
1782 uncertainty in the efficiency to reconstruct both lepton tracks is then taken from
1783 the ratio of the efficiencies in data and simulation. The resulting efficiencies and
1784 systematic uncertainties are listed in Table C.2.

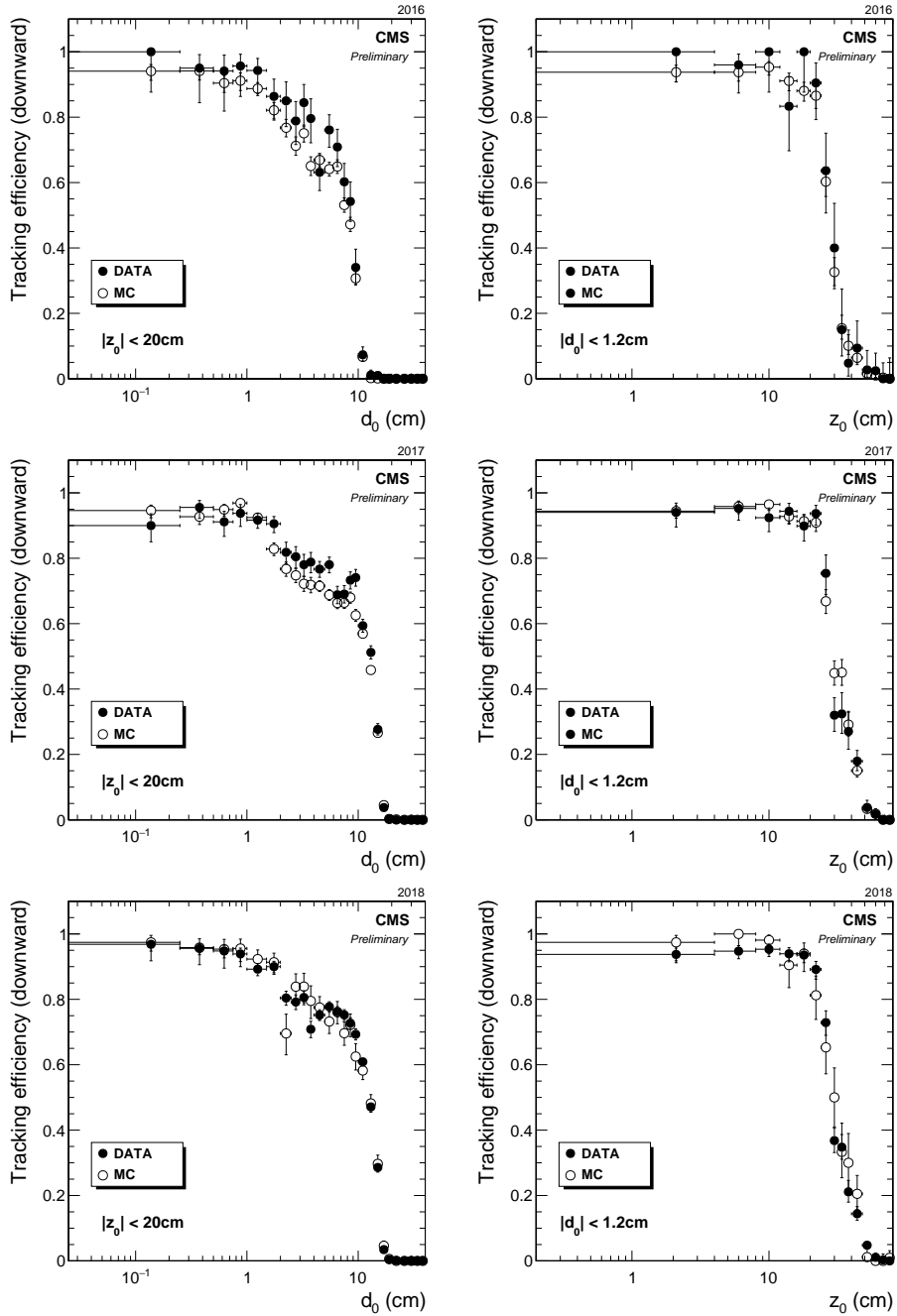


Figure C.3: Measured downward tracking efficiency in 2016 (top), 2017 (middle), and 2018 (bottom) versus $|d_0|$ (left) and $|d_z|$ (right) in data and simulation. $|d_z|$ ($|d_0|$) impact parameter is constrained to less than 20 cm (1.2 cm) when plotting against $|d_0|$ ($|d_z|$).

Table C.2: Mean measured efficiency to reconstruct both lepton tracks in simulated $\tilde{t}\tilde{t} \rightarrow l b \bar{l} \bar{b}$ events in data and simulation and the resulting systematic uncertainty. The top squark mass and proper decay length are assumed to be 1800 GeV and 100 cm.

	2016	2017	2018
Efficiency in data	$57.5 \pm 2.1\%$	$55.3 \pm 1.1\%$	$56.1 \pm 0.7\%$
Efficiency in simulation	$50.3 \pm 1.0\%$	$52.3 \pm 0.7\%$	$57.5 \pm 1.1\%$
Systematic uncertainty	$14.1 \pm 4.3\%$	$5.8 \pm 2.3\%$	$2.4 \pm 2.2\%$

Bibliography

- [1] CMS Collaboration. Performance of electron reconstruction and selection with the CMS detector in proton-proton collisions at $\sqrt{s} = 8\text{TeV}$. *Journal of Instrumentation*, 10(06):P06005–P06005, jun 2015.
- [2] Summaries of cms cross section measurements. <https://twiki.cern.ch/twiki/bin/view/CMSPublic/PhysicsResultsCombined>. Accessed: 2021-04-04.
- [3] Cms supersymmetry physics results. <https://twiki.cern.ch/twiki/bin/view/CMSPublic/PhysicsResultsSUS>. Accessed: 2021-04-04.
- [4] Brian Shuve. Theory overview of long-lived particles at the lhc. <https://indico.cern.ch/event/607314/contributions/2542308>.
- [5] Lyndon Evans and Philip Bryant. LHC machine. *Journal of Instrumentation*, 3(08):S08001–S08001, aug 2008.
- [6] Esma Mobs. The CERN accelerator complex - 2019. Complex des accélérateurs du CERN - 2019. Jul 2019. General Photo.
- [7] Jorg Wenninger. Operation and Configuration of the LHC in Run 2. Mar 2019.
- [8] AC Team. Diagram of an LHC dipole magnet. Schéma d'un aimant dipôle du LHC. Jun 1999.
- [9] Tai Sakuma. 3D SketchUp images of the CMS detector (120918). May 2016.
- [10] CMS Collaboration. The CMS experiment at the CERN LHC. The Compact Muon Solenoid experiment. *JINST*, 3:S08004. 361 p, 2008. Also published by CERN Geneva in 2010.
- [11] Run ii pixel performance plots for data and simulation. \textbf{\{https://lhcc-commissioning.web.cern.ch/schedule/LHC-long-term.htm\}}. Accessed: 2021-04-04.
- [12] The Tracker Group of the CMS Collaboration. The CMS Phase-1 Pixel Detector Upgrade. *JINST*, 16(02):P02027, 2021.

- 1811 [13] CMS Collaboration. Observation of a new boson at a mass of 125 GeV with the
1812 CMS experiment at the LHC. *PLB*, 716:30, 2012.
- 1813 [14] CMS Collaboration. CMS Physics: Technical Design Report Volume 1: Detector
1814 Performance and Software. 2006. There is an error on cover due to a technical
1815 problem for some items.
- 1816 [15] CMS Collaboration. Particle-flow reconstruction and global event description
1817 with the CMS detector. *JINST*, 12:P10003, 2017.
- 1818 [16] Image courtesy of Jamie Antonelli.
- 1819 [17] David J. Gross and Frank Wilczek. Asymptotically free gauge theories. i. *Phys.*
1820 *Rev. D*, 8:3633–3652, Nov 1973.
- 1821 [18] H. Fritzsch, M. Gell-Mann, and H. Leutwyler. Advantages of the color octet
1822 gluon picture. *Physics Letters B*, 47(4):365–368, 1973.
- 1823 [19] Steven Weinberg. A model of leptons. *Phys. Rev. Lett.*, 19:1264–1266, Nov 1967.
- 1824 [20] Jeffrey Goldstone, Abdus Salam, and Steven Weinberg. Broken symmetries.
1825 *Phys. Rev.*, 127:965–970, Aug 1962.
- 1826 [21] F. Englert and R. Brout. Broken symmetry and the mass of gauge vector mesons.
1827 *Phys. Rev. Lett.*, 13:321–323, Aug 1964.
- 1828 [22] Peter Ware Higgs. Broken symmetries, massless particles and gauge fields. *Phys.*
1829 *Lett.*, 12:132–133, 1964.
- 1830 [23] G. S. Guralnik, C. R. Hagen, and T. W. B. Kibble. Global conservation laws
1831 and massless particles. *Phys. Rev. Lett.*, 13:585–587, Nov 1964.
- 1832 [24] ATLAS Collaboration. Observation of a new particle in the search for the stan-
1833 dard model Higgs boson with the ATLAS detector at the LHC. *PLB*, 716:1,
1834 2012.
- 1835 [25] CMS Collaboration. Combined measurements of Higgs boson couplings in pro-
1836 ton–proton collisions at $\sqrt{s} = 13$ TeV. *Eur. Phys. J. C*, 79(5):421, 2019.
- 1837 [26] ATLAS Collaboration. Combined measurements of higgs boson production and
1838 decay using up to 80 fb^{-1} of proton-proton collision data at $\sqrt{s} = 13$ TeV
1839 collected with the atlas experiment. *Phys. Rev. D*, 101:012002, Jan 2020.
- 1840 [27] Masataka Fukugita and P. J. E. Peebles. The cosmic energy inventory. *The*
1841 *Astrophysical Journal*, 616(2):643–668, Dec 2004.

- 1842 [28] Gian Francesco Giudice. Naturally speaking: The naturalness criterion and
 1843 physics at the lhc. *Perspectives on LHC Physics*, page 155–178, Jun 2008.
- 1844 [29] Gerard 't Hooft. Naturalness, chiral symmetry, and spontaneous chiral symmetry
 1845 breaking. *NATO Sci. Ser. B*, 59:135–157, 1980.
- 1846 [30] Nima Arkani-Hamed, Savas Dimopoulos, and Gia Dvali. The hierarchy problem
 1847 and new dimensions at a millimeter. *Physics Letters B*, 429(3-4):263–272, Jun
 1848 1998.
- 1849 [31] Stephen P. Martin. A supersymmetry primer. *Advanced Series on Directions in*
 1850 *High Energy Physics*, page 1–98, Jul 1998.
- 1851 [32] Nathaniel Craig. The state of supersymmetry after run i of the lhc, 2014.
- 1852 [33] Particle Data Group. Review of Particle Physics. *Progress of Theoretical and*
 1853 *Experimental Physics*, 2020(8), 08 2020. 083C01.
- 1854 [34] Zhen Liu and Brock Tweedie. The fate of long-lived superparticles with hadronic
 1855 decays after lhc run 1. *Journal of High Energy Physics*, 2015(6), Jun 2015.
- 1856 [35] W Kilian, T Plehn, P Richardson, and E Schmidt. Split Supersymmetry at
 1857 Colliders. *Eur. Phys. J. C*, 39(hep-ph/0408088. DESY-04-136. DESY-2004-136.
 1858 CERN-PH-TH-2004-144):229–243. 28 p, Oct 2004.
- 1859 [36] Frank E Paige and J Wells. Anomaly mediated SUSY breaking at the LHC.
 1860 Technical Report hep-ph/0001249, Jan 2000.
- 1861 [37] Peter W. Graham, David E. Kaplan, Surjeet Rajendran, and Prashant Saraswat.
 1862 Displaced Supersymmetry. *JHEP*, 07:149, 2012.
- 1863 [38] Lawrence J. Hall and Mahiko Suzuki. Explicit r-parity breaking in supersym-
 1864 metric models. *Nuclear Physics B*, 231(3):419–444, 1984.
- 1865 [39] Linear accelerator 2. Sep 2012.
- 1866 [40] The Proton Synchrotron Booster. Jul 2012.
- 1867 [41] Proton Synchrotron. 1959.
- 1868 [42] The Super Proton Synchrotron. Jan 2012.
- 1869 [43] CMS Collaboration. CMS Physics: Technical Design Report Volume 2: Physics
 1870 Performance. *J. Phys. G*, 34(CERN-LHCC-2006-021. CMS-TDR-8-2):995–1579.
 1871 669 p, 2007. revised version submitted on 2006-09-22 17:44:47.
- 1872 [44] Cms collaboration. <https://cms.cern/collaboration>. Accessed: 2021-03-28.

- 1873 [45] A et al. Dominguez. CMS Technical Design Report for the Pixel Detector Up-
1874 grade. Technical Report CERN-LHCC-2012-016. CMS-TDR-11, Sep 2012.
- 1875 [46] Lea Michaela Caminada. Performance and Operation of the CMS Phase 1 Pixel
1876 Detector. Technical Report CMS-CR-2018-067, CERN, Geneva, Jun 2018.
- 1877 [47] A.M. Sirunyan, A. Tumasyan, W. Adam, F. Ambrogi, E. Asilar, T. Bergauer,
1878 J. Brandstetter, E. Brondolin, M. Dragicevic, J. Erö, and et al. Performance of
1879 the cms muon detector and muon reconstruction with proton-proton collisions
1880 at $\sqrt{s} = 13$ tev. *Journal of Instrumentation*, 13(06):P06015–P06015, Jun 2018.
- 1881 [48] M.A. Shah, R. Hadjiska, A. Fagot, M. Gul, C. Roskas, M. Tytgat, N. Zaganidis,
1882 S. Fonseca De Souza, A. Santoro, F. Torres Da Silva De Araujo, and et al.
1883 The cms rpc detector performance and stability during lhc run-2. *Journal of
1884 Instrumentation*, 14(11):C11012–C11012, Nov 2019.
- 1885 [49] Mia Tosi. The CMS trigger in Run 2. Technical Report CMS-CR-2017-340,
1886 CERN, Geneva, Oct 2017.
- 1887 [50] L. Cadamuro. The cms level-1 trigger system for lhc run ii. *Journal of Instru-
1888 mentation*, 12(03):C03021, 2017.
- 1889 [51] W Adam, R Frühwirth, A Strandlie, and T Todorov. Reconstruction of electrons
1890 with the gaussian-sum filter in the CMS tracker at the LHC. *Journal of Physics
1891 G: Nuclear and Particle Physics*, 31(9):N9–N20, jul 2005.
- 1892 [52] CMS Collaboration. Search for displaced supersymmetry in events with an elec-
1893 tron and a muon with large impact parameters. *Physical Review Letters*, 114(6),
1894 Feb 2015.
- 1895 [53] CMS Collaboration. Search for displaced leptons in the e-mu channel. Technical
1896 Report CMS-PAS-EXO-16-022, CERN, Geneva, 2016.
- 1897 [54] Juliette Alimena et al. Searching for long-lived particles beyond the standard
1898 model at the large hadron collider. *Journal of Physics G: Nuclear and Particle
1899 Physics*, 47(9):090501, sep 2020.
- 1900 [55] CMS Collaboration. Search for disappearing tracks in proton-proton collisions
1901 at $s=13$ tev. *Physics Letters B*, 806:135502, Jul 2020.
- 1902 [56] CMS Collaboration. Search for long-lived particles using delayed photons in
1903 proton-proton collisions at $s=13$ tev. *Physical Review D*, 100(11), Dec 2019.
- 1904 [57] CMS Collaboration. Search for long-lived particles using nonprompt jets and
1905 missing transverse momentum with proton-proton collisions at $s=13$ tev. *Physics
1906 Letters B*, 797:134876, Oct 2019.

- 1907 [58] J. Alwall, R. Frederix, S. Frixione, V. Hirschi, F. Maltoni, O. Mattelaer, H. S.
 1908 Shao, T. Stelzer, P. Torrielli, and M. Zaro. The automated computation of tree-
 1909 level and next-to-leading order differential cross sections, and their matching to
 1910 parton shower simulations. *JHEP*, 07:079, 2014.
- 1911 [59] Rikkert Frederix and Stefano Frixione. Merging meets matching in MC@NLO.
 1912 *JHEP*, 12:061, 2012.
- 1913 [60] Johan Alwall et al. Comparative study of various algorithms for the merging
 1914 of parton showers and matrix elements in hadronic collisions. *Eur. Phys. J. C*,
 1915 53:473, 2008.
- 1916 [61] Stefano Frixione and Bryan R. Webber. Matching NLO QCD computations and
 1917 parton shower simulations. *JHEP*, 06:029, 2002.
- 1918 [62] Paolo Nason. A New method for combining NLO QCD with shower Monte Carlo
 1919 algorithms. *JHEP*, 11:040, 2004.
- 1920 [63] Stefano Frixione, Paolo Nason, and Carlo Oleari. Matching NLO QCD computa-
 1921 tions with Parton Shower simulations: the POWHEG method. *JHEP*, 11:070,
 1922 2007.
- 1923 [64] Simone Alioli, Paolo Nason, Carlo Oleari, and Emanuele Re. NLO vector-boson
 1924 production matched with shower in POWHEG. *JHEP*, 07:060, 2008.
- 1925 [65] Simone Alioli, Paolo Nason, Carlo Oleari, and Emanuele Re. A general frame-
 1926 work for implementing NLO calculations in shower Monte Carlo programs: the
 1927 POWHEG BOX. *JHEP*, 06:043, 2010.
- 1928 [66] Torbjörn Sjöstrand, Stefan Ask, Jesper R. Christiansen, Richard Corke, Nishita
 1929 Desai, Philip Ilten, Stephen Mrenna, Stefan Prestel, Christine O. Rasmussen, and
 1930 Peter Z. Skands. An introduction to PYTHIA 8.2. *Comput. Phys. Commun.*,
 1931 191:159, 2015.
- 1932 [67] Vardan Khachatryan et al. Event generator tunes obtained from underlying event
 1933 and multiparton scattering measurements. *Eur. Phys. J.*, C76(3):155, 2016.
- 1934 [68] CMS Collaboration. Extraction and validation of a new set of CMS PYTHIA8
 1935 tunes from underlying-event measurements. *EPJC*, 80:4, 2020.
- 1936 [69] Johan Alwall, A. Ballestrero, P. Bartalini, S. Belov, E. Boos, et al. A standard
 1937 format for Les Houches event files. *Comput. Phys. Commun.*, 176:300, 2007.
- 1938 [70] B.C. Allanach, M. Battaglia, G.A. Blair, Marcela S. Carena, A. De Roeck, et al.
 1939 The Snowmass points and slopes: Benchmarks for SUSY searches. *EPJC*, 25:113,
 1940 2002.

- 1941 [71] CMS Collaboration. Precision measurement of the structure of the CMS inner
 1942 tracking system using nuclear interactions. *JINST*, 13:P10034, 2018.
- 1943 [72] CMS Collaboration. Precision measurement of the structure of the CMS inner
 1944 tracking system using nuclear interactions with data collected in 2018. *CMS-*
 1945 *DP-2019-001*, 2019.
- 1946 [73] Jared A. Evans and Jessie Shelton. Long-lived staus and displaced leptons at
 1947 the LHC. *JHEP*, 04:056, 2016.
- 1948 [74] CMS Collaboration. Identification of b quark jets at the CMS Experiment in the
 1949 LHC Run 2. Technical Report CMS-PAS-BTV-15-001, CERN, Geneva, 2016.
- 1950 [75] CMS Collaboration. CMS luminosity measurements for the 2016 data taking
 1951 period. CMS Physics Analysis Summary CMS-PAS-LUM-17-001, 2017.
- 1952 [76] CMS Collaboration. CMS luminosity measurements for the 2017 data-taking
 1953 period at $\sqrt{s} = 13$ TeV. CMS Physics Analysis Summary CMS-PAS-LUM-17-
 1954 004, 2018.
- 1955 [77] CMS Collaboration. CMS luminosity measurements for the 2018 data-taking
 1956 period at $\sqrt{s} = 13$ TeV. CMS Physics Analysis Summary CMS-PAS-LUM-18-
 1957 002, 2018.
- 1958 [78] Lumi POG. Luminosity POG Twiki. [https://twiki.cern.ch/twiki/bin/vi
 1959 ew/CMS/TWikiLUM#LumiComb](https://twiki.cern.ch/twiki/bin/view/CMS/TWikiLUM#LumiComb).
- 1960 [79] CMS Collaboration. Measurement of the inelastic proton-proton cross section at
 1961 $\sqrt{s} = 13$ TeV. *JHEP*, 07:161, 2018.
- 1962 [80] Thomas Junk. Confidence level computation for combining searches with small
 1963 statistics. *Nucl. Instrum. Meth. A*, 434:435, 1999.
- 1964 [81] A. L. Read. Presentation of search results: the CL_s technique. In *Durham*
 1965 *IPPP Workshop: Advanced Statistical Techniques in Particle Physics*, page 2693,
 1966 Durham, UK, March 2002. [*J. Phys. G* 28 (2002) 2693].
- 1967 [82] Glen Cowan, Kyle Cranmer, Eilam Gross, and Ofer Vitells. Asymptotic formulae
 1968 for likelihood-based tests of new physics. *Eur. Phys. J. C*, 71:1554, 2011.
- 1969 [83] The ATLAS Collaboration, The CMS Collaboration, The LHC Higgs Combi-
 1970 nation Group. Procedure for the LHC Higgs boson search combination in Summer
 1971 2011. Technical Report CMS-NOTE-2011-005, ATL-PHYS-PUB-2011-11, 2011.
- 1972 [84] B Aa Petersen and C Schwick. Experiment Requests and Constraints for Run 3.
 1973 Technical report, 2019.

- 1974 [85] Longer term lhc schedule. <https://lhcb-commissioning.web.cern.ch/schedule/LHC-long-term.htm>. Accessed: 2021-04-04.
- 1976 [86] Robert Bainbridge. Recording and reconstructing 10 billion unbiased b hadron
1977 decays in cms. *EPJ Web Conf.*, 245:01025, 2020.
- 1978 [87] W. Adam et al. The effect of highly ionising particles on the CMS silicon strip
1979 tracker. *Nucl. Instrum. Meth. A*, 543:463, 2005.
- 1980 [88] M J French, L L Jones, Q R Morrissey, A Neviani, R Turchetta, J R Fulcher,
1981 G Hall, E Noah, M Raymond, G Cervelli, P Moreira, and G Marseguerra. Design
1982 and results from the APV25, a deep sub-micron CMOS front-end chip for the
1983 CMS tracker. *Nucl. Instrum. Methods Phys. Res., A*, 466(2):359–65, 2001.
- 1984 [89] Philipp Biallass, Thomas Hebbeker, and K Höpfner. Simulation of Cosmic Muons
1985 and Comparison with Data from the Cosmic Challenge using Drift Tube Cham-
1986 bers. Technical Report CMS-NOTE-2007-024, CERN, Geneva, Mar 2007.
- 1987 [90] S. Agostinelli et al. Geant4—a simulation toolkit. *Nuclear Instruments and*
1988 *Methods in Physics Research Section A: Accelerators, Spectrometers, Detectors*
1989 *and Associated Equipment*, 506(3):250–303, 2003.